Hydrogen ignition and safety

Pierre Boivin, Marc Le Boursicaud, Alejandro Millán-Merino, Said Taileb, Josué Melguizo-Gavilanes, Forman Williams

Hydrogen ignition and safety

Pierre Boivin, Marc Le Boursicaud, Alejandro Millán-Merino,
Said Taileb, Josué Melguizo-Gavilanes, Forman Williams

Abstract This chapter provides an overview of H_2 ignition and safety-related questions, to be addressed in the development of future H_2 thermal engines. Basics of H_2 ignition phenomena are covered in the first part, including the well-known branched-chain oxidation reactions described by Semenov & Hinshelwood, as well as useful analytical derivations of induction delay times. The second part provides an overview of classical canonical limit problems, including the explosion-limit (p, T) diagram, the propagation limits of both deflagrations and detonations, and shock-induced or thermal-induced ignitions. The two remaining parts address two opposite but complementary questions: how to ignite a H_2 engine, and how to prevent hazardous H_2 ignition. In the former, a list of available technologies is offered, while in the latter, simplified models are presented to predict ignition hazards from cold-flow numerical simulations.

Pierre Boivin, Marc Le Boursicaud, Alejandro Millán-Merino, Said Taileb
Aix Marseille Univ, CNRS, Centrale Marseille, M2P2, Marseille, France,
e-mail: pierre.boivin@cnrs.fr

Josué Melguizo-Gavilanes
Institut Pprime, UPR 3346 CNRS, ISAE-ENSMA, Futuroscope-Chasseneuil, France

Forman Williams
University of California San Diego, La Jolla, California

Nomenclature

Symbol	Name	Units (SI)	Equation
$\mathbf{A}$	ignition kinetic Jacobian matrix	s^{-1}	(25)
C_k	k^{th} molar concentration	mol/m^3	(4)
C_{M_j}	effective third-body concentration of step $j = (4, 8)$	mol/m^3	
$\overline{c}$	average molecular velocity	m/s	(61)
c_p	specific heat at constant pressure	J/K/kg	(8)
D_{CJ}	Chapman-Jouguet detonation velocity	m/s	(71)
D_k	k^{th} species diffusion coefficient	m^2/s	(57)
D_T	thermal diffusion coefficient	m^2/s	(73)
E_a	activation energy	J/mol	
h_k	k^{th} species molar formation enthalpy	J/mol	(8)
j	reaction index	1	
k	species index	1	
k_j	j^{th} reaction Arrhenius rate constant (forward: k_{jf}, backward: k_{jb})	$m^3/mol/s^*$	(6)
	* unit for a second-order reaction.		
$k_{k,w}$	k^{th} species wall destruction rate	s^{-1}	(63)
l_j	j^{th} reaction rate inverse characteristic time	s^{-1}	(25)
p	pressure	Pa	(1)
Q	heat of reaction $2\,H_2 + O_2 \longrightarrow 2\,H_2O$	J/mol	(49)
q	dimensionless heat of reaction	1	(53)
R	molar gas constant	J/K/mol	(1)
r	radial coordinate	m	
S_L	premixed flame velocity	m/s	
T	temperature	K	(1)
T_c	crossover temperature ($\alpha = 1$)	K	(18)
T_p	premixed flame limit temperature (lean limit: $\alpha = 2$)	K	(69)
T_{vN}	von Neumann state temperature (detonation)	K	
t	time	s	
t_B	branching time	s	(28)
t_E	thermal explosion time	s	(56)
t_i	induction time ($t_i = t_B + t_E$)	s	(10)
V_k	ignition radical pool composition vector	1	(27, 29)
W	mixture molecular weight	kg/mol	(2)
W_k	k^{th} molecular weight	kg/mol	(2)
X_k	k^{th} mole fraction	1	(3)
Y_k	k^{th} mass fraction	1	(3)
α	crossover parameter	1	(18)
β	dimensionless activation energy	1	
δ_c	detonation cell size	m	
$\bar{\epsilon}$	initiation rate vector	$mol/m^3/s$	(24)
ε	sticking coefficient	1	(63)
φ	equivalence ratio	1	(5)
γ	ratio of specific heats	1	
κ	thermal conductivity	W/m/K	(67)
λ	reactivity (inverse characteristic branching time)	s^{-1}	(27, 42)
ρ	volume mass	kg/m^3	(1)
θ	dimensionless temperature	1	(50)
$\dot{\omega}_k$	k^{th} species net production rate	s^{-1}	(73)
ω_j	j^{th} reaction rate	$mol/m^3/s$	(6)
$\dot{\omega}_T$	heat equation chemical source term	K/s	(73)

Introduction

Modifying the design of classical hydrocarbon thermal engines to burn hydrogen instead, whilst effectively suppressing CO_2 emissions locally, is far from being simple. The space-propulsion sector, which relied heavily on H_2 cryogenic engines for their high specific energy and associated specific impulse, is well aware of the challenges of H_2 usage. Worryingly, this sector is now largely reconsidering that choice, getting back to hydrocarbon fuels such as methane : Although the H_2 specific energy (energy released per unit mass consumed) is almost three times that of conventional fuels, its energy per unit volume is 3000-4000 times lower than conventional (liquid) petroleum-derived fuels under ambient conditions. When space is a constraint (e.g. in the transportation sector) H_2 tanks must therefore be either heavily compressed (up to 700 atm.), or cooled to cryogenic temperatures, the H_2 boiling point being close to 20 K at normal ambient pressure. Both alternatives require very heavy and solid tanks and feed systems.

When engineering any fluid system, especially a high-pressure system, the question is not so much *whether* it will leak, but rather *how much* it will leak. This is even more true with H_2, among the most fugacious gases. The question of H_2 safety is therefore of paramount importance in the design of future H_2 thermal engines. In particular, it is important to set appropriate design rules for the acceptable H_2 leakage rates depending on the local environment (oxidant, local concentration, pressure, bulk temperature, wall temperature, micro-channel widths, etc.).

Hydrogen and hydrocarbons also have very distinct explosion, flammability, and detonability limits. They do require careful scrutiny, as they are generally found to be much wider for H_2, allowing for more potentially disastrous scenarios. For instance, H_2 flame propagation is possible in more diluted and leaner regions, including through millimeter-wide channels, where hydrocarbons typically quench. These wide flammability limits make H_2 very prone to flashback hazards in places a conventional thermal-engine specialist would not expect. Hydrogen is also more prone to deflagration-to-detonation transition (DDT), potentially with disastrous effects. Last but not least, combustion temperatures are higher for H_2 than hydrocarbons, so the engine design point must be set closer to the lean flammability limit to avoid a drastic increase of NO_x emissions, and this is precisely where H_2 combustion is hardest to stabilize.

Focusing now on the bright side, H_2 is probably the fuel which was most studied by the combustion scientific community, perhaps for its oxymoronic characteristic of being both the most elementary fuel and the one involving the most complexity. Elementary because its thermochemical and chemical-kinetic properties are comparably simpler – or at least better established – than for any other fuel. Its explosion limits, for example, are very clearly defined in comparison with those of hydrocarbons, the underlying branched-chain chemistry having been unravelled by Semenov & Hinshelwood over 80 years ago. But it also involves the most complexity, in that H_2 is a very capricious gas, for example exhibiting diffusive-thermal instabilities that do not exist with conventional fuels.

The objective of this chapter is to provide the reader with an overview of the physical phenomena controlling ignition and extinction limits of H_2, indicating potential pitfalls and unexpected limit behavior. For instance, common sense dictates that a gaseous mixture becomes more likely to react as pressure increases. Figure 1 presents the famous S-curve representing the pressure-temperature dependence of the H_2-O_2 explosion limits for gaseous reactant mixtures injected into a vessel. Explosion occurs to the right of the curve, details of which depend also on the size, shape, and wall properties of the chamber into which the mixture is admitted, while slow reaction or flame propagation may occur on the left, limits of flammability lying far below and to the left. The middle section of the curve, corresponding to the

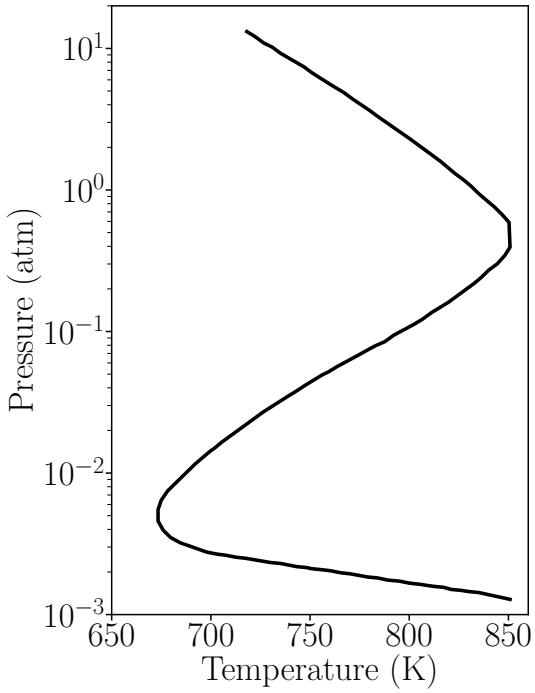

Fig. 1 Experimental explosion limits of a stoichiometric hydrogen-oxygen mixture in a 3.7 cm radius spherical vessel, from the classical Lewis & von Elbe textbook [1]. Explosion occurs to the right of the curve (towards higher temperatures)

so-called second explosion limit, exhibits the counter-intuitive behavior for which the reactivity decreases with increasing pressure. This behavior is often encountered under ambient conditions, as will be explained throughout this chapter. In particular, it will become obvious that there is a significant range of temperatures, overlapping with those of interest for engine design, within which ignition is more prompt at atmospheric pressure than under typical engine operating pressures.

The Chapter is organized as follows. Part 1 presents an in-depth analysis of the ignition-related H_2 kinetics, where only the chemistry of H_2 oxidation is investigated, omitting all transport phenomena. There, we shall introduce the notion of a crossover temperature, T_c, corresponding to the second explosion limit described above. The minimal kinetic description for H_2 ignition will also be introduced, to serve as a baseline for the remainder of the Chapter. Finally, useful analytical expressions for H_2 reactivity, ignition times, and radical-pool composition will be presented, to be used in ignition and safety studies.

Part 2 gives an overview of canonical processes involving H_2 kinetic limit phenomena. In particular, we shall study the link between the H_2 chemistry and the three explosion limits depicted in Fig. 1. The reaction-front propagation limits in premixed gases will be presented for both the deflagration (subsonic) and detonation (supersonic) regimes, along with appropriate simplified descriptions, different from that given earlier for autoignition. Recent results regarding the propagation limits in narrow channels will also be presented. Finally, ignition will be studied in a wide variety of configurations: mixing-layer ignition, thermal-induced (hot-wall) ignition, and even the recently investigated shock-induced ignition.

Part 3 intends to answer the (relatively easy) question: *How to ignite H_2?* In particular, we shall present the main principles of igniter design, from the combustion chamber topography, to the ignition sequence (fuel rich or oxidizer rich), and conclude with a suggested list of igniter technologies usable for H_2 ignition, including spark ignition, laser ignition, and the more unconventional acoustic ignition.

Part 4 tackles the (not so easy) opposite question: *How to avoid – or at least predict – H_2 hazardous ignition?* Through analysis of a numerical simulation of a turbulent H_2-air lifted flame – a configuration reminiscent of H_2 leaking into a hot environment, selected as a canonical example – we shall present tools to identify ignition kernels both *a posteriori* and, perhaps more interestingly, *a priori*.

The chapter concludes with a summary that indicates some of the open questions that the authors believe should be tackled in the near future to assist in the transition towards "carbon-free" combustion.

1 The chemistry of H_2 ignition

This section presents an analytical description of the kinetics involved in H_2 limit phenomena. It builds upon the derivation of analytical formulas for the ignition delays of arbitrary H_2–O_2–inert mixtures.

1.1 Preliminary definitions and notation

The notation largely follows the convention established by Poinsot and Veynante in their textbook [2]. The mixture is fully defined by providing the pressure p,

temperature T and mass-fraction composition vector Y_k (with k the species index). Their relation to the density is taken to be the perfect-gas law

$$p = \frac{\rho R T}{W}, \tag{1}$$

where $R = 8.314\,\mathrm{J\,mol^{-1}\,K^{-1}}$, and W is the mixture molecular weight, obtained from the component molecular weight W_k as

$$\frac{1}{W} = \sum_k \frac{Y_k}{W_k}. \tag{2}$$

Mole fractions are written as X_k, with

$$X_k = \frac{W}{W_k} Y_k. \tag{3}$$

The species molar concentration is denoted by C_k:

$$C_k = \rho \frac{Y_k}{W_k} = \rho \frac{X_k}{W}. \tag{4}$$

For a mixture of H_2–O_2 (potentially including other gases), the mixture's equivalence ratio φ is defined as

$$\varphi = \frac{X_{H_2}}{2X_{O_2}}. \tag{5}$$

As above, (e.g. X_{H_2}), the component index k can conveniently be replaced by the component symbol (H_2, O_2, N_2, ...) for easier reading.

1.2 Minimal kinetic description

It is generally accepted that the detailed description [3–8] of H_2 chemistry consists of 20 or more elementary reactions between 8 reactive species. Albeit that discrepancies remain between the detailed descriptions proposed (as is discussed later in this Chapter on H_2 kinetics), all agree on the elementary reactions listed in Tab. 1. A comparison of ignition times as obtained with selected reference detailed mechanisms is provided in Fig. 2. The specific definitions employed in generating these results are to be defined below. This figure, which is to be discussed in greater detail later, is exhibited here to provide a general indication of the extent to which the predictions differ at normal atmospheric pressure for different detailed mechanisms available in the current literature. It may be seen from this figure that agreement is excellent for both high and low temperatures, where differences in predicted ignition delays are less than a factor of two for the most part, while significant departures are found in the vicinity of the inflexion point (to be identified later as the second

Table 1 List of elementary reactions for hydrogen combustion, as extracted from the San Diego mechanism [3].

1	$H + O_2 \rightleftharpoons OH + O$	11	$HO_2 + H \rightleftharpoons H_2 + O_2$
2	$H_2 + O \rightleftharpoons OH + H$	12	$HO_2 + H \rightleftharpoons H_2O + O$
3	$H_2 + OH \rightleftharpoons H_2O + H$	13	$HO_2 + O \rightleftharpoons OH + O_2$
4	$H_2O + O \rightleftharpoons 2OH$	14	$HO_2 + OH \rightleftharpoons H_2O + O_2$
5	$2H + M \rightleftharpoons H_2 + M$	15	$2OH(+M) \rightleftharpoons H_2O_2(+M)$
6	$H + OH + M \rightleftharpoons H_2O + M$	16	$2HO_2 \rightleftharpoons H_2O_2 + O_2$
7	$2O + M \rightleftharpoons O_2 + M$	17	$H_2O_2 + H \rightleftharpoons HO_2 + H_2$
8	$H + O + M \rightleftharpoons OH + M$	18	$H_2O_2 + H \rightleftharpoons H_2O + OH$
9	$H + O_2(+M) \rightleftharpoons HO_2(+M)$	19	$H_2O_2 + OH \rightleftharpoons H_2O + HO_2$
10	$HO_2 + H \rightleftharpoons 2OH$	20	$H_2O_2 + O \rightleftharpoons HO_2 + OH$

explosion limit), at which point the differences in predicted temperatures span a total range of almost 100 K about the nominal 940 K value.

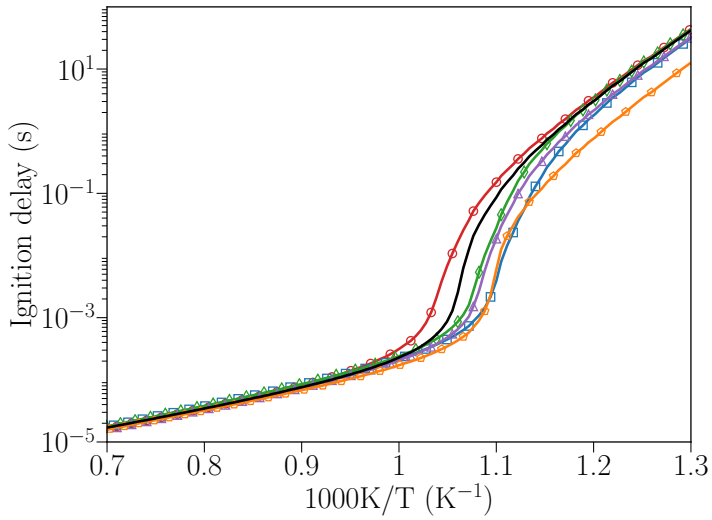

Fig. 2 Comparison of ignition times of H_2-air mixtures ($\varphi = 1$, $p = 1$atm), as obtained with selected detailed mechanisms.

Symbol	none	△	◇	o	⬠	□
Reference	[3]	[4]	[5]	[6]	[7]	[8]

Many of the elementary steps present in the detailed chemistry are unimportant during ignition. The reactants, being relatively stable, must generate radicals that serve as active intermediates accelerating ignition. The only steps that create radicals from the reactants are 5b, 7b, and 11b, where b stands for the backward reaction, with f to denote the forward. However, 5b and 7b describe reactant dissociation, which occurs only at very high temperature that do not arise in normal ignition events, whence 11b is generally dominant in initiating ignition. The radical H so

produced therefrom generates additional radicals through steps 1f, 2f and 3f. It also creates additional hydroperoxyl through step 9f, which, albeit less active than other radical, yet is important in forming hydrogen peroxide through steps 16f and 17b, since the latter can further enhance the active radical concentrations through step 15b. Hydroperoxyl also is quite effective in releasing heat through 16f, making it key radical in autoignition. The resulting 8 elementary steps, referred to from now on as the *skeletal mechanism*, constitute a reduced mechanism that yields sufficiently accurate descriptions of ignition for most purposes.

Table 2 Rate coefficients responsible for hydrogen ignition in Arrhenius form $k = AT^n \exp(-E_a/RT)$ for the skeletal mechanism, with numerical values of the San Diego mechanism [3].

	Reaction		A^a	n^a	E_a^a
1	$H+O_2 \rightarrow OH+O$		$3.52\ 10^{16}$	-0.7	71.42
2	$H_2+O \rightarrow OH+H$		$5.06\ 10^{4}$	2.67	26.32
3	$H_2+OH \rightarrow H_2O+H$		$1.17\ 10^{9}$	1.3	15.17
4	$H+O_2+M \rightarrow HO_2+M^b$	k_0	$5.75\ 10^{19}$	-1.4	0.0
		k_∞	$4.65\ 10^{12}$	0.44	0.0
5	$H_2+O_2 \rightarrow HO_2+H$		$2.93\ 10^{12}$	0.356	232.21
6[c]	$2HO_2 \rightarrow H_2O_2+O_2$		$1.03\ 10^{14}$	0.0	46.22
			$1.94\ 10^{11}$	0.0	-5,89
7	$HO_2+H_2 \rightarrow H_2O_2+H$		$7.80\ 10^{10}$	0.61	100.14
8	$H_2O_2+M \rightarrow 2OH+M^d$	k_0	$7.60\ 10^{30}$	-4.20	213.71
		k_∞	$2.63\ 10^{19}$	-1.27	214.74

[a] Units are mol, s, cm^3, kJ, and K.
[b] Chaperon efficiencies are 2.5 for H_2, 16.0 for H_2O, 0.7 for Ar and He and 1.0 for all other species; Troe falloff with $F_c = 0.5$
[c] Bi-Arrhenius (the sum of the two constants).
[d] Chaperon efficiencies are 2.0 for H_2, 6.0 for H_2O, 0.4 for Ar and He and 1.0 for all other species; $F_c = 0.265 \exp(-T/94\text{K}) + 0.735 \exp(-T/1756\text{K}) + \exp(-5182\text{K}/T)$

The list of 8 elementary reactions is provided in Tab. 2, along with values of the rate parameters as extracted from the San Diego detailed mechanism [3]. The corresponding file is also made available in Cantera format [9] at pierre-boivin.cnrs.fr. A significant advantage of this reduced mechanism is that it enables fully explicit predictions to be made for ignition delay times and other relevant quantities.

The skeletal description has been validated through a set of homogeneous-isobaric-reactor calculations, performed using the Cantera open-source software [9]. Two typical temperature and species histories in such a reactor are reported in Fig. 3. To address validation over a wide range of conditions, let us now define the ignition delay based on histories such as those plotted in Fig. 3.

Generally, the ignition delay is defined as the time of **maximum heat-release**, which coincides with the maximum of $\frac{\partial T}{\partial t}$ in Fig. 3, indicated by the two vertical dashed lines. Alternative definitions for ignition delays exist (such as the time required for the temperature to increase by 100 K), but general conclusions are found to remain similar so long as a single consistent criterion is maintained.

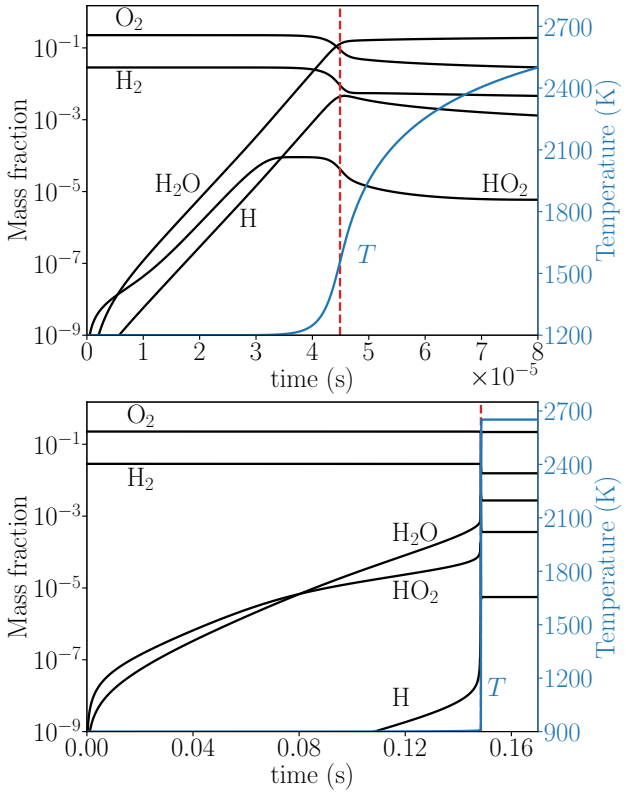

Fig. 3 Species and temperature evolution in a homogeneous isobaric reactor initially at $(p, T, \varphi) = (10^5\,\text{Pa}, 1200\,\text{K}, 1)$ (top) and $(p, T, \varphi) = (10^5\,\text{Pa}, 900\,\text{K}, 1)$ (bottom).

Figure 4 shows a comparison of ignition-delay predictions for stoichiometric H_2-air mixtures in adiabatic, isobaric reactors as obtained with the detailed (Tab. 1) and skeletal (Tab. 2) descriptions. Results from the two descriptions are seen to be in excellent agreement over wide ranges of pressure, temperature, and equivalence ratio, supporting the accuracy of the *skeletal description*.

The j^{th} reaction rate is denoted by ω_j, and the corresponding reaction-rate constant $k_j = AT^n \exp(-E/R^oT)$ appears in its proportionality to the product of the reactant concentrations for the elementary step in question, e.g.

$$\omega_1 = k_1 C_H C_{O_2}. \tag{6}$$

For reactions 4 and 8, the effective third-body concentration C_{M_j} is defined as the sum of the concentrations of each species, weighted by the chaperon efficiencies listed in the footnotes of the table, e.g. $\omega_4 = k_4 C_H C_{O_2} C_{M_4}$, with $C_{M_4} = 2.5C_{H_2} + 16C_{H_2O} + C_{O_2} + C_{N_2}$ for H_2-air mixtures with water addition. The complete system of equations for the evolution of the concentrations of the chemical species under

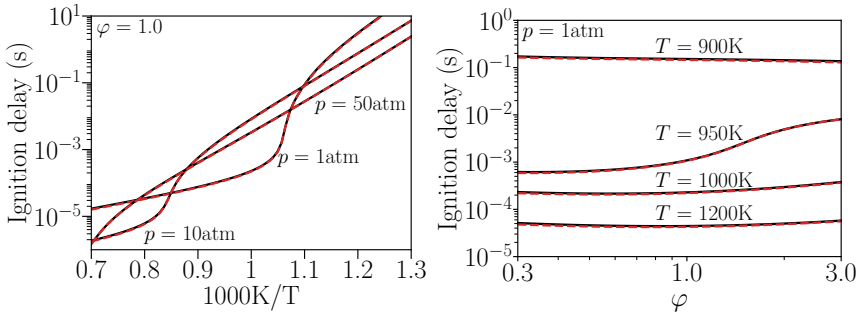

Fig. 4 Comparisons of ignition delays computed with detailed chemistry (solid curves) and 8-step skeletal chemistry (dashed curves) for hydrogen-air mixtures as a function of temperature (a) and equivalence ratio (b).

homogeneous, isobaric conditions then reads

$$\begin{cases} dC_{H_2}/dt & = -\omega_2 - \omega_3 - \omega_5 - \omega_7, \\ dC_{O_2}/dt & = -\omega_1 - \omega_4 - \omega_5 + \omega_6, \\ dC_{H_2O}/dt & = \omega_3, \\ dC_{H}/dt & = -\omega_1 + \omega_2 + \omega_3 - \omega_4 + \omega_5 + \omega_7, \\ dC_{O}/dt & = \omega_1 - \omega_2, \\ dC_{OH}/dt & = \omega_1 + \omega_2 - \omega_3 + 2\omega_8, \\ dC_{HO_2}/dt & = \omega_4 + \omega_5 - 2\omega_6 - \omega_7, \\ dC_{H_2O_2}/dt & = \omega_6 + \omega_7 - \omega_8. \end{cases} \tag{7}$$

These species-evolution equations (7) are coupled with an equation for energy conservation which, for a constant-pressure, adiabatic reactor, reads

$$\rho c_p \frac{dT}{dt} = -\sum_k h_k \frac{dC_k}{dt}, \tag{8}$$

where h_k is the enthalpy of formation per unit mass for species k, and the specific heat at constant pressure of the mixture, c_p, appears on the left-hand side. The system typically is simplified through a number of common approximations that are listed below.

A1 Reactants H_2, O_2 concentration variations can be neglected,

$$\frac{dC_{H_2}}{dt} = \frac{dC_{O_2}}{dt} = 0 \tag{9}$$

A2 Temperature variation can be neglected,

$$\frac{dT}{dt} = 0 \tag{10}$$

A3 Minor species (O, OH) satisfy the quasi-steady-state approximations (QSSA)[1],

$$\frac{dC_{\mathrm{O}}}{dt} = \frac{dC_{\mathrm{OH}}}{dt} = 0 \tag{11}$$

A4 The chemistry of (HO_2, H_2O_2) can be neglected,

$$\omega_6 = \omega_7 = \omega_8 = 0 \tag{12}$$

A5 Minor species (H, HO_2) are in quasi-steady state,

$$\frac{dC_{\mathrm{H}}}{dt} = \frac{dC_{\mathrm{HO_2}}}{dt} = 0. \tag{13}$$

Table 3 presents a selected list of analytical studies of H_2–O_2 ignition, along with the corresponding assumptions adopted in each investigation. The approximations differ, depending on whether the temperature is above or below the crossover temperature (denoted by T_c, to be defined explicitly later).

Table 3 Assumptions made in selected analytical studies of H_2–O_2 autoignition.

Authors, year	$T > T_c$	$T < T_c$
Asaba et al. 1965 [10]	A1, A2, A4	∅
Brokaw et al. 1965 [11]	A1, A2, A4	∅
Treviño et al. 1991 [12, 13]	A1, A3, A4	A1, A3
Treviño et al. 1994 [14]	A1, A2, A4	∅
Del Alamo et al. 2004 [15]	A1, A2, A3, A4	∅
Boivin et al. 2012 [16]	∅	A1, A3, A5
Boivin et al. 2017 [17]	A1, A2, A4	A1, A3, A5

1.3 A simplified study of high-temperature ignition – crossover definition

A low-order description of H_2 ignition in the high-temperature regime may be obtained by introducing the assumptions A1–A4 (9–12). The set of equations (7-8) then reduces to

$$\frac{dC_{\mathrm{H}}}{dt} = -\omega_1 + \omega_2 + \omega_3 - \omega_4 + \omega_5, \tag{14}$$

in which most terms involve concentrations of the QSSA species. This equation can be re-arranged on the basis of the quasi-steady-state assumptions to read:

$$\frac{dC_{\mathrm{H}}}{dt} \approx \frac{dC_{\mathrm{H}}}{dt} + 2\frac{dC_{\mathrm{O}}}{dt} + \frac{dC_{\mathrm{OH}}}{dt} = 2\omega_1 - \omega_4 + \omega_5. \tag{15}$$

[1] A short description of the Quasi-Steady-State Approximation (QSSA) is provided in Appendix 1.

This equation is fully decoupled from the others, showing that C_{H} satisfies the first-order differential equation

$$\frac{dC_{\mathrm{H}}}{dt} = (2k_1 - k_4 C_{\mathrm{M}_4}) C_{\mathrm{O}_2}.C_{\mathrm{H}} + k_5 C_{\mathrm{H}_2} C_{\mathrm{O}_2}, \quad C_{\mathrm{H}}(t=0) = 0, \tag{16}$$

corresponding to (half) the rate of global reaction $3\,\mathrm{H}_2 + \mathrm{O}_2 \longrightarrow 2\,\mathrm{H}_2\mathrm{O} + 2\,\mathrm{H}$. The solution to the differential equation is

$$C_{\mathrm{H}}(t) = \left(e^{(2k_1 - k_4 C_{\mathrm{M}_4}) C_{\mathrm{O}_2}.t} - 1 \right) \frac{k_5 C_{\mathrm{H}_2}}{2k_1 - k_4 C_{\mathrm{M}_4}}, \tag{17}$$

leading to an exponential growth of radical H so long as $2k_1 - k_4 C_{\mathrm{M}_4} > 0$, or, alternatively, $\alpha > 1$, where we have introduced the so-called crossover variable α.

The crossover parameter α is defined as

$$\alpha = \frac{2k_1}{k_4 C_{\mathrm{M}_4}}. \tag{18}$$

It measures the competition between H-atom branching to form additional active intermediates, the rate constant in the numerator, to its replacement by a less active intermediate, the rate constant in the denominator, during its interaction with oxygen molecules.

- $\alpha = 1$ corresponds to the second explosion limit,
- $\alpha > 1$ for temperature/pressure conditions above crossover,
- $\alpha < 1$ for temperature/pressure conditions below crossover.

At a given pressure, the temperature for which $\alpha = 1$ is called the crossover temperature T_c. The following relation holds:

$$\alpha > 1 \Leftrightarrow T > T_c.$$

Using the rates from Tab. 2 yields $T_c = 943$ K for a stoichiometric mixture of H_2-air at atmospheric pressure, but this value evidently depends on the choice of detailed mechanism, as shown in Fig. 2.

This definition (18) is in agreement with the classical result [1] that, at crossover, the rate of reaction $\mathrm{O}_2 + \mathrm{H} \rightarrow \mathrm{OH} + \mathrm{O}$ is half that of reaction $\mathrm{H} + \mathrm{O}_2 + \mathrm{M} \rightarrow \mathrm{HO}_2 + \mathrm{M}$. The dependence of the crossover variable α on pressure and temperature is the reason for non-trivial relation of the second explosion limit, as will be explained in Sec. 2.1.

The development can be extended to obtain an approximation for the ignition delay t_i. One possible explicit definition of the ignition delay is that the hydrogen atom concentration reaches a value equal to a minimum reactant concentration:

$$C_{\mathrm{H}}(t_i) = \min(C_{\mathrm{H}_2}, C_{\mathrm{O}_2}/2), \tag{19}$$

yielding

$$t_i = \frac{1}{(2k_1 - k_4 C_{M_4}) C_{O_2}} \ln\left(1 + \min\left(C_{H_2}, C_{O_2}/2\right) \frac{2k_1 - k_4 C_{M_4}}{k_5 C_{H_2}}\right). \quad (20)$$

This approximation provides a reasonable dependence of the ignition time on temperature, but it leads to a non-physical dependence on the equivalence ratio because of failure of O and OH steady-state assumptions [15, 18].

1.4 An eigenvalue study of the branching reactions

The main limitation of the above approach is failure of the O and OH steady-state assumptions A3 (11) [15, 18], which implicitly requires $(dC_O/dt, dC_{OH}/dt) \ll dC_H/dt$. Not only are H, O, and OH production rates of the same order, as evidenced by the radical-pool composition presented later, but also the balance between each of their rates is fundamental in obtaining the correct dependence of the ignition time on the equivalence ratio, as well as in identifying the most reactive mixture. The development can nonetheless be carried out without these assumptions, as shown below.

Keeping only assumptions A1, A2, A4 (9, 10, 12) yields

$$\frac{\mathrm{d}\bar{C}}{\mathrm{d}t} = \mathbf{A}\bar{C} + \bar{\epsilon}, \quad (21)$$

where

$$\bar{C} = \left[C_H \; C_O \; C_{OH} \; C_{HO_2} \; C_{H_2O_2}\right]^\intercal \quad (22)$$

is the radical-concentration vector,

$$\mathbf{A} = \begin{bmatrix} -(k_1 + k_4 C_{M_4}) C_{O_2} & k_2 C_{H_2} & k_3 C_{H_2} & k_7 C_{H_2} & 0 \\ k_1 C_{O_2} & -k_2 C_{H_2} & 0 & 0 & 0 \\ k_1 C_{O_2} & k_2 C_{H_2} & -k_3 C_{H_2} & 0 & 2k_8 C_{M_8} \\ k_4 C_{O_2} C_{M_4} & 0 & 0 & -k_7 C_{H_2} & 0 \\ 0 & 0 & 0 & k_7 C_{H_2} & -k_8 C_{M_8} \end{bmatrix} \quad (23)$$

is the Jacobian matrix corresponding to the chain-branching chemistry, and

$$\bar{\epsilon} = \left[\omega_5 \; 0 \; 0 \; \omega_5 \; 0\right]^\intercal \quad (24)$$

is the vector containing the initiation rate. To simplify the notation the inverse characteristic times for each reaction $l_1 = k_1 C_{O_2}$, $l_2 = k_2 C_{H_2}$, etc., are introduced, yielding

$$\mathbf{A} = \begin{bmatrix} -(l_1 + l_4) & l_2 & l_3 & l_7 & 0 \\ l_1 & -l_2 & 0 & 0 & 0 \\ l_1 & l_2 & -l_3 & 0 & 2l_8 \\ l_4 & 0 & 0 & -l_7 & 0 \\ 0 & 0 & 0 & l_7 & -l_8 \end{bmatrix}. \quad (25)$$

The solution to (21) with initial conditions $\bar{C}(t=0)=0$ can be cast in the form

$$\bar{C} = \sum_{i=1,5} a_i \bar{V}_i e^{\lambda_i t} + \bar{C}_0, \tag{26}$$

involving the eigenvalues λ_i and associated eigenvectors $\bar{V}_i$ of the Jacobian matrix $\mathbf{A}$ along with the particular solution $\bar{C}_0$, obtained by solving $\mathbf{A}\bar{C}_0 + \bar{\epsilon} = 0$. The coefficients a_i are determined by imposing the initial (null) condition $\sum_{i=1,5} a_i \bar{V}_i + \bar{C}_0 = 0$.

The set of eigenvalues λ_i, obtained as solutions to the characteristic equation associated with $\mathbf{A}$, includes one or more positive real value. Because of the exponential growth of the solution, the largest eigenvalue, denoted by λ with associated coefficient a and eigenvector $\bar{V} = (V_{\mathrm{H}}, V_{\mathrm{O}}, V_{\mathrm{OH}}, V_{\mathrm{HO_2}}, V_{\mathrm{H_2O_2}})$, soon becomes dominant, so that (26) simplifies for $\lambda t \gg 1$ to

$$\bar{C} = a\bar{V}e^{\lambda t}. \tag{27}$$

This equation provides a sufficiently accurate description of the intermediate-species evolution during the first stages of ignition, irrespective of whether the temperature is above or below crossover. This is shown in Fig. 5, which compares results of numerical integrations with the predictions obtained from (27) for the H-atom mole fraction $X_{\mathrm{H}} = (aV_{\mathrm{H}}e^{\lambda t})/[p/(RT)]$ and $\mathrm{HO_2}$ mole fraction $X_{\mathrm{HO_2}} = (aV_{\mathrm{HO_2}}e^{\lambda t})/[p/(RT)]$.

This linearized approach remains valid until the rate of reaction 6 – the only one not included in this description – becomes important. From Eq. (27), it is straightforward to write the time at which this occurs as

$$t_B = \lambda^{-1} \ln\left(\frac{\lambda}{2ak_6 V_{\mathrm{HO_2}}}\right), \tag{28}$$

which defines the instant at which $\mathrm{HO_2}$ reaches a steady state, calculated by equating the $\mathrm{HO_2}$ production rate $\lambda a V_{\mathrm{HO_2}} e^{\lambda t}$ to its consumption rate by step 6, expressed in the form $2k_6 C_{\mathrm{HO_2}}^2 = 2k_6 (aV_{\mathrm{HO_2}} e^{\lambda t})^2$, with $V_{\mathrm{HO_2}}$ denoting the fourth component of the eigenvector $\bar{V}$ associated with the largest real eigenvalue λ.

The time t_B computed from (28) is identified in Fig. 5 as the end point for the dashed lines evaluated from (27). As can be seen, at high temperature $T > T_c$ the H-atom mole fraction grows to significant values ~ 0.1 at the end of the branching stage, with the temperature beginning to increase appreciably for $t > t_B$ as a result of the subsequent radical recombination. Under those high-temperature conditions, therefore, the prediction for t_B becomes a prediction for the induction time t_i.

The behavior encountered at low temperatures ($T < T_c$) is markedly different, however, as is seen in Fig. 5 from the computations with $T = 900\,\mathrm{K}$. The radical concentration is negligibly small at the end of the branching period, which is followed by a stage of comparable duration ending with a rapid temperature increase. For low temperatures, therefore, the prediction of the induction time t_i requires consideration of two different stages, the second of which, for $t_B < t < t_i$, being a thermal explosion occurring with all radicals (H, O, OH, $\mathrm{HO_2}$) in steady state. The thermal-explosion

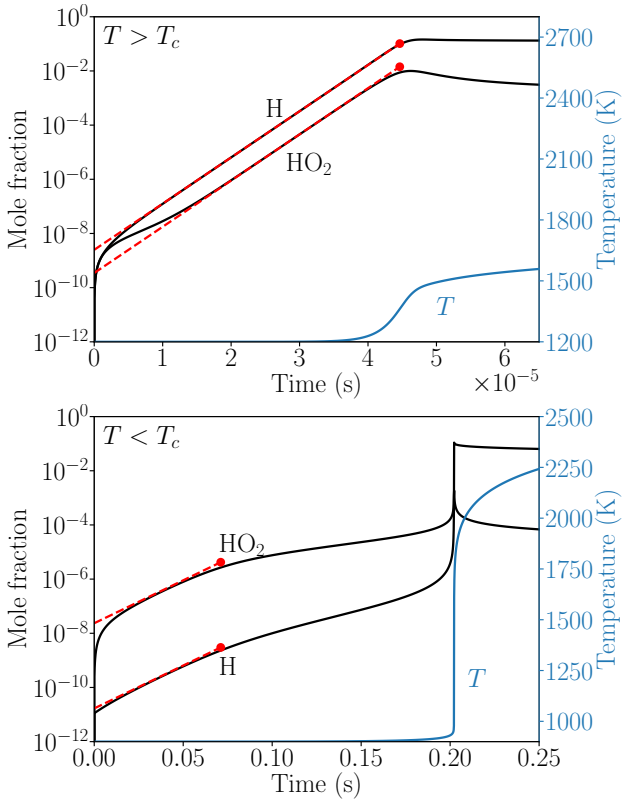

Fig. 5 H and HO_2 mole fractions and temperature as functions of time, during isobaric homogeneous ignition processes from numerical integrations with the 8-step skeletal chemistry for $\varphi = 1$, p =1 atm, with $T = 1200\,\mathrm{K} > T_c$ (top) and $T = 900\,\mathrm{K} < T_c$ (bottom); the H and HO_2 mole fractions evaluated with use of Eq. (27) are shown as dashed lines.

stage will be seen in Sec. 1.7 to become dominant as the temperature decreases, so that for temperatures sufficiently below crossover the branching stage can be neglected in a first approximation in providing predictions for t_i, as was done earlier for hydrogen-air ignition [16].

1.5 Radical-pool composition

Although the coefficients a and λ in Eq. (28) cannot be obtained analytically for the 5×5 matrix system, analytical results can be derived by studying regimes above and below the crossover temperature.

The separate branched-chain-explosion descriptions given below will account for the markedly different composition of the radical pool found for $\alpha > 1$

and $\alpha < 1$. This composition is exhibited most clearly by the normalized form $(V_{\rm H}, V_{\rm O}, V_{\rm OH}, V_{\rm HO_2}, V_{\rm H_2O_2})/(V_{\rm H} + V_{\rm O} + V_{\rm OH} + V_{\rm HO_2} + V_{\rm H_2O_2})$ of the eigenvector $\bar{V}$ associated with the dominant eigenvalue, which is used in Fig. 6 to illustrate the dependence on temperature of the radical-pool content for a stoichiometric H_2-air mixture at atmospheric pressure. The vertical dashed line indicates the crossover condition ($\alpha = 1$). It is clear that, at high temperatures, H, O, and OH are the main radicals responsible for ignition, while HO_2 and H_2O_2 are dominant for temperatures below crossover.

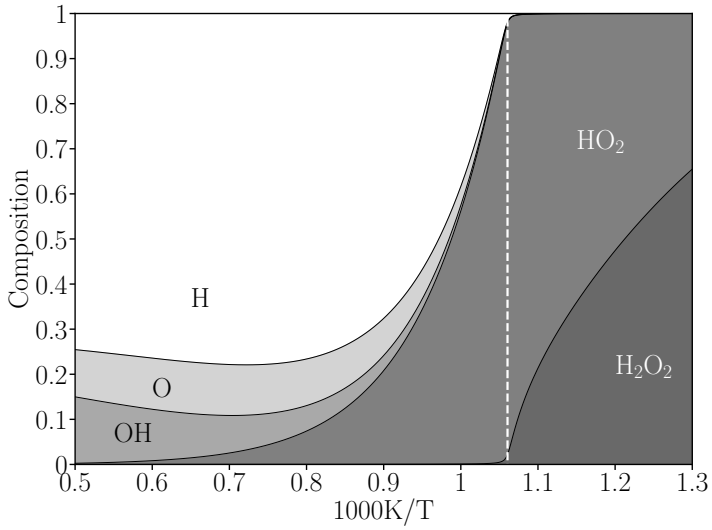

Fig. 6 Radical-pool composition obtained from the normalized eigenvector associated with the dominant eigenvalue for p=1atm, φ=1. The vertical line indicates the crossover $\alpha = 1$.

Note that, given the eigenvalue λ (to be derived later in Eq. 42), the corresponding eigenvector can be analytically obtained as

$$\begin{cases} V_{\rm H} & = 1 \\ V_{\rm O} & = l_1 V_{\rm H}/(l_2+\lambda) \\ V_{\rm OH} & = \left(l_1 V_{\rm H} + l_2 V_{\rm O} + 2 l_8 V_{\rm H_2O_2}\right)/(l_3+\lambda) \\ V_{\rm HO_2} & = l_4 V_{\rm H}/(l_7+\lambda) \\ V_{\rm H_2O_2} & = l_7 V_{\rm HO_2}/(l_8+\lambda)\,, \end{cases} \tag{29}$$

which can be used to express Fig. 6 in a fully analytical manner.

1.6 Analytical derivation of branching times

Let us now present fully analytical expressions for the branching times. More details are available in [17]. Hereafter, the superscript $^+$ will denote quantities valid above crossover ($\alpha > 1$), while $^-$ will apply for $\alpha < 1$.

1.6.1 Branching above crossover $\alpha > 1$

Above crossover, the main branching species are H, O, and OH, so that the system (25) reduces to a 3×3 system, corresponding to the upper left block of the linear system:

$$\mathbf{A}^+ = \begin{bmatrix} -(l_1 + l_4) & l_2 & l_3 \\ l_1 & -l_2 & 0 \\ l_1 & l_2 & -l_3 \end{bmatrix} \tag{30}$$

The eigenvalues of $\mathbf{A}^+$ are obtained as the solution of the characteristic polynomial

$$\det\left[\mathbf{A}^+ - \lambda \mathbf{I}\right] = \lambda^3 + a_2\lambda^2 + a_1\lambda + a_0 = 0, \tag{31}$$

where

$$\begin{cases} a_0 &= (l_4 - 2l_1)l_2l_3 \\ a_1 &= l_2l_3 + l_4(l_2 + l_3) \\ a_2 &= l_1 + l_2 + l_3 + l_4. \end{cases} \tag{32}$$

This characteristic polynomial admits three solutions, λ_1, λ_2, and λ_3, only one of which is positive, $\lambda_1 = \lambda^+$. This is seen in Fig. 7, which shows the variation with the equivalence ratio φ of the three eigenvalues, λ_1, $-\lambda_2$, and $-\lambda_3$ at atmospheric pressure for a temperature of 1100K. The figure also shows the accompanying variation of the main characteristic chain-branching times appearing in $\mathbf{A}^+$. As can be seen, λ_2 and λ_3 are both negative, and they are much larger in norm than $\lambda_1 = \lambda^+$, validating the fact that the branching can be described with only one eigenmode (27).

The analytical solution of the cubic polynomial (31) leads to a fairly complicated expression [15] that can, however, be simplified by noting that a_2 is always much greater than λ^+, so that in computing this eigenvalue the cubic term in (31) can be neglected in the first approximation. This is illustrated in Fig. 7, which shows that, for any mixture fraction, λ_1 is much smaller than at least one of the rate terms l_1, l_2, and l_3 that appear in the expression for a_2. The resulting quadratic equation for λ can then be solved explicitly to give

$$\lambda^+ = \frac{\sqrt{a_1^2 - 4a_0a_2} - a_1}{2a_2}, \tag{33}$$

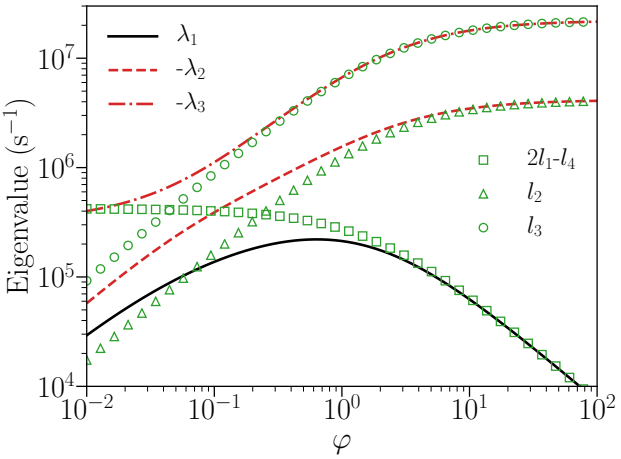

Fig. 7 The variation with equivalence ratio of the the three eigenvalues λ_1 (triangles), $-\lambda_2$ (squares), and $-\lambda_3$ (circles) and of the reaction rates $2l_1 - l_4$ (solid curve), $2l_1$ (dashed curve), l_2 (dot-dashed curve), and l_3 (dotted curve) as obtained for p =1 atm, T = 1100K.

with the a_i defined in (32). Note that similar simplifications to the characteristic polynomial (31) were investigated by Brokaw as early as 1965 [11], but with less accurate results, the detailed rate parameters being less well developed at that time.

1.6.2 Branching below crossover $\alpha < 1$

For temperatures below crossover, H and O, and OH are present in negligible quantities, as testified by the radical-pool composition (see Fig. 6), so their rates can be assumed to be negligible $dC_H/dt = dC_O/dt = dC_{OH}/dt = 0$ to give

$$-(l_1 + l_4)C_H + l_2C_O + l_3C_{OH} + l_7C_{HO_2} + \omega_5 = 0 \tag{34}$$

$$l_1C_H - l_2C_O = 0 \tag{35}$$

$$l_1C_H + l_2C_O - l_3C_{OH} + 2l_8C_{H_2O_2} = 0. \tag{36}$$

Adding (34) and (36) to eliminate C_{OH} and using (35) to eliminate C_O in the resulting equation leads to

$$k_4C_{O_2}C_{M_4}C_H = [l_7C_{HO_2} + 2l_8C_{H_2O_2} + \omega_5]/(1 - \alpha) \tag{37}$$

as an expression for the H-atom recombination rate. This last equation can be used in (21) to produce the simplified branching problem

$$\frac{d}{dt}\begin{bmatrix} C_{HO_2} \\ C_{H_2O_2} \end{bmatrix} = \begin{bmatrix} \frac{\alpha l_7}{1-\alpha} & \frac{2l_8}{1-\alpha} \\ l_7 & -l_8 \end{bmatrix} \cdot \begin{bmatrix} C_{HO_2} \\ C_{H_2O_2} \end{bmatrix} + \begin{bmatrix} \frac{\epsilon^-}{1-\alpha} \\ 0 \end{bmatrix}, \tag{38}$$

where

$$\epsilon^- = (2-\alpha)\omega_5 \tag{39}$$

is a measure of the reduced initiation rate. The associated characteristic equation for the Jacobian matrix in (38) can be solved to give

$$\lambda^- = \frac{\sqrt{b_1^2 - 4b_0b_2} - b_1}{2b_2}, \tag{40}$$

where

$$\begin{cases} b_0 &= -l_7 l_8 (2+\alpha) \\ b_1 &= l_8(1-\alpha) - \alpha l_7 \\ b_2 &= 1-\alpha. \end{cases} \tag{41}$$

A formula valid for all values of $\alpha \in [0, \infty]$

. The above formulations were improved in [17] to provide an excellent approximation for the full 5×5 system as

$$\lambda^{\pm} = [(C_1^2 - 4C_0)^{1/2} - C_1]/2, \tag{42}$$

involving the coefficients

$$C_0 = \lambda^+ \lambda^- \tag{43}$$

$$C_1 = \lambda^- \frac{1-\alpha}{(2+\alpha)} - \lambda^+. \tag{44}$$

Figure 8 presents a comparison between the exact maximum positive eigenvalue λ of the 5×5 linear system (25), as well as the three analytical predictions derived above:

- λ^+ (33), valid for $\alpha \gg 1$,
- λ^- (40), valid for $\alpha \ll 1$,
- and $\lambda^{\pm}$ (42), valid for $\alpha \in [0, \infty]$.

Agreement is seen to be excellent, validating the present approach. Less accurate approximate expressions for λ may be found in the literature as early as 1965 [11].

1.6.3 Branching-time expression

From the above expressions and their respective associated branching times [17], a general formula valid for the entire range of temperature can be obtained as

$$t_B = \lambda^{-1} \ln[(1+\alpha)\lambda^2/(2k_6\omega_5)]. \tag{45}$$

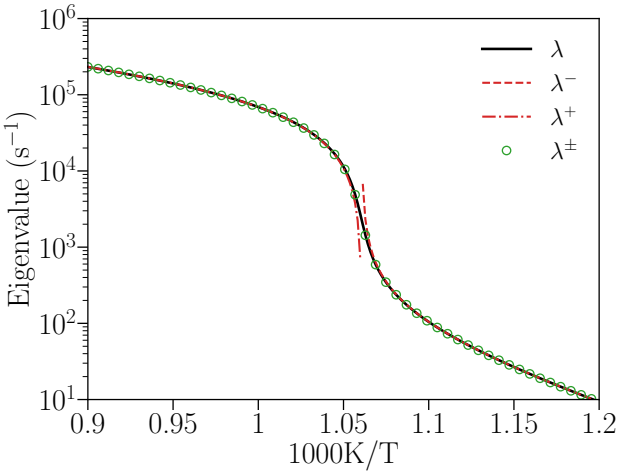

Fig. 8 Variation with temperature of the exact eigenvalue λ of the 5×5 linear system (25), λ^+ (33), λ^- (40) and $\lambda^\pm$ (42), for a stoichiometric H_2-air mixture at 1atm.

Excellent agreement is obtained between the analytical prediction (45) and detailed integration of the branching time, as is seen in Fig. 9. The remaining difference between branching time (to reach HO_2 steady state) and ignition time (to reach maximum heat release) below crossover is accounted for by the thermal-runaway stage described in the next Section.

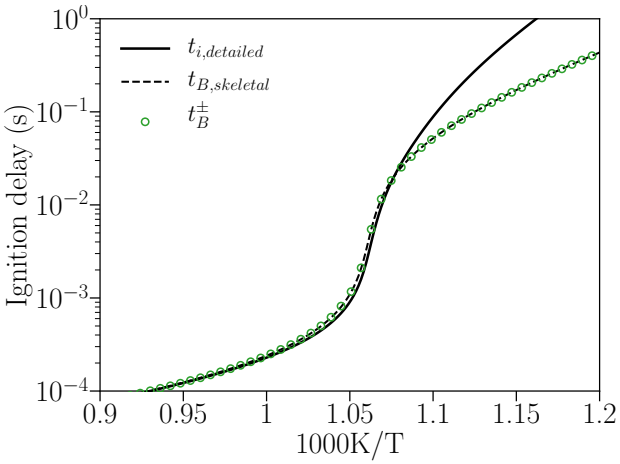

Fig. 9 Ignition delay t_i (thick solid line) determined numerically with the 20-step San Diego mechanism for a stoichiometric hydrogen-air mixture at atmospheric pressure. The thin dashed line represents the branching time t_B evaluated from Eq. (28), and the circles representing predictions obtained from Eq. (45).

Having derived an expression for the induction time t_B (45), the reason for the failure of O and OH steady states (15) during this stage, indicated at the beginning of the full Jacobian eigen study of Sec. 1.4, is now clear:

- The H, O, and OH growth rates are of the same order (see Fig. 6), resulting in (15) being a poor approximation : Together, O and OH represent close to 25% of the radical-pool content at stoichiometric conditions, and over 50% close to the lean flammability limit.
- The simplified formula for t_i (20) obtained using O and OH QSSA yields a main temperature dependence $\sim (2l_1 - l_4)^{-1}$, instead of the result $\sim \lambda^{-1}$ in (45). Upon comparing the inverse-characteristic-time ($2l_1 - l_4$ and λ) equivalence-ratio dependences seen in Fig. 7, it becomes clear that the former approximation does not exhibit the expected maximum at the most-reactive mixture ratio, while the latter does. The two formulations, however, do asymptotically approach each other in the rich limit.

1.7 Thermal runaway

As observed in Fig. 5, ignition below crossover proceeds in a two-stage process, with a thermal explosion following the initial branched-chain period investigated above. To analyze the thermal runaway it is reasonable to assume that approximations (A1, A3, A5) hold. The steady-state assumptions for H, O, OH, HO_2 lead to a two-step reduced mechanism derived from the skeletal mechanism, with overall reactions

$$H_2 + O_2 \xrightarrow{\text{I}} H_2O_2$$
$$2H_2 + O_2 \xrightarrow{\text{II}} 2H_2O,$$

and associated rates

$$\omega_{\text{I}} = \frac{2-\alpha}{2(1-\alpha)}\omega_7 \tag{46}$$
$$\omega_{\text{II}} = 2\omega_8. \tag{47}$$

The above expressions involve the elementary reaction rates (ω_7, ω_8). In evaluating $\omega_7 = l_7 C_{HO_2}$, a simplified steady-state expression is introduced,

$$C_{HO_2} = \sqrt{\frac{l_8 C_{H_2O_2}}{k_6(1-\alpha)}}, \tag{48}$$

neglecting contributions from the elementary reaction 7, an excellent approximation under most conditions [16]. With reactant consumption neglected, the homogeneous ignition history associated with the above reduced chemistry can be obtained by integration of

$$\begin{cases} \dfrac{\mathrm{d}C_{\mathrm{H_2O_2}}}{\mathrm{d}t} & = \omega_{\mathrm{I}} \\ \rho c_p \dfrac{\mathrm{d}T}{\mathrm{d}t} & = Q\omega_{\mathrm{II}} \end{cases}$$

with initial temperature $T = T_o$ and initial H_2O_2 concentration $C_{\mathrm{H_2O_2}} = 0$, the concentration of H_2O_2 produced in the earlier branching stage being negligible here. In the formulation ρ and c_p are the initial values of the density and specific heat at constant pressure. The heat released by reaction I has been neglected in the energy equation, since its contribution is small compared with that of the other two reactions, which have been expressed in terms of the global heat release of reaction II, which is

$$Q = -2h_{\mathrm{H_2O}}, \tag{49}$$

depending only on the enthalpy of formation of water, $h_{\mathrm{H_2O}} = -241.8$ kJ/mol.

The analysis proceeds by noting that the activation energies of the overall reaction-rate constants k_8, and $k_7(k_8/k_6)^{1/2}$, appearing in ω_{I} upon substitution of (48) are very similar, so that a single dimensionless activation energy $\beta = E_8/(R^oT_o) + n_8$, based for definiteness on the low-pressure rate parameters $n_8 = -4.20$ and $E_8 = 213.71$ kJ/mol of the elementary rate constant $k_8 = A_8T^{n_8}\exp[-E_8/(R^oT)]$, characterizes the strong temperature dependence of rates ω_7 and ω_8. For large values of β, introduction of the rescaled variables

$$\theta = \beta\frac{T - T_o}{T_o}, \quad \varphi = (\beta q X)^{2/3}\frac{C_{\mathrm{H_2O_2}}}{C_{\mathrm{M_8}}}, \quad \text{and} \quad \tau = \frac{(\beta q)^{1/3}}{(1-\alpha)}X^{-2/3}l_8 t \tag{50}$$

reduces the problem to the integration of

$$\begin{cases} \dfrac{\mathrm{d}\varphi}{\mathrm{d}\tau} & = \varphi^{1/2}e^{\theta} \\ \dfrac{\mathrm{d}\theta}{\mathrm{d}\tau} & = \varphi e^{\theta} \end{cases} \tag{51}$$

with initial conditions $\varphi(0) = \theta(0) = 0$. The constant k_8 in the definition of τ and the reaction-rate parameter

$$X = \frac{2C_{\mathrm{M_8}}\sqrt{k_8k_6(1-\alpha)}}{(2-\alpha)l_7} \tag{52}$$

are to be evaluated at the initial conditions. The above expressions involve the dimensionless effective heat of reaction

$$q = \frac{QC_{\mathrm{M_8}}}{\rho c_p T_o}. \tag{53}$$

Dividing the second equation of (51) by the first provides $\theta = \frac{2}{3}\varphi^{3/2}$ upon integration, leading to the dimensionless thermal-explosion time

$$\tau_E = \int_0^\infty \frac{\mathrm{d}\varphi}{\varphi^{1/2} \exp\left(\frac{2}{3}\varphi^{3/2}\right)}. \tag{54}$$

This integral takes the value

$$\tau_E = (2/3)^{2/3}\Gamma(1/3) \simeq 2.0444, \tag{55}$$

where the Γ function $\Gamma(z) = \int_0^\infty x^{z-1}e^{-x}dx$ is introduced. The definition of the dimensionless time τ given in (50) can be employed to show that the dimensional explosion time is

$$t_E = \frac{X^{2/3}(1-\alpha)}{(\beta q)^{1/3} l_8}\tau_E. \tag{56}$$

Typical results obtained for the explosion time t_E are presented in Fig. 10, showing an excellent agreement with the detailed integration in the low-temperature range $\alpha \ll 1$. Since the present stage can be triggered only after HO_2 has reached steady state, e.g. after the branching duration t_B, the induction duration may be obtained as the sum $t_B + t_E$. The evolution of t_B, and $t_B + t_E$ are included in Fig. 10, exhibiting excellent agreement.

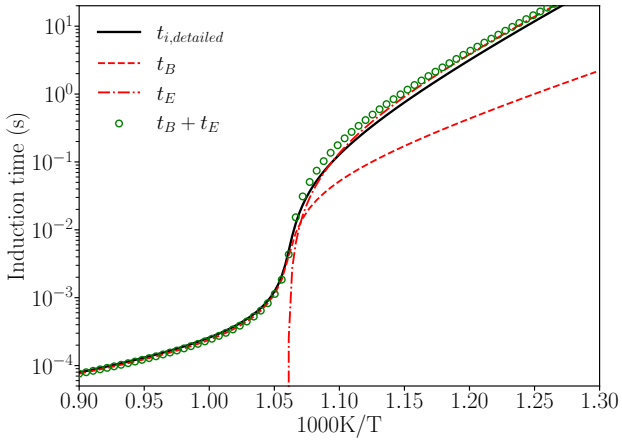

Fig. 10 The solid curve represents the variation with temperature of the induction time t_i obtained numerically with detailed chemistry for a stoichiometric hydrogen-air mixture with at $p = 1$ atm. The dashed curves are evaluated from (45) and (56) for those same conditions, with the circles representing the sum $t_B + t_E$.

1.8 Recap: analytical formulas for H_2 induction times

The induction time can be obtained analytically as the sum of

- the branching time t_B (45), time for HO_2 to reach a steady state, and
- the explosion time t_E (56), time of the thermal runaway, present for $\alpha < 1$.

Figure 11 shows the reasonable agreement obtained for the above formulation, over a wide range of pressure, temperature and equivalence ratios.

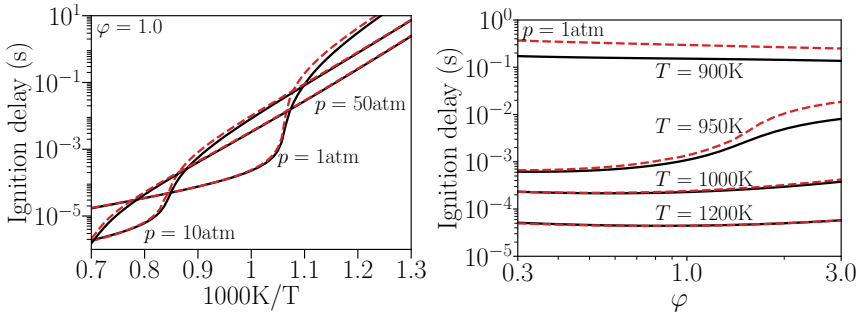

Fig. 11 Comparison of ignition delays t_i in air obtained by numerical integrations for the complete 20-step chemistry (solid curves) with the analytical prediction $t_i = t_B + t_E$ (dashed curves).

2 Limit phenomena in canonical flow configurations

We have now described in-depth the basic chemistry behind H_2 ignition. Once the chemical ignition time is known, the various problems of ignition limits all come down to comparing this chemical timescale with a given problem timescale (e.g. convective or diffusive timescales). This section aims at providing a wide overview of such problems. Attention will be directed to the seven canonical experimental scenarios listed in Tab. 4.

2.1 Explosion in a closed vessel: the three explosion limits

This section presents the link between the derivation presented in Sec. 1 and the three explosion limits presented in Introduction. A sketch of an explosion in a spherical vessel is provided in Fig. 12. The vessel, of radius a, is initially filled with a homogeneously premixed mixture of H_2–O_2 at a certain pressure and temperature. The (p, T) values separating explosive and non-explosive domains define the so-called explosion limits, shown in Fig. 13. The curve clearly exhibits three sections, referred to as the first, second, and third explosion limits, in order of ascending pressure. As indicated in Sec. 1.3, the counter-intuitive character of the second explosion limit, pointed out in the introduction, is a consequence of the fact that it corresponds exactly to the crossover conditions $\alpha = 1$, or $2l_1 = l_4$, identified in Fig. 13

Table 4 List of canonical experimental scenarios of Sec. 2.

#	Phenomenon	Description
1	explosion limit	Explosion of a mixture initially at rest in a closed vessel, corresponding to the experiment by Lewis & von Elbe [1].
2	flammability limit	Subsonic propagation limit of a reactive front (deflagration) in premixed gases. Planar case, and multi-dimensional effects.
3	detonability limit	Supersonic propagation limit of a reactive front (detonation) in premixed gases. Planar case, and multi-dimensional effects.
4	flame lift-off	Ignition in an evolving mixing layer downstream from a splitter plate, as in a high-speed-jet lifted flame or a fuel leak into a hot environment.
5	wall ignition	Ignition induced by the heat fluxes from hot walls in natural or forced convection.
6	shock ignition	Ignition induced by the thermodynamic-property jumps across a shock discontinuity.
7	extinction limit	Extinction limit of strained diffusion flames.

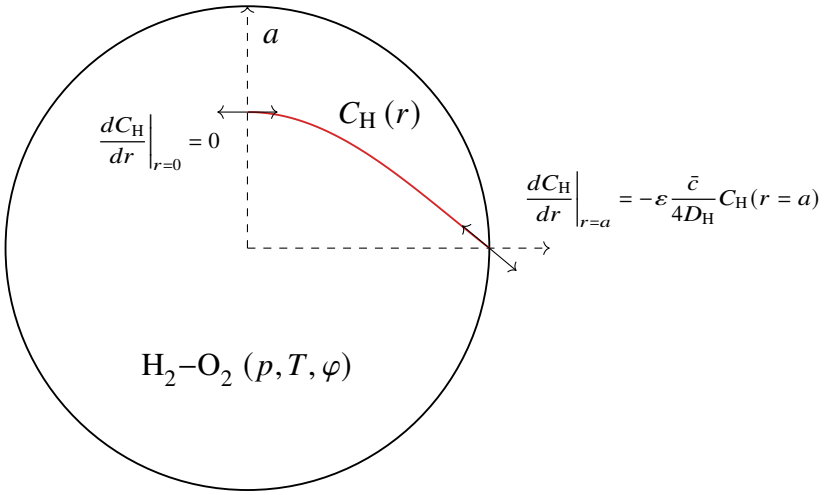

Fig. 12 Sketch of the problem of an explosion in a closed vessel for a sphere of radius a.

as the dotted line; the unexpected pressure dependence is due to the fact that reaction 4 involves a third body which produces a cubic (third-order) pressure dependence, while reaction 1 is of second order. The first and third explosion limits are a result of competition between the branched-chain reaction, occurring in the center of the vessel, and diffusion of intermediate species, necessary for that branching, to the vessel walls, where their destruction occurs by heterogeneous reactions.

2.1.1 A spherical-diffusion approach

A straightforward approach, originally considered more than 85 years ago [19,20], is to address the problem sketched in Fig. 12, in spherical coordinates. This, in general,

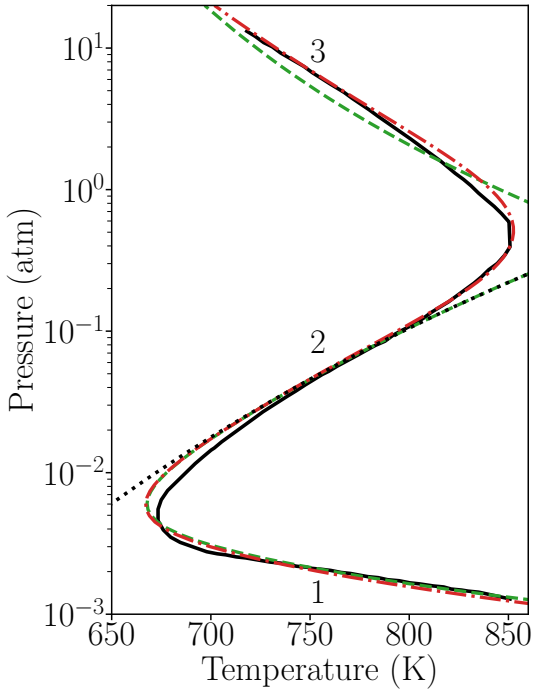

Fig. 13 Explosion limits of a stoichiometric hydrogen-oxygen mixture in a spherical vessel of radius $a = 3.7$ cm. Experimental (solid curves) data are extracted from [1]. Numerical values are shown for two different approaches, one, the dashed curves, is obtained by solving equations (62) and (67), while the other, the dot-dashed curves, is obtained through equation (66). The dotted line corresponds to the extended second-explosion-limit condition $\alpha = 1$.

involves solving differential equations in r, expressing steady-state diffusion-reaction balances, for each of the five reaction intermediaries, bringing in the diffusion coefficients, D_k for each species k. Since the diffusion coefficient of the H atom exceeds that of any other species by more than a factor of three, a potentially useful simplification is obtained by retaining only the H contribution (as in Sec. 1.3) to obtain

$$-\frac{1}{r^2}\frac{\partial}{\partial r}\left(r^2\frac{\partial}{\partial r}D_{\mathrm{H}}.C_{\mathrm{H}}\right) = (2l_1 - l_4).C_{\mathrm{H}}. \tag{57}$$

Subject to the condition $\frac{dC_{\mathrm{H}}}{dr} = 0$ at $r = 0$, this equation can be integrated to give

$$C_{\mathrm{H}} = (C/r)\sin\left(r\sqrt{((2l_1 - l_4)/D_{\mathrm{H}})}\right), \tag{58}$$

where C is an integration constant. If H is consumed completely at the walls, then

$$a\sqrt{(2l_1 - l_4)/D_{\mathrm{H}}} = \pi, \tag{59}$$

but, as described in [20], this largely overestimates the extent of H destruction at the wall, whence the boundary condition is better described through imposition of a finite catalytic destruction rate at the wall, such as

$$- D_{\mathrm{H}} \frac{dC_{\mathrm{H}}}{dr}(r = a) = \varepsilon \frac{\bar{c}}{4} C_{\mathrm{H}}(r = a), \tag{60}$$

where ε is the sticking coefficient – the fraction of molecules being destroyed upon reaching the vessel wall (typically 10^{-5} to 10^{-2}) – and $\overline{c}$ is the average molecular velocity [21],

$$\overline{c} = \sqrt{\frac{8RT}{\pi W}}. \tag{61}$$

Introducing the wall catalytic destruction of radicals then result in modifying the critical radius for explosion as

$$a\sqrt{(2l_1 - l_4)/D_{\mathrm{H}}} \approx 0.534, \tag{62}$$

which corresponds to a sticking coefficient of $0.72\sqrt{D_{\mathrm{H}}\lambda}/\bar{c}$, around 0.001. The lower part of the dashed curve in Figure 13 was obtained employing equation (62), showing excellent agreement with the experimental data from Lewis & von Elbe [1].

2.1.2 A Jacobian-based approach

A simpler approach for deriving explosion limits can be found in work of C.K. Law and coworkers [22, 23]. The problem is assumed to be zero-dimensional, with the rate of removal of intermediate species at the wall embedded directly into the chemical-kinetic Jacobian (25).

The destruction rate of intermediate species at the wall is of first order, being proportional to the species concentration, with an (inverse-time) rate constant k defined as

$$k_{k,w} = \frac{1}{4} \varepsilon_k \bar{c}_k \frac{S}{V}, \tag{63}$$

much like in (60), where S/V is introduced as the surface-to-volume ratio of the vessel ($S/V = 3/a$ for the spherical case), and average molecular velocities $\bar{c_k}$ and sticking coefficients ε_k being different for each species.

With radicals destruction at the wall added in this zero-dimensional formulation, Eq. (21) becomes

$$\frac{\mathrm{d}\bar{C}}{\mathrm{d}t} = \mathbf{A}'\bar{C} + \bar{\epsilon}, \tag{64}$$

where A' now includes wall-destruction terms along its diagonal

$$\mathbf{A}' = \begin{bmatrix} -l_1 - l_4 - k_{\mathrm{H},w} & l_2 & l_3 & l_7 & 0 \\ l_1 & -l_2 - k_{\mathrm{O},w} & 0 & 0 & 0 \\ l_1 & l_2 & -l_3 - k_{\mathrm{OH},w} & 0 & 2l_8 \\ l_4 & 0 & 0 & -l_7 - k_{\mathrm{HO_2},w} & 0 \\ 0 & 0 & 0 & l_7 & -l_8 - k_{\mathrm{H_2O_2},w}. \end{bmatrix}. \tag{65}$$

The Jacobian-based approach can be applied at temperatures high enough for reactions to occur, but it fails at the explosion limit when the wall reactions are included because the matrix $\mathbf{A}'$ becomes singular there,

$$\det(\mathbf{A}') = 0. \tag{66}$$

This condition is plotted in Fig. 13 as the dashed-dotted curve, with the selections $\varepsilon_k = \left[\varepsilon_{\mathrm{H}}, 0, 0, 5\times10^{-3}, 0\right]$ as expressed in the order of radical vector $\bar{C}$ (22). In plotting the results, we took the liberty of employing $\varepsilon_{\mathrm{H}} = 0.72\sqrt{D_{\mathrm{H}}\lambda}/\bar{c}$, consistently with the analysis of the previous section[2].

The resulting predictions are seen to be in excellent agreement with the experimental results, indicating that the values chosen for the sticking coefficients may be reasonable. In this description, the H-atom destruction at the walls ε_{H} controls the first limit, while the third explosion limit would be highly sensitive to HO_2 destruction through $\varepsilon_{\mathrm{HO_2}}$, instead.

2.1.3 The third explosion limit

The much-disputed [24, 25] upper part of the dashed curve in the figure is obtained from the parameter-free expression

$$a = \left(\frac{10.25 D_{\mathrm{H_2O_2}}\sqrt{\kappa T_o k_6}}{l_8 l_7 \sqrt{\beta Q}}\right)^{1/3}, \tag{67}$$

which is derived from a thermal-explosion analysis, with H_2O_2 being the dominant intermediary that diffuses to the walls where it is destroyed completely [16, 26].

The success of this model is comparable with that of Wang et al. [22] in describing the third limit, demonstrating that two very different physical processes can produce nearly identical predictions for this limit when suitable values are assigned to unknown parameters. For example, in the Jacobian approach (66), with the values of the sticking coefficients selected for the figure, H_2O_2 is not consumed at all at the walls, while in the diffusion approach it is consumed completely. On the other hand, HO_2 is assigned a constant sticking coefficient for the dot-dash curves (66) in the figure, while it is not consumed at the walls for the dotted curves (67) !

[2] The expression selected here for ε_{H} produces a value that increases appreciably as temperature increases along the limit curve, consistent with the expected increase in the destruction rate with increasing temperature, while it is assumed to be a constant in [22], leading to larger discrepancies for the first explosion limit.

Concerning the relationship with the first section, it may be observed that the Jacobian approach is equivalent to neglecting the runaway time (56) in comparison with the branching time, (28) $t_E \ll t_B$ while, for Eq. (67), $t_B \ll t_E$ is assumed. Upon investigating Figs. 5, 9, 10, and 13 (see also [17,27] for a discussion on the transition between the two regimes), one can infer that the Jacobian approach is valid close to the turning point (at which $\alpha \approx 1$), while the diffusion approach (67) is the correct one for higher pressures, where $\alpha \ll 1$. The strong sensitivity of predictions of the Jacobian formulation to the value of the HO_2 sticking coefficient for $\alpha \ll 1$ [23] is also a good indicator that the parameter-free expression (67) is the correct one there.

2.2 Premixed flames: flammability limits

This section addresses only the so-called flammability limits of H_2-air planar flames (deflagrations); the reader is referred to the Chapter on laminar flames for a full description of H_2 premixed-flame properties. It is simply recalled here that premixed-flame propagation involves a thermal diffusivity D_T to conduct heat upstream to regions where $T < T_c$, raising the temperature to $T > T_c$ so that oxidation can proceed at a rate characterized by a reciprocal time $\dot{\omega}$, leading to a deflagration velocity $S_L \propto \sqrt{D_T \dot{\omega}}$ [2,28].

In most applications, premixed combustion involves the propagation of quasi-isobaric waves called deflagrations or premixed flames. They often propagate in highly turbulent flows and are affected by the flow dynamics. In such scenarios, different combustion regimes are encountered, depending on competition between the turbulent flow and molecular transport with chemical reaction. Though multiple regimes exist, it is well accepted that most turbulent-flame properties can be related to the self-sustained planar-flame propagation velocities under laminar conditions, the so-called laminar burning velocity S_L. This value emerges as a fundamental measure of the reactivity of a premixed system for given initial conditions.

In developing detailed mechanisms [3–8], an enormous amount of effort has been invested in determining this fundamental property, both experimentally [29–40] and numerically [41, 42]. Figure 14 presents a large selection of experimental results for hydrogen-air flame velocities and compares those results with numerical predictions obtained using the complete mechanism of Tab. 1. Excellent overall agreement is evident between the different experimental data sets – obtained by different research groups – showing that one-dimensional planar flame propagation is now relatively well described, at least under normal ambient conditions. Although only one numerical prediction is shown, other detailed descriptions [4–8] of Fig. 2 produce similar agreement for these ambient conditions. On the other hand, rate-optimization of detailed descriptions for high pressures remains an active topic of investigation.

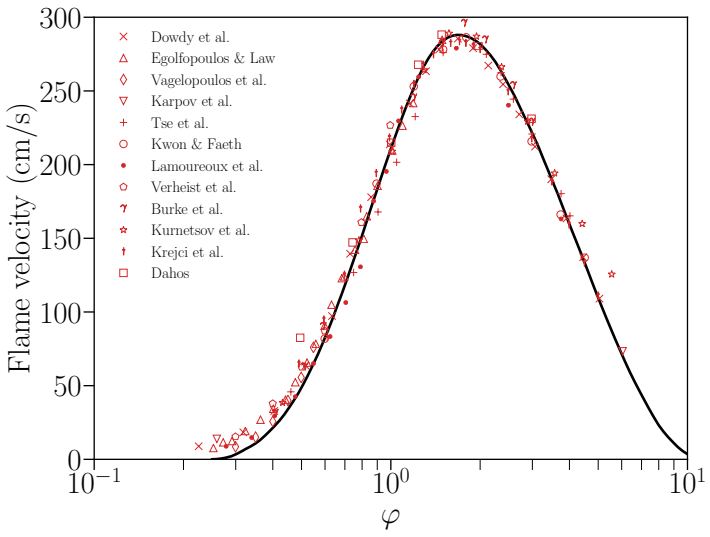

Fig. 14 laminar flame velocity of hydrogen-air mixtures at atmospheric conditions. Solid curve corresponds to calculations with the complete mechanism while symbols correspond to experiments as follows:

Symbol	×	△	◇	▽	+	○	•	⬠	γ	☆	†	□
Reference	[29]	[30]	[31]	[32]	[33]	[34]	[35]	[36]	[37]	[38]	[39]	[40]

* Data extracted from [20].

2.2.1 Planar premixed-flame propagation limit – flammability limits

At low concentrations of the limiting reactant (hydrogen for fuel-lean flames and oxygen for fuel-rich flames), the concentrations of the intermediate chemical species are small, and their production and destruction occur in a thin layer at the hot end of the flame. Under these conditions, only nine elementary reactions, described in [43], are needed to describe the flammability limit accurately.

1	$H + O_2 \rightleftharpoons OH + O$
2	$H_2 + O \rightleftharpoons OH + H$
3	$H_2 + OH \rightleftharpoons H_2O + H$
4	$H + O_2(+M) \longrightarrow HO_2(+M)$
5_b	$HO_2 + H \longrightarrow H_2 + O_2$
6’	$HO_2 + H \longrightarrow 2\,OH$
7’	$HO_2 + OH \longrightarrow H_2O + O_2$
8’	$H + OH + M \longrightarrow H_2O + M$
9’	$2H + M \longrightarrow H_2 + M$

The necessary rate parameters are given in standard format in [43], as extracted from the San Diego detailed mechanism [3]. The first 5 of these reactions correspond to those of the skeletal mechanism for autoignition conditions, and the first 4 alone suffice to describe the fuel-lean limit. This numbering is employed only in the

present section (Eqs. 68 through 70), with primes identifying steps having numbering different from that elsewhere in this chapter.

The OH and H radicals are found to satisfy the quasi-steady-state assumption, so that a single global reaction $2H_2 + O_2 \rightarrow 2H_2O$ suffices to describe the flame structure. The associated global reaction rate is obtained from the elementary reaction rates according to

$$\omega = \omega_{4f} + \omega_{8'f} + \omega_{9'f} = k_{4f} C_{M_4} C_{O_2} C_H + k_{8'f} C_{M'_8} C_{OH} C_H + k_{9'f} C_{M_{9'}} C_H^2. \quad (68)$$

From the OH steady-state approximation, the reaction rate may be simplified, near the lean limit, as

$$\omega = \left(\frac{\alpha}{2} - 1\right) \frac{k_{2f} k_{3f} / k_{1b}}{1 + \frac{k_{3b} C_{H_2O}}{k_{4f} C_{M_4} C_{O_2}}} C_{H_2}^2. \quad (69)$$

For deflagration propagation to be possible, ω has to be positive somewhere in the flame - within which the temperature vary from its fresh-mixture value to the adiabatic flame temperature T_a. Since α increases with temperature, this condition is equivalent to $T_a > T_p$, where T_p is the temperature at which ω is zero. At the lean limit (69), T_p therefore corresponds to the condition $\alpha = 2$, yielding a temperature somewhat higher than the induction crossover temperature T_c (corresponding to $\alpha = 1$).

In a similar manner a simplified equation for the rich limit can be derived as

$$\omega = \left(\frac{\alpha}{2} - 1 + \frac{k_{6'f} / (k_{6'f} + k_{5b})}{1 + \frac{k_{7'f}}{k_{6'f} + k_{5b}} \frac{k_{3b} C_{H_2}}{k_{3f} C_{H_2O}}} \right) \frac{(k_{4f} C_{M_4})^2}{\frac{k_{3b} C_{H_2O}}{k_{3f} C_{H_2}} k_{8'f} C_{M_8} + k_{9'f} C_{M_{9'}}} C_{O_2}^2, \quad (70)$$

yielding a slightly different condition for T_p, valid at the rich limit. A more complex formula for T_p, applicable for both the lean and rich limits, is also available [43].

Figure 15 compares the laminar burning velocity predicted by the 1-step mechanism according to the global rate in the corresponding limit (Eq. 69 or 70) with that of the complete mechanism. There is excellent agreement at both limits. Agreements improve with increasing pressure, extending over wider ranges of equivalence ratios (not shown here). The T_p and T_a curves may be seen in the figure to cross at zero burning velocity, corresponding to the lean and rich flammability limits.

Near the rich limit pulsating instabilities arise in one-dimensional, planar propagation [44–46] as a consequence of the high Lewis number of O_2 in these flames, resulting in oscillations of the peak values of the temperature and H-radical concentration profiles [47,48]. The transition between steady and unsteady propagation regimes is linked to a Hopf bifurcation [49,50]. For the pulsating regime, the one-step, steady description described above fails, and at least two global steps are required. Taking this phenomenon into account has the effect of narrowing the flammability range around the rich limit [47,48].

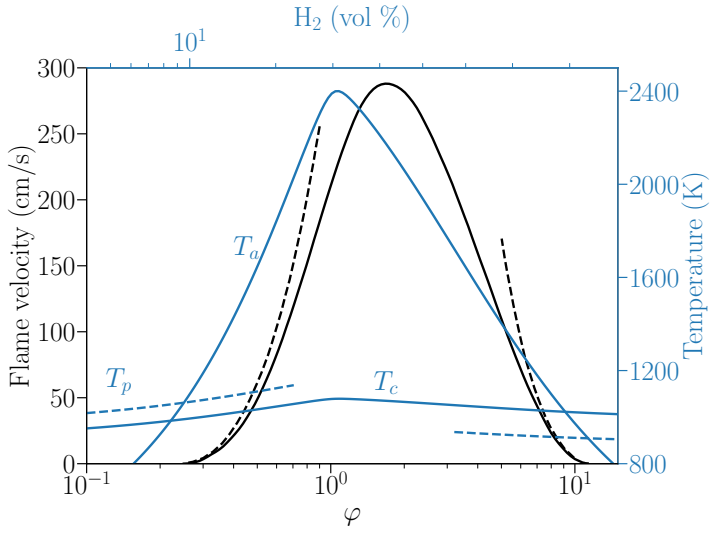

Fig. 15 Laminar burning velocity and the adiabatic flame temperature, T_a of hydrogen-air mixtures at normal atmospheric conditions as functions of the equivalence ratio. Also shown are the premixed flame crossover temperature, T_p, and the classical crossover temperature, T_c. The solid curve corresponds to the complete mechanism [3] while the dashed segments represent predictions of the single-step mechanism [43].

2.2.2 Multi-dimensional effects and potential unexpected propagation in narrow channels.

Departures from the one-dimensional configuration discussed above are prevalent for hydrogen flames. Planar-deflagration instabilities are associated intimately with the relation between the molecular transport process and the finite rate of heat release. The well-known Darrieus-Landau instability, which results from the density change across to a perturbed flame front, tends to destabilize the flame front [51–53], but the effect may be offset by diffusive-thermal phenomena. In the specific case of hydrogen flames, this typically occurs only over an intermediate range of equivalence ratios, and the flames are intrinsically unstable for rich and lean mixtures.

Near the lean propagation limit, cellular finger-like structures arise and propagate into the fresh mixture [54–58]. In addition, heat-loss effects become important when walls are present, and they can drastically modify flame propagation. Veiga-López et al. [59] studied the effects of heat losses on hydrogen flame propagation in a quasi-two-dimensional Hele-Shaw combustion chamber, controlling the heat-loss rate by modifying the gap distance between the two plates. Figure 16 shows the water trace that the H_2-air flame leaves behind after the combustion process, as revealed by a Schlieren technique. Under low-to-moderate heat losses, case (a) in Fig. 16, a continuous flame front characterizes the propagation, but, when the heat losses become important, the flame front breaks into several small flame cells that propagate into the fresh gases, continuously generating secondary smaller cells in a

fractal-like pattern, Fig. 16(b). The last mode found in this investigation, with high heat losses that are nearly enough to completely prevent propagation, involves the propagation of isolated flame cells moving almost straight, as is seen Fig. 16(c). Thorough explanations of these observations are yet to be completed.

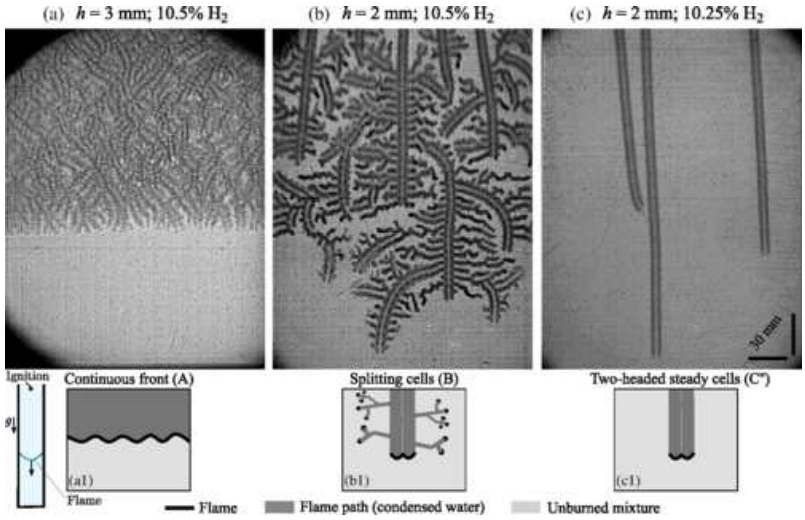

Fig. 16 Downward propagating H_2-air flames in a Hele-Shaw cell, near the lean flammability limit [59]. Reprinted figure with permission from F. Veiga-López, M. Kuznetsov, D. Martínez-Ruiz, E. Fernández-Tarrazo, J. Grune, and M. Sánchez Sanz, Physical Review Letters, vol. 124, p. 174501, 2020. Copyright (2020) by the American Physical Society.

The two unexpected propagation modes are related to the intense heat-loss contribution that tends to prevent flame propagation, along with the high hydrogen diffusivity, which can compensate for the heat losses by bringing surrounding hydrogen into the reaction zone of the flame and thereby providing higher hydrogen content there to release more heat. These two unexpected propagation modes extend the flammability limits of H_2-air flames beyond the planar, adiabatic flammability limits; Figs. 15 and 16 (a), exhibit a minimum H_2 concentration $\sim$ 9.5%, while the authors of [59] report propagations for H_2 concentration as low as $\sim$ 4.5%. This result is particularly important for safety studies as it implies that H_2 flames may propagate in gaps much narrower than initially anticipated.

A three-dimensional configuration in which hydrogen burns under suitable conditions is that of flame balls. Flame balls were first predicted in theoretical work by Zel'dovich [60], who reasoned that they would be unstable and therefore not observable in the laboratory, but later they were found experimentally by Ronney under microgravity conditions [61–64]. They consist of a spherical reaction layer bounding a hot core of reaction products, heat and products diffusing to the surrounding region while the fresh gases supply the reactants by diffusing into the reaction layer from the surroundings. Radiation heat losses that were not considered in the original

analysis stabilize the structure, enabling it to survive so long as buoyancy or other perturbations do not move it to walls that quench it [65].

2.2.3 Conservative deflagration limits for hydrogen safety

In addressing hydrogen safety issues, it may be convenient to retain a single value for hydrogen flammability limits, instead of a value for each specific flow configuration. The values commonly found in hydrogen safety reports are listed in Tab. 5, with the lean limit being most important for safety considerations.

Table 5 Hydrogen deflagration limits in Oxygen and Air [66, 67], expressed in H_2 vol. %.

	Lower	Upper
Flammability limit O_2	4.0	95.0
Flammability limit Air	4.0	75.0

The notable difference between the lean flammability limits seen in Fig. 15, corresponding to a H_2 volume content of $\sim$ 9.8% rather than 4%, is due to (i) multi-dimensional effects and (ii) gravity effects. The 1D study (Fig. 15) neglects influences of wrinkling and curvature which effectively extend the limit as shown, e.g., in the example of Fig. 16. The lean limit is also strongly dependent on the direction of propagation of the flame relative to that of gravity. In [66], a value of 4% is reported for upward propagation, which favors the development of curvature through the influence of buoyancy, whereas the limits for horizontal and downward propagation are close to 7% and 9%, respectively. With these considerations in mind, 4% seems to be a safe, conservative estimate for the lean flammability limit for hydrogen mixtures.

2.3 Detonation propagation limits

As in the deflagrations studied above, ideal detonations are also planar fronts, but their physics of propagation relies on adiabatic shock compression and subsequent autoignition. A strong coupling between the leading shock and the reaction zone is a key feature of self-sustained detonations. Its characteristic propagation velocity is on the order of $\mathrm{km\,s^{-1}}$, whereas H_2 propagation velocities of deflagrations do not exceed a few $\mathrm{m\,s^{-1}}$. The usually observed detonation propagation speed is called the Chapman-Jouguet velocity, D_{CJ}, a minimum in that strong detonations propagate faster but weaken over time through wave interactions. In the presence of losses (i.e. curvature, friction, interaction with inert layers, etc.) detonations have been observed to propagate at speeds below D_{CJ}. If these losses are strong enough to decouple the leading shock from the reaction zone, extinction occurs.

Indirect initiation of detonations can occur through deflagration-to-detonation transition (DDT), which involves the initial ignition of a flame, its subsequent acceleration, the formation of shocks ahead of it, and often interactions with obstacles [68], leading to flame-shock complexes that result in detonation onset usually with localized explosions arising downstream from the precursor shock, typically in boundary layers near walls or near the flame front [69,70]. One of the first detailed observations of DDT was documented by Oppenheim et al. [71]; recent numerical simulations have helped to clarify the phenomenology of DDT [72–74], although the processes involved are so complex that much more remains to be learned about them.

Gaseous detonations exhibit a characteristic cellular structure, which effectively involves the motion and collisions of transverse waves passing along the wave front forming triple points (see Fig. 17). Traditionally, detonation cells have been charac-

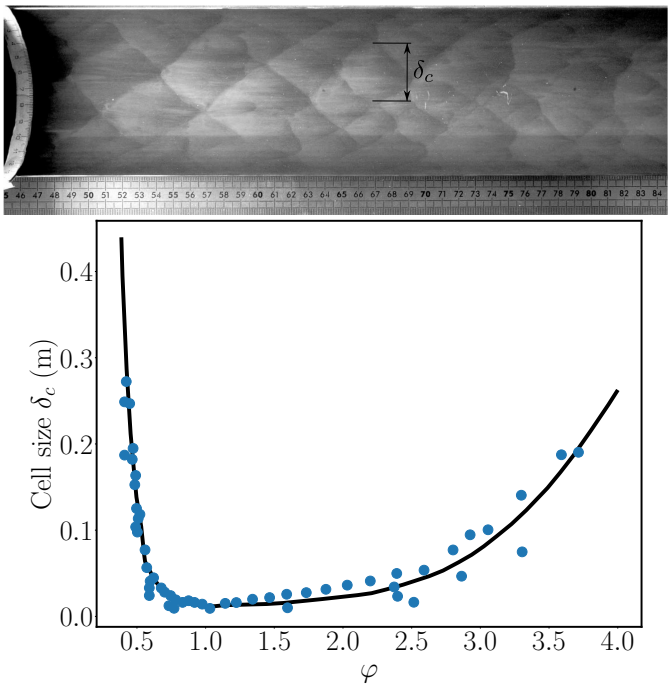

Fig. 17 Top : Experimental soot foil marking the trajectory of triple points obtained in a tube of 57 mm in diameter for a hydrogen-air mixture with propane addition at normal ambient pressure and temperature (p_0 = 100 kPa and T_0 = 300 K). Image adapted from [75]. Bottom : average detonation cell size as a function of equivalence ratio for H_2-air. Experimental data (symbols); curve fit (solid line).

terized as having either a *regular* or an *irregular* structure. Regular detonation cells have very structured patterns with cell sizes that can be unambiguously determined. Irregular detonation cells on the other hand, exhibit stochastic-looking structures

where various length scales are present [76, 77]. The characteristic cell size δ_c[3] is directly correlated with the reactivity of the mixture, smaller δ_c values being associated with faster reaction rates. As a result, δ_c increases drastically for mixture compositions away from stoichiometry or with high dilution levels [78] (see Fig. 17).

Detonation propagation limits for uniform mixtures are typically given as a function of a characteristic length, ℓ, dictated by the configuration considered, scaled by the detonation cell size, δ_c. Qualitatively, for confined tubes and channels the critical conditions are $\ell \geq \delta_c/\pi$ and $\ell \geq \delta_c$, respectively. Experimentally, for detonation transmission from tubes/channels to open-space (see Figures 18), ℓ is $13\delta_c$ and

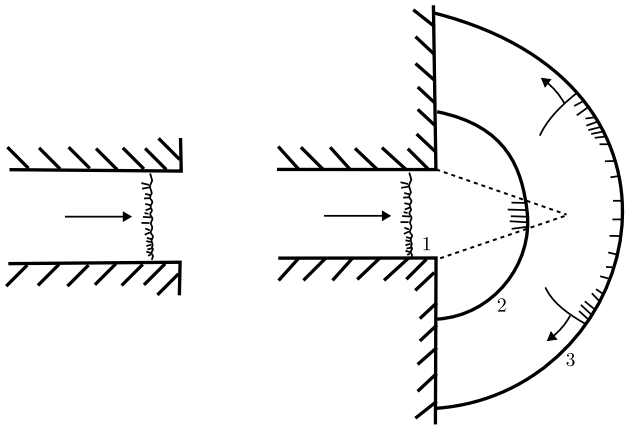

Fig. 18 Schematic representation of detonation transmission from a tube to an open area. Left : detonation front propagation in a tube. Right : detonation front diffraction 1 and re-ignition 2-3 process.

$11\delta_c$ for most hydrocarbons, and reduces to $\ell = 3\delta_c$ for high-aspect-ratio channels; the latter critical value was also found for detonation propagation in stoichiometric hydrogen-oxygen mixtures confined by an inert layer [79], but for hydrocarbons, this value increases to $\ell \sim (5-10)\delta_c$ [80]. These experimental results suggest that, depending on the boundary conditions that the wave is exposed to (i.e., confining walls or inert gases), the extinction limits vary; triple points play a fundamental role in detonation propagation and conditions in which their reflections are totally or partially suppressed render the wave more prone to failure.

The prediction of limiting behaviors for detonations is a challenge even with the use of state-of-the-art numerical simulations, likely because of the very simplified descriptions of the chemistry that have to be used, as discussed in [81] or the assumption of inviscid/non-conducting flow that typically is made, as argued in [82]. Experimental data bases [78] therefore continue to be the most reliable source when limits are needed for design and sizing of facilities, be it to avoid detonation

[3] Most authors use λ for the cell size, which in this chapter denotes the mixture's reactivity.

initiation in industrial settings [83] or promote detonation propagation in propulsion applications (such as in rotating detonation engines [84, 85]).

In spite of the challenges mentioned above, simple models exist in which sink terms are added, to account for heat and momentum losses or curvature, to the Zel'dovich-von Neumann-Döring (ZND) model (a 1-D laminar, steady description of a detonation wave) from which one can obtain the so-called $D - c_f$ [86] and $D - \kappa$ [87] curves. Turning points on these curves yield the maximum friction/heat losses or curvature that a one-dimensional detonation is able to sustain, thereby providing a conservative propagation limit. In the specific case of H_2 detonations, even simpler models can be devised in which the thermodynamic state behind the leading shock (i.e., von Neumann state) is simply compared with the crossover temperature, T_c, as proposed by Belles [88, 89]. A selection of these models will be discussed briefly next.

2.3.1 Propagation limits of planar detonations - Belles' Model

Ideal detonability limits may be understood in a way very similar to the deflagration-limit considerations presented in the previous section, namely evaluating a crossover variable (or temperature T_c) in the induction zone. According to Belles [88, 89], self-sustained detonation exist for $\alpha > 1$ in the post-shock region, also referred to as the von Neumann (vN) state.

In Belles' model [88] the critical Mach number Ma_c is computed using the Rankine-Hugoniot jump relations and the condition that $\alpha = 1$ at the vN state. Since the post-shock temperature increases with increasing Mach number, self-sustained detonations are possible only if the detonation Mach number $Ma_D = D_{\mathrm{CJ}}/c_0$ is greater than Ma_c (i.e., $Ma_D > Ma_c$), where c_0 is the sound speed in the fresh mixture [90]. The latter statement is equivalent to saying that the post-shock temperature at the vN state, T_{vN}, exceeds T_c at the post-shock pressure, p_{vN} .

Figure 19 shows the post-shock temperature, T_{vN}, computed using detonation software [91], and the crossover temperature T_c evaluated at the post-shock pressure, p_{vN}, as a function of equivalence ratio for $H_2 - O_2$ and H_2-Air mixtures. Since detonability limits are often reported in percent by volume, $\%H_{2,\,\mathrm{vol}}$ corresponding axes are also included in Fig. 19. The predicted lean limits are $\%H_{2,\,\mathrm{vol}} = 17.8$ and $\%H_{2,\,\mathrm{vol}} = 19.5$ for $H_2 - O_2$ and H_2-air, respectively, in agreement with experimental data [92]. Similar observations can be made for rich limits, $H_2 - O_2$ exhibits wider limits ($\%H_{2,\,\mathrm{vol}} = 90$) than H_2-air ($\%H_{2,\,\mathrm{vol}} = 58$).

2.3.2 Propagation limits in tubes - Fay's model

As mentioned above, experimental detonability limits are dependent on the initial mixture conditions as well as on the nature of the boundary [93]. Two main categories are yielding confinement [81, 94, 95] and rigid confinement [96, 97]. For a given mixture composition φ and thermodynamic state there is a tube diameter below

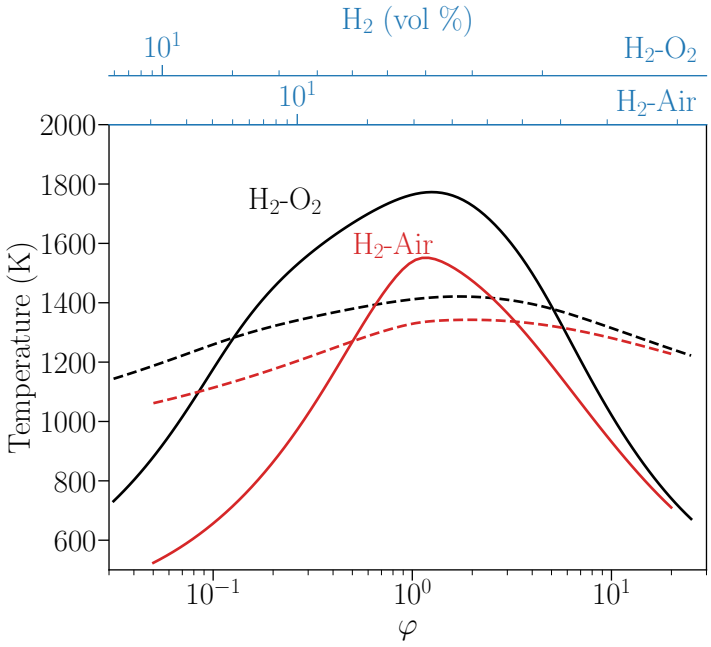

Fig. 19 Detonation post-shock temperature (solid curves) and the crossover temperature at the Neumann state (dashed curves) as a function of equivalence ratio for H_2-O_2 (black) and H_2-air (red) mixtures. Conditions: $p_0 = 1$ atm, $T_0 = 300$ K) prevail in the fresh mixture. The ideal detonability limits correspond to the intersection of the solid lines with the dashed lines.

which a steady detonation can no longer be sustained. Figure 20 shows the limit equivalence ratio as a function of the inverse of the tube diameter. Narrowing of the limits with decreasing diameter is evident, and it may be inferred by extrapolation that there is a diameter small enough that propagation can be prevented for all equivalence ratios.

As the tube diameter decreases, boundary-layer effects becomes prominent, and a detonation velocity deficit is observed. The losses are due to friction and heat transfer to tube walls, causing front curvature and flow divergence at the boundaries. Moreover, the detonation velocity changes affect the post-shock and final-state conditions, thereby altering detonability limits. Fay [99] proposed a model based on the negative displacement thickness of the wall boundary layer. An expression for the velocity deficit can be derived from the conservation equations of quasi-one-dimensional flow :

$$\Delta D_m = \frac{\Delta D}{D_{CJ}} = \frac{D_{CJ} - D}{D_{CJ}} = 1 - \left[\frac{(1-\nu^2)}{(1-\nu)^2 + \gamma(2\nu - \nu^2)} \right]^{1/2}, \qquad (71)$$

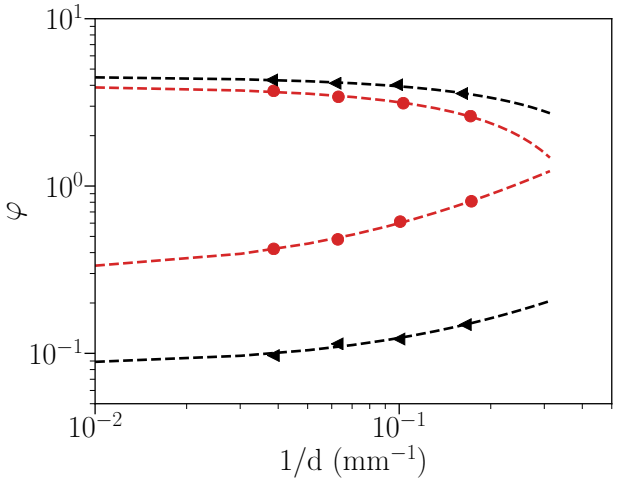

Fig. 20 Equivalence ratio as a function of inverse of tube diameter, adapted from [98]. Circles represent experimental results for H_2-Air mixtures while triangles are for H_2-O_2 mixtures.

where $\nu = \xi/|(1+\gamma)(1+\xi)|$, ξ is the stream-tube area-divergence factor, and γ is the ratio of specific heats. The area divergence is estimated from the boundary-layer displacement thickness δ^* :

$$\xi = \frac{A_1}{A_0} - 1 = \frac{\pi(d/2+\delta^*)^2}{\pi(d/2)^2} - 1 \approx \frac{4\delta^*}{d}, \text{with} \quad \delta^* = 0.22x^{0.8}\left(\frac{\mu_e}{\rho_0 D_{CJ}}\right), \tag{72}$$

where μ_e, x, and ρ_0 are the burnt-gas viscosity, the distance from the shock, and the initial gas density, respectively.

Fay's model [99] is compared with experimental results from Gao et al. [100] in Fig. 21. Three tube diameters $d = (1.8,\ 4.6,\ 10.9)$ mm are selected, and the initial pressure is varied to seek the maximum velocity deficit for which propagation was achieved. As the initial pressure decreases, the characteristic length scales of the detonation (δ_c) increase towards the tube diameter, and the effects of lateral losses become increasingly important, enhancing the velocity deficit, until the leading shock decouples from the reaction zone and quenching occurs. These results show that the theoretical model predicts correct trends but fails to predict the experimental velocity deficit accurately, implying that the process of detonation extinction is more complex and involves elements beyond the assumptions made for the derivation of this model.

An earlier study by Wood and Kirkwood [101] also takes into account the 2-D detonation curvature, but, as shown by Reynaud et al. [95,102], who compared results of numerical simulations with the model's predictions for detonation propagation under yielding confinement, it, too, is limited in its ability to recover the detonability limits of real mixtures. These observations attest to the complexity of the physical

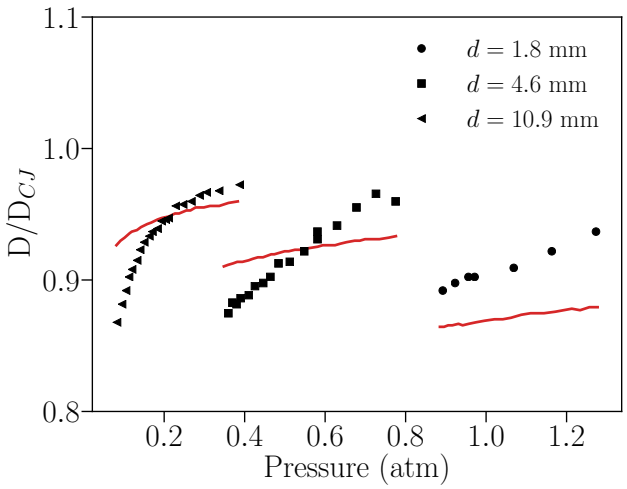

Fig. 21 Velocity deficit D/D_{CJ} as a function of the initial pressure for three different tube diameters. Comparison of Fay's [99] model (solid lines) for $H_2 - O_2$ mixture with experimental results from [100] (symbols).

processes involved in multidimensional configurations. To obtain more complete descriptions of the detonability limits of hydrogen for practical applications, it seems to be important to take into account additional characteristic scales, beyond the chemical scales, the size of the cellular structure δ_c, and the front curvature, by further addressing other transverse and longitudinal scales, such as the distance from the shock to the sonic plane (i.e., the hydrodynamic thickness) along with other geometrical aspects [103].

2.3.3 Conservative detonability limits for hydrogen safety

Just as was addressed for flammability limits in Sec. 2.2.3, it is convenient to retain single values for detonability limits. The values most widely found in the literature are reported in Tab. 6. Detonability limits are narrower than flammability limits

Table 6 Hydrogen detonability limits for confined explosion in Oxygen and Air [104, 105], expressed in H_2 vol. %.

	Lower	Upper
Detonation limit O_2	15.0	90.0
Detonation limit Air	18.3	58.9

(Tab. 5), but agree very well with Belles' simple 1D model (Fig. 19). It should not be concluded that detonability limits are not sensitive to curvature and geometrical effects, contrary to flammability limits, but rather that these effects tend to narrow the

H_2 detonability range, instead of expanding the range, as they do for deflagrations. The value of 18% may thus be retained as a conservative lean detonability-limit estimate for H_2-air mixtures.

2.4 Diffusion flames: ignition in mixing layer

Let us now consider ignition in a spatially evolving mixing layer [106]. The two-dimensional problem is sketched in Fig. 22. Two streams of identical density and velocity (one of fuel - with subscript F - the other of oxidizer - subscript O) come into contact at the end of a splitter plate. A spatially evolving mixing layer develops, eventually igniting farther downstream. Albeit complex mathematically, the solution is elegantly simple, being equivalent to that for the one-dimensional, time-dependent problem in which uniform half-spaces of fuel and oxidizer are brought together instantaneously at time zero [106].

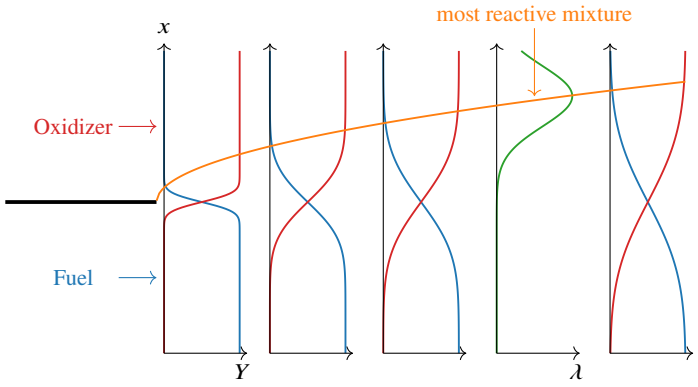

Fig. 22 Sketch of ignition in an unstrained mixing layer.

With the assumption of equal and constant density and velocity U_0 throughout the domain[4], the system reduces to

$$\begin{cases} U_0 \dfrac{\partial Y_k}{\partial y} + D_k \dfrac{\partial^2 Y_k}{\partial x^2} = \dot{\omega}_k \\ U_0 \dfrac{\partial T}{\partial y} + D_T \dfrac{\partial^2 T}{\partial x^2} = \dot{\omega}_T \,, \end{cases} \tag{73}$$

where

[4] This assumption may be relaxed using a more complex asymptotic description of the mixing layer [107].

$$\dot{\omega}_T = \frac{Q\omega}{\rho c_p} \tag{74}$$

and D_k and D_T are the diffusion coefficient of species k and the thermal diffusivity, respectively. The reciprocal-time source terms in these equations are the rate of production of mass of species k per unit volume divided by the density of the mixture and the rate of heat release per unit volume divided by the product of the density and the specific heat at constant pressure. Assuming unity for all Lewis numbers, the system (73) reduces to a single-equation problem

$$U_0 \frac{\partial Y}{\partial y} - \frac{U_0}{y}\left[\frac{\eta}{2}\frac{\partial Y}{\partial \eta} + \frac{\partial^2 Y}{\partial \eta^2}\right] = \dot{\omega}, \tag{75}$$

where

$$\eta = x\sqrt{\frac{U_0}{Dy}}$$

is the self-similar variable of classical diffusion problems [107]. The frozen-flow (flow without a source term $\dot{\omega}$) diffusion admits a self-similar solution of the form

$$Y_F = 1 - Y_O = \frac{1}{2}\mathrm{erfc}\left(\frac{\eta}{2}\right). \tag{76}$$

Through asymptotic analysis, Sánchez et al [106] proved that the mixture would ignite first where the branching characteristic time λ^{-1} is shortest, a result that will be useful in Sec. 4.3.2 of this chapter. A second result is that the ignition delay corresponds to that of the most reactive mixture in the mixing layer. To determine ignition lift-off distance in a mixing layer, one must then take the following steps:

- calculate the frozen self-similar solution through (76), or through a more complete description [107].
- identify the point in the mixing layer where λ (42) is maximum,
- compute the ignition delay, t_B, for these conditions by (45) and multiply by the flow velocity U_0 to obtain the ignition distance (lift-off).

Although it was initially restricted to the high-temperature regime, the study [106] quite likely can be extended to conditions below crossover by simply replacing t_B by $t_B + t_E$. Analytical studies are also available for strained mixing layers [20, 108], a configuration of high relevance to practical non-premixed flows (e.g. in turbulent jets).

2.5 Thermal ignition

Heated surfaces represent a potential hazard that needs to be assessed in order to prevent and mitigate accidental combustion events. One of the potential hazards that must be considered as part of certification is the ignition of flammable fluids

(aviation kerosene, engine oil, hydraulic fluids) by hot surfaces which may be present in the design (engines, hot air ducts) and can also develop through events such as lightning strikes, rotor bursts or electrical-system failures. Currently, the analysis of hot-surface ignition relies extensively on legacy guidelines that are based on empirical test methods that often have little relationship to the actual hazards. A goal for the future is the development of more applicable tests and analysis methods based on numerical simulation of thermal ignition.

2.5.1 Hot-surface ignition scenarios

Several cases can be differentiated based on two important parameters: (i) whether the surface is stationary or moving with respect to the reactive gas, and (ii) the characteristic length scale, L, of the hot surface (see Figure 23). Previous work has shown that, in the case of stationary hot surfaces, two ignition regimes exist: low temperature (LT) and high temperature (HT) ignition. The former regime is mostly relevant to large surfaces and hydrocarbon fuels such as *n*-alkanes which may still auto-ignite at temperatures on the order of 500 K [109–111]. The latter regime applies to smaller surfaces and more reactive fuels like H_2 because the LT and HT ignition time scales for this fuel differ significantly (see, e.g. Fig. 2).

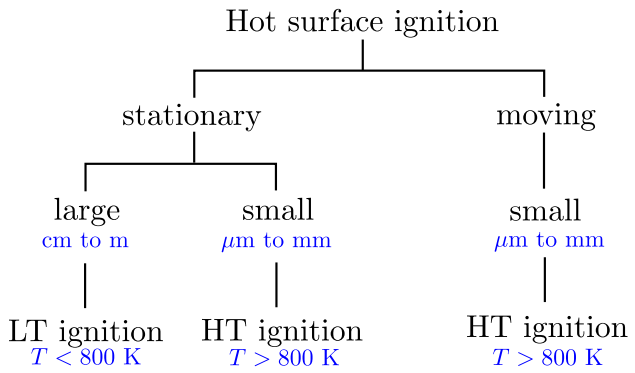

Fig. 23 Hot surface ignition scenarios.

Studies using commercial glow plugs [112, 113] and "inert" laser-heated particles suspended in explosive atmospheres [114] show that the minimum ignition temperature is weakly dependent on the equivalence ratio but highly dependent on the type of fuel used (e.g. *n*-pentane, propane, ethylene or hydrogen). The minimum ignition temperature is also highly dependent on the hot-surface length scale (i.e. glow plug height or particle/vessel diameter). Effects of the surface material (silicon nitride, tungsten carbide, steel, casting steel, and aluminum) at fixed composition for sub-millimeter sized surfaces have been observed with H_2 [115]. Aluminum and steel (type 1.4034 and 1.3541) exhibit the lowest and highest ignition thresholds,

respectively. The mixture chemical properties and surface properties (e.g. geometry, material) are thus important to determine the minimum surface temperature required to ignite a reactive gas.

Another parameter found to play a major role in hot-surface ignition is the rate at which the surface is heated. In the LT regime, the heating rate imposed on a stationary large hot surface determines the type of reaction that the reactive mixture experiences, namely slow oxidation or rapid explosion [116, 117]. For a small stationary hot surface [112, 118], the chemical processes of HT chemistry typically dominate irrespective of the fuel considered, although the negative temperature coefficient (NTC) region characteristic of LT chemistry of higher normal alkanes can influence the ignition behavior for hydrocarbons like *n*-hexane, while being absent and hence irrelevant for hydrogen.

For moving small surfaces ($2-5$ m/s), similar to their stationary counterparts, HT chemistry dominates. For a fixed gas mixture, previous work suggests that the size and temperature of a particle are the most important factors in determining whether ignition occurs [119]. In the specific case of H_2-O_2-N_2 mixtures, differential diffusion (i.e., species diffusion at different rates) has also been found to have an effect on ignition thresholds [120, 121]. Experiments provide invaluable data for validation of numerical simulations to determine the level of refinement required for the modeling of key physical processes so that accurate predictions using approximate reaction mechanisms can be made.

2.5.2 The physics of thermal ignition

The interaction of the surface with the flow is key in creating zones that are prone to ignition. This is illustrated in Fig. 24 for a small ($L = h = 9.4$ mm) surface in natural convection, as well as for a small ($L = d = 4$ mm) moving surface in forced convection.

In the separated-flow region, species and energy convection is often negligible, and the build-up of intermediate species is opposed only by diffusion, facilitating the branching and thermal runaway characteristic of ignition processes. Close to the wall, diffusion counteracts the heat release due to chemistry. At some distance away from the surface, the heat-release rate is greater than the rate at which heat is diffused back to the wall, giving birth to an ignition kernel. In H_2 systems this is observed to occur when the gas temperature exceeds the crossover temperature T_c. Notably, irrespective of the ignition time and length scale, the location where ignition takes place seems to be a universal feature of both natural and forced convection in internal [117] and external flows (see Fig. 24).

Detailed transient multidimensional simulations are typically needed for an accurate prediction of ignition thresholds. This is because important features in the flow field such as boundary-layer separation and processes of energy/species transport play a significant role in flows where ignition takes place within the thermal/hydrodynamic boundary layer next to a hot surface.

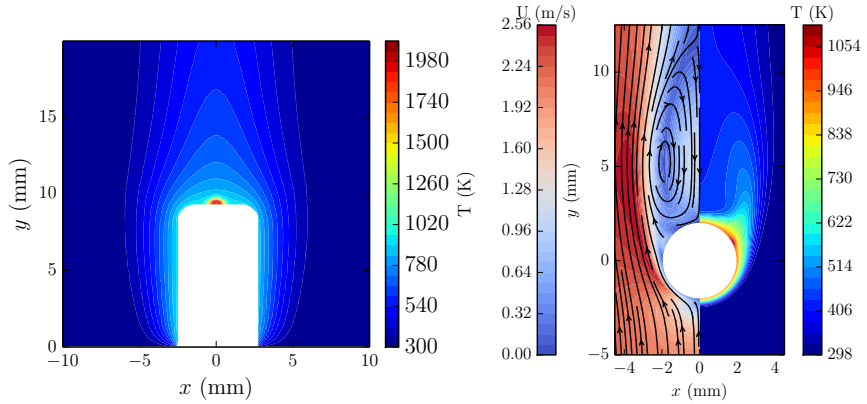

Fig. 24 Ignition-kernel formation for hot surfaces in natural (left) and forced (right) convection. Left: stationary small surface (glow plug). Right: moving small surface (falling heated sphere).

As in previous sections, simpler approaches also exist to determine order-of-magnitude estimates for hot-surface ignition. These rely on deriving a new set of equations from the conservation laws, in which only leading-order terms are retained, based on the main physics involved (e.g. convection, diffusion, mixing, etc.). The ignition theories of Semenov [122] and Frank-Kamenetskii [123] are good seminal examples already covered in Sec. 2.1. A more recent analytical approach is provided next.

Consider a one-dimensional thermal-ignition problem of characteristic size δ. An isothermal wall is placed at the origin, $T(x=0)=T_w$, while the other end correspond to the free-flow temperature $T(x=\delta)=T_\delta$. Neglecting reactant consumption (A1), and retaining heat diffusion and heat release only leads to a single governing equation

$$Q\omega = \kappa \frac{\mathrm{d}^2 T}{\mathrm{d}x^2}, \qquad T(x=0)=T_w, \qquad T(x=\delta)=T_\delta, \tag{77}$$

with a global reaction rate

$$\omega = \left(\frac{\rho}{W}\right)^n X_F^{m_\mathrm{F}} X_O^{m_\mathrm{O}} A e^{-\frac{E_a}{RT}}, \tag{78}$$

where $n = m_\mathrm{F} + m_\mathrm{O}$ is the reaction order. In the expression for ω (78), the density further is assumed to be constant and equal to the mean geometrical density between both extremities $\sqrt{\rho_\delta \rho_w}$. Laurendeau et al. [124] showed that integration of (77, 78) yields an expression for the heat flux q_chem from the reacting mixture to the wall

$$q_\mathrm{chem} = \kappa \left(\frac{\mathrm{d}T}{\mathrm{d}x}\right)_w = \sqrt{2\kappa Q \omega_w \left(\frac{T_\delta}{T_w}\right)^{n/2} \frac{R {T_w}^2}{E_a}}, \tag{79}$$

where ω_w is the kinetic source term (78) at the wall.

An approximate ignition criterion may finally be obtained as the condition for which the heat flux generated by the chemistry, q_{chem}, equals the heat flux at the wall

$$q_{\text{loss}} = \frac{\kappa Nu}{L}(T_w - T_\delta). \tag{80}$$

The advantage of this formulation is that it is possible to use classical empirical Nusselt-number (Nu) correlations [125] to best match the nature of the flow at hand (e.g. natural/forced convection, stagnant flow, etc.).

If Nu is constant, a proportionality relationship between the wall temperature and the length scale of the hot surface can be derived [124]

$$\ln L \propto \frac{E_a}{2RT_w} \tag{81}$$

The wall temperature T_w scales with the natural log of the length scale L. See [126] for a complete derivation of the model, and a discussion on the limitations of this type of scalings.

2.6 Shock-induced ignition

While hot-surface ignition is the most likely means of igniting a flame in accidental scenarios, it is also possible to initiate chemical reactions in the absence of diffusive processes. Shock waves (flow discontinuities across which pressure and temperature increase abruptly) can be generated in controlled laboratory settings using shock tubes or may result from leaks in high-pressure vessels typically used for fuel storage in industrial facilities.

We have seen in the previous section that hydrogen ignition can easily take place through diffusive processes at relatively long time scales ($\sim$ 1 s) and initiate fronts that propagate by heat and mass transfer. At shorter time scales ($\sim$ 1 ms / μs), reactive mixtures can be ignited by shocks or adiabatic compression with diffusive processes playing a minor role. The simplest experimental device that is used to study chemical kinetics is a shock tube whose $x - t$ diagram is sketched in Fig. 25. The thermodynamic states in a constant-cross-section shock tube, composed of a high-pressure driver (state P_4) and a low-pressure driven section (state P_1), can be predicted reasonably well with 1D gas dynamics, and the *shock tube problem* is typically covered in elementary gas dynamics books [127, 128].

In simplest form, processes in a shock tube are assumed to be adiabatic and inviscid, so heat release through chemistry becomes the only possible mechanism responsible for modifying the post-shock state. High-temperature chemical-kinetic investigations generally are made in the region behind the shock reflected from the end wall (referred to as P_5 and T_5 by chemical-kinetics researchers) [129]. Shock tubes have played a fundamental role in combustion science, particularly in clarifying high-temperature kinetics, and they have enabled measurements of

ignition delay times, τ_{ign}, as well as of the rates of progress of elementary reactions. This is because the thermodynamic state 5 is, for all practical purposes, constant and highly repeatable; formulas for the strength of the incident shock, M, as a function of the pressure ratio P_4/P_1, as well as for P_5 and T_5, are given in textbooks.

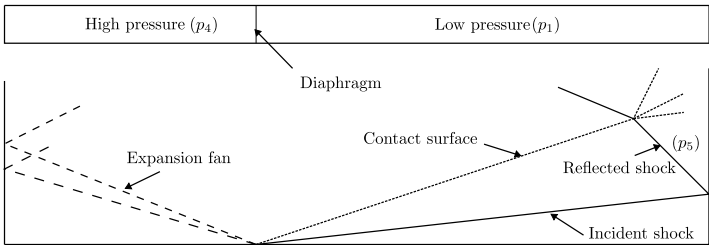

Fig. 25 Sketch of shock tube and wave diagram. Shock waves are represented by solid lines. Reflection from the right wall produces an interaction of the shock with the contact surface that separates the shocked gas from the driver gas. The expansion fan propagates towards the left wall reducing the pressure in the high pressure gas.

Depending on the strength of the reflected shock wave, two distinct ignition modes have been identified in $H_2 - O_2$ mixtures [130]: (i) strong and (ii) weak ignition. Strong ignition takes place for post-shock temperatures well above the crossover temperature ($T_5 > T_c$) and for which ignition of the mixture is assumed to take place homogeneously after the induction time t_i.

For $T_5 \lesssim T_c$, weak ignition occurs and is characterized by spatial nonuniformities in which perturbations of the flow field and diffusive processes play a role, resulting in localized temperature increase. Since the ignition delay time, t_i, is more sensitive to temperature variations in weak ignition (see, e.g. Fig. 2), the ignition process occurs in a non-uniform manner and may result in the initiation and propagation of reaction fronts (deflagrations). Figure 26 shows results from the literature in which the *extended* second limit is defined as $\alpha = 1$, denoting the strong/weak ignition boundary for H_2 mixtures, with strong ignitions identified by solid symbols and weak ignitions by open symbols[5].

Additional non-idealities exist in shock tubes that have received considerable attention in the past, such as reflected-shock bifurcations, pressure rise in the test section (state 5), diaphragm-rupture variability, etc. [133]. Although chemical-kinetics researchers typically model shock-tube data using idealized time-dependent reactors (i.e. assuming constant pressure or constant volume) justifying their choice by the fact that high levels of dilution (N_2 or Ar) are used so that changes are small, when more reactive mixtures are examined or longer test times are targeted such

[5] Although, following an initial guess of Voevodsky et al. [130], we prefer the extension of the second explosion limit because of its simpler physical interpretation, it should be noted that most authors employ instead a fixed value of $\left.\frac{\partial t_i}{\partial T}\right)_p$ to separate the strong and weak ignition regimes, as suggested by Oppenheim [71]. The differences between predictions of the two criteria are small, comparable with experimental uncertainties.

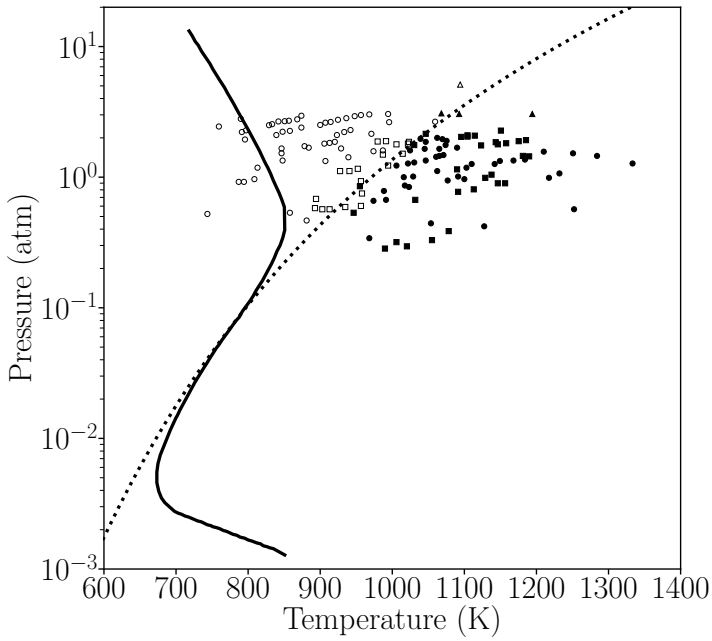

Fig. 26 Weak and strong ignition presented in a temperature-pressure diagram. The explosion limit (solid curve) and the extended second explosion limit $\alpha = 1$ (dotted line) are those of Lewis and von Elbe [1]. Ignition events are taken from ■ Meyer & Oppenheim [131], ● Voevodsky & Soloukhin [130], and ▲ Grogan & Ihme [132]

assumptions are no longer valid. A proper description of the ignition process then requires accounting for spatial gradients, even in the absence of the aforementioned non-idealities if higher accuracy is required [134].

Besides leading to flame propagation, shock-induced ignition may result directly in detonation initiation. Direct initiation of detonation consists of the spontaneous formation of a detonation by a sufficiently intense and rapid energy deposition in a reactive mixture. If the deposited energy is above the minimum ignition energy for detonation initiation, E_c, a spherical shock wave is generated that is strong enough to rapidly activate chemical reactions that subsequently couple with the shock. If the deposited energy is below E_c, the shock wave and the reaction zone decouple, preventing the formation of a detonation. Eckett [135] reported that E_c varies with the induction time according to $E_c \propto \tau_{ind}^3$; E_c values may be found in industrial-safety handbooks and experimental databases [78].

Finally worth mentioning is another type of combustion process that may result from high-pressure fuel leaks into surrounding air and its subsequent heating by the leading shock wave. In this scenario, ignition at the fuel/hot-air interface leads to unintended combustion different from the deflagrations and detonations described above, namely a diffusion flame that is characteristic of non-premixed combustion and that usually is turbulent. Because of the high mass diffusivity coefficient of H_2,

it readily diffuses over the hot air region, mixing, and reaching concentrations in which ignition is possible. Hydrogen is notoriously prone to ignite in this fashion (unlike hydrocarbons) producing jet fires which lead to extensive damage.

2.7 Diffusion flames: extinction limits

For safety reasons, many thermal engines rely – at least partially – on non-premixed combustion. Fuel and oxidizer typically are injected separately and mixed as much as possible by injectors designed to enhance mixing (impinging jets, swirl, etc.), but diffusion flames nevertheless remain present where combustion occurs. The present section addresses the physics governing extinction of strained diffusion flames.

A configuration often considered in experimental and numerical investigations is the jet flame sketched in Fig. 27, where a cold jet of fuel is ejected into an air atmosphere that may be at atmospheric conditions or at hot-gas temperatures. At

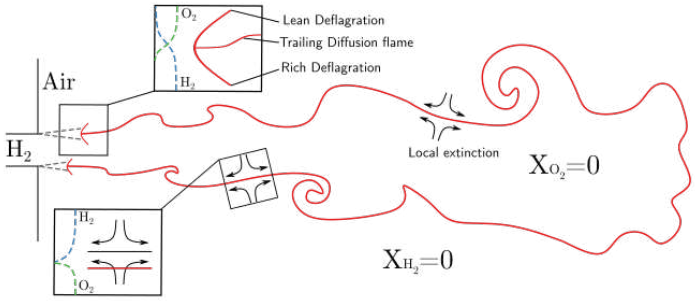

Fig. 27 Sketch of a hydrogen-air jet diffusion flame.

high Reynolds numbers, the reaction occurs in small mixing layers distorted and strained by the flow, as illustrated. The strain rate of the flow affects the burning rate and may cause local extinction of the flame, creating holes in the flame surface, bounded by edge flames that act as extinction or re-ignition fronts [20].

The flame structure in diffusion-flame fronts, analyzed by Liñán in [136], is governed by a diffusion-reaction balance under the influence of the external strain. A classical configuration enabling detailed study of this balance is the counterflow configuration, sketched in Fig. 28, composed of impinging uniform streams of fuel and oxidizer.

To characterize the strain rate, what currently often is called the global strain rate has been introduced [137], based on conditions in the oxidizer stream,

$$a_{\text{air}} = \frac{2|v_{\text{air}}|}{L}\left(1 + \frac{v_{\text{H}_2}\sqrt{\rho_{\text{H}_2}}}{v_{\text{air}}\sqrt{\rho_{\text{air}}}}\right). \tag{82}$$

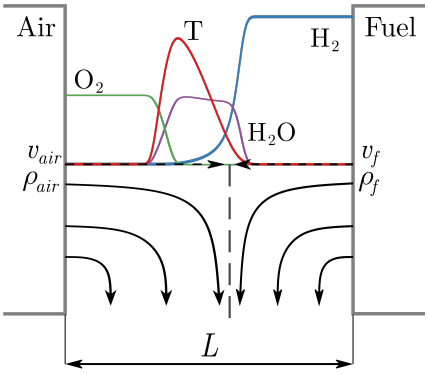

Fig. 28 Sketch of the canonical counterflow hydrogen-air jet diffusion flame.

Experimentally, combustion is first initiated at a low strain rate, then this global strain rate is progressively increased by increasing the feed-stream inflow rates, maintaining the momentum-flux ratio constant so that the flame position remains fixed, until the flame extinguishes. Prior to extinction, the maximum temperature in the flow increases with strain rate because of the increase of the diffusive influx of reactants with decreasing characteristic length scales, as is shown in Fig. 29.

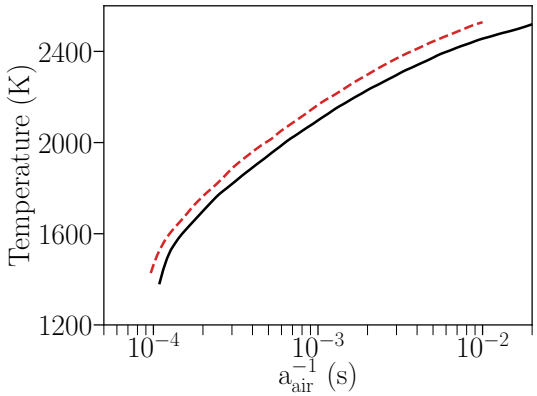

Fig. 29 Dependence of the flame temperature on the global strain rate for a diffusion flame of hydrogen in air at atmospheric conditions. The solid curve is the prediction of the San Diego mechanism, while the dashed curve is obtained from a 2-step reduced mechanism. The data are extracted from [18, 20, 138].

Niemann et al. [139] obtained the pressure dependence of the strain rate at extinction both experimentally and numerically, as is shown in Fig. 30, along with results of a more recent experiment and predictions of the San Diego mechanism by a finite-difference method that likely is close to potential flow. These results are

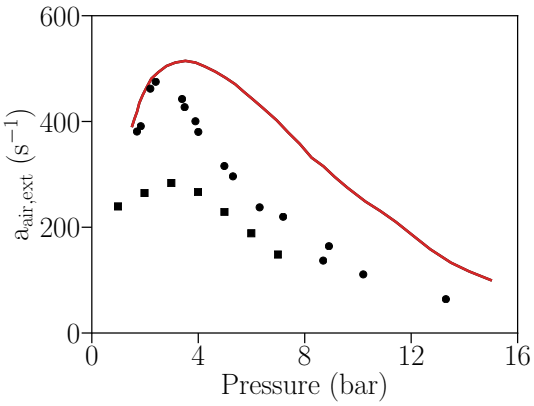

Fig. 30 Strain rate at extinction, $a_{air,ext}$, as a function of the ambient pressure for a diffusion flame of a hydrogen/nitrogen mixture with a hydrogen mole fraction of 0.14 flowing against air . The solid curve is obtained from the San Diego mechanism [3]. Square points correspond to experimental results of Park et al. [140], while the circular points represent the experimental results of [139].

illustrative of the degree of agreement that has been achieved. The differences seen here are appreciable because these counterflows are rotational and different extents of rotation are present in different experiments as a consequence of different flow-exit screen or honeycomb arrangements; potential-flow predictions fail to account for the rotational flow and overpredict extinction strain rates, although chemical-kinetic uncertainties at pressures above 4 bar are so great that differences in predictions of different current mechanisms are comparable with the differences seen in the figure.

Near the limit of extinction, the minor species O, OH, HO_2, and H_2O_2 satisfy the quasi-steady state assumption, QSSA, (approximations A3 & A4), and the chemistry that then governs the extinction process is described by 11 elementary steps:

1	$H + O_2 \rightleftharpoons OH + O$
2	$H_2 + O \rightleftharpoons OH + H$
3	$H_2 + OH \rightleftharpoons H_2O + H$
4	$H + O_2(+M) \longrightarrow HO_2(+M)$
5	$H_2 + O_2 \rightleftharpoons HO_2 + H$
6’	$HO_2 + H \longrightarrow 2\,OH$
7’	$HO_2 + OH \longrightarrow H_2O + O_2$
8’	$H + OH + M \rightleftharpoons H_2O + M$
9’	$2H + M \rightleftharpoons H_2 + M$
10’	$2HO_2 \longrightarrow 2OH + O_2$
11’	$HO_2 + H_2 \longrightarrow 2OH + H$

The corresponding rates are provided in standard format in [27], as extracted from the San Diego detailed mechanism [3]. The first five of these reactions correspond to those of the skeletal mechanism for autoignition, while the last two are obtained from the H_2O_2 QSSA, typically applicable in diffusion flames while not applying to deflagrations or to autoignition processes. This specific numbering is only

valid throughout this section (Eqs. 83 through 84). Given this skeletal mechanism, introduction of the applicable QSSA leads to two-step reduced mechanism

$$\begin{aligned} 3H_2 + O_2 &\xrightarrow{\text{I}} 2H_2O + 2H \\ H + H + M &\xrightarrow{\text{II}} H_2 + M, \end{aligned} \tag{83}$$

with the rates

$$\begin{aligned} \omega_{\text{I}} &= \omega_1 + \omega_{6'f} + \omega_{10'f} + \omega_{11'f} \\ \omega_{\text{II}} &= \omega_{4f} + \omega_{8'} + \omega_{9'} - \omega_{10'f} - \omega_{11'f}, \end{aligned} \tag{84}$$

which can be expressed explicitly by making use of the steady-state expressions for O, OH, and HO_2 species as is shown in [27, 138].

3 How to ignite: Ignition strategies

The objective of this part is to provide a brief overview of ignition strategies that are available for potential hydrogen thermal engines. The examples come mainly from cryogenic-engine applications.

3.1 A simplified conceptual model of a H_2 combustion chamber

Figure 31 is an illustration of components of a conceptual model for a H_2 thermal engine. For simplicity, the flow rate of fuel injection is assumed to be controlled by a valve that can be opened or closed at a constant rate, as is the flow rate of injection of the oxidizer, which may be anything from vitiated air to pure O_2. In applications employing air, the equivalence ratio generally is less than unity, the fuel being the more expensive reactant, but rocket engines usually use pure O_2 since they have to carry both reactants, and they are designed to operate fuel-rich because the consequent lower molecular weight of the product mixture improves the performance, increasing the specific impulse, and oxygen is more aggressive than hydrogen in damaging hot chamber walls.

3.2 Ignition sequence

The first design decision to be made is a specification of the ignition sequence, which determines the conditions present in the chamber during engine ignition. In the simple configuration considered here, three timing selections are important, namely start of oxygen injection (t_O), start of fuel injection (t_F), and start of igniter

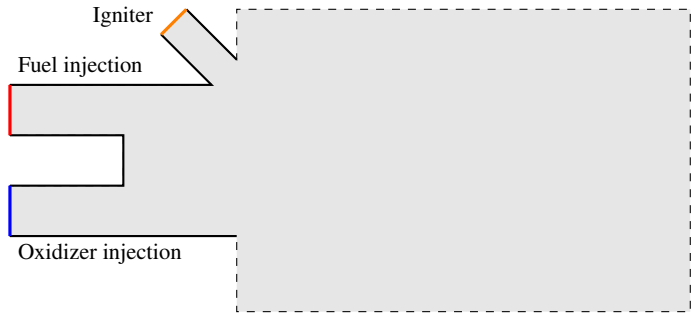

Fig. 31 Sketch of a model combustion chamber, with an arbitrary F/O injection system (co-axial, swirl, or whatever), and an igniter inlet for high-temperature gas injection.

(t_{ig}). Adjusting the ignition sequence consists in setting the appropriate timeline to ensure safe, reliable, and systematic ignition.

A typical ignition sequence, shown in Fig. 32, accounts for several constraints. For

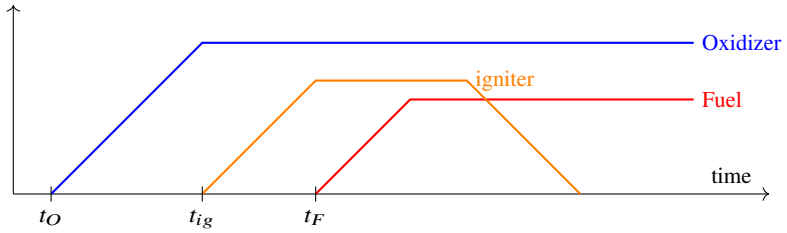

Fig. 32 An example of an oxidizer-rich ignition sequence. The lines represents the mass fluxes, or potentially the power delivered by the igniter.

instance, it is clear that for operating equivalence ratios less than unity one should not open the H_2 valve full throttle before being sure that the chamber is ignited because otherwise there is a risk of filling a large volume with a potentially explosive H_2–O_2 mixture. Generally speaking, it is a good idea to open the valve of the limiting reactant last, to avoid passing through stoichiometric conditions during the ignition transient. Most engines are not designed to cope with the extreme temperatures that would be encountered close to stoichiometry.

Having chosen an oxidizer-rich ignition sequence, one then has to decide where to place the igniter in the sequence, taking into account the following considerations: (i) The igniter has to be working long enough for the engine to be ignited. (ii) It is safer to turn on the igniter before t_F, to make sure it is properly turned on. (iii) The igniter has to be still operating when the equivalence ratio in the chamber, which increases with time starting at t_F, reaches the lean flammability limit of the fuel/oxidizer mixture. (iv) The igniter should ignite the mixture in the combustion chamber as early as possible, to avoid accumulation of unburnt premixed gases,

which may result in a subsequent strong pressure rise during ignition as the mixture burns. In light of these constraints, a safe choice is to turn on the igniter very close to t_F, preferably just before.

For large combustion chambers, it is often convenient to relocate ignition into a small separate combustion chamber, with exhaust close to the injection system of the main chamber. This is the strategy of torch igniters (e.g., the augmented spark igniter of former Space-Shuttle engines). This decouples the igniter-chamber sequence from the main-chamber sequence, and it can be designed to ignite a controlled fraction of the main fuel/oxidizer mass flux by diverting a small fraction of it through a pre-chamber that serves as the igniter. See [141] for an example of an oxidizer-rich ignition sequence for a fuel-rich engine.

Note that cryogenic engines are mostly operating in non-premixed mode, so developing a premixed H_2 combustion chamber, as is desired in some gas-turbine applications, will probably yield additional constraints, and relocating ignition in a small separate (non-premixed) chamber may be the easiest option.

3.3 Minimal thermal power required

Adequately adjusting the igniter power required is the most critical choice in igniter design, especially when weight or volume is a design criterion (e.g. in the transportation sector).

3.3.1 Rule-of-thumb specification

Consider the Vinci rocket engine, designed to power the new upper stage of Ariane 6. The mixture ratio (fuel-to-oxidizer mass-flux ratio) is close to 6 during steady operation, with a total mass-flux rate on the order of 40kg/s (see, e.g. the communication brochure from ArianeGroup). The igniter essentially injects burnt gases into a region near the center of the injection plate, much like the augmented-spark igniter of the former Space-Shuttle main engine.
The igniter power required to produce ignition in the engine is

$$P_{ig} = \dot{m}_{ig}.c_p.\Delta T, \tag{85}$$

where c_p is the heat capacity of the mixture to be ignited, close to $c_p = 3 \times 10^3\,\mathrm{J\,kg^{-1}\,K^{-1}}$ (standard conditions), ΔT is the temperature increment required to obtain ignition (≈ 1000 K), and $\dot{m}_{ig}$ ($\mathrm{kg\,s^{-1}}$) is the fresh-gas mass flux needed to ignite at the time of ignition (highly dependant on the ignition sequence).

The quantity $\dot{m}_{ig}$ is the most difficult factor to estimate, but, in particular for the example being considered here, one can safely assume (i) that the total mass flow rate during ignition is only a small fraction of the steady mass flow rate, since the combustion chamber pressure is close to 1 bar at ignition (whereas the engine is

designed to operate at 60 bar.), and (ii) only a fraction of the injectors (those close to the igniter outlet) need to be ignited since the remainder of the injectors will ignite subsequently through flame propagation. Assuming the flow rate at ignition to be 1/60th of the steady-state flow rate (the ignition pressure is lower by a factor of 60), and that igniting 20% of the injectors is sufficient to achieve good ignition, one obtains 400 kW, a result close to the 440 kW value reported in early developmental reports [142].

What has just been described is an oversimplified rule that is to be followed with much caution; successful ignition of a complex system involves countless parameters. See [143] for a classical ignition sequence of an annular combustion chamber. Once the burnt-gas flow rate of the igniter (or, equivalently, igniter thermal power) is known, ignition may be obtained by one of the techniques to be listed in a following section.

3.3.2 Additional steps to improve igniter specification

Direct numerical simulations (DNS) can provide highly relevant information regarding the ignition characteristics of a combustion chamber. For instance, Carpio et al. [144] studied the critical radius of a burnt-gas jet issuing into fresh gases, required for successful ignition (which depends on the local conditions, burnt-gas velocity, and local Reynolds number). Large-eddy simulation (LES) is also a very valuable tool in unraveling the ignition-sequence dynamics, as is suggested by the abundance of articles on the topic (see, e.g. [143, 145]).

The methods presented in Sec. 4.4 to detect potential H_2 ignition based on cold-flow simulations also can be useful for obtaining an estimate of the properties of the flow required for ignition during the transient process. Other studies [146–149] go a step further and analyze ignition-kernel histories, to assess the probability of ignition success (or alternatively, the probability of ignition-kernel quenching).

3.4 A list of igniter technologies

The list below is not exhaustive but covers the most common alternatives.

3.4.1 Pyrotechnic ignition

In this strategy, a small solid propellant is ignited and burnt, with its exhaust gases directed to enter the combustion chamber in the vicinity of the injectors. This type of ignition device is employed in the Vulcain 2 engine currently flying on Ariane V [150]. It is highly robust, but has the disadvantage of being a one-shot method (although in some cases multiple solid-propellant charges are included).

3.4.2 Glow-plug ignition

A glow plug, similar to those found in diesel engines, can also be used for ignition [151]. It can raise the temperature into the range 1000-1200 K for a few seconds, enough to reach ignition temperatures if the fuel/oxidizer mass flux is small enough and well enough controlled. The system is simple, but it requires an electrical system. Another disadvantage is that heating up to the target temperature can take 10 s, which would be too long for very time-sensitive ignition sequences if variability is important. Heating and transferring the heat to the mixture is not instantaneous and is less controllable than heating by spark plugs.

3.4.3 Spark-plug ignition

Spark plugs are more precise in timing than glow plugs because their energy deposition comes from an electrical ark, which is rapid. This well-known technology is very common; it is used in most gasoline engines and airplane engines, and it was also the strategy used for the former Space-Shuttle Main Engine. There exist several methods in the literature for modeling energy deposition by spark plugs [152, 153].

3.4.4 Laser ignition

A laser can be focused to deposit the energy required to produce ignition into a well-mixed fuel-oxidizer region. Laser ignition presents several advantages over spark-plug and glow-plug systems [154], especially the extremely precise timing that it can achieve. The laser may be focused more easily onto a region of interest (unlike glow plugs and spark plugs, which typically are close to a wall). Lasers also can produce leaner ignition [155], which allows for earlier and smoother ignition in the sequence. Also unlike glow plugs and spark plugs, there is no erosion over time, but maintenance is required for the optical system. Several models are available for laser energy-deposition processes [28, 156].

3.4.5 Hypergolic ignition

There are propellant combinations for which hypergolic ignition can be achieved [157]. The most famous probably is nitrogen tetroxide N_2O_4 with hydrazine N_2H_4 (and their derivatives), which was used to propel a number of rockets as main propellants, e.g. the Viking engine from Ariane IV. Since these compounds react directly upon contact, they do not require external energy for ignition (thereby bypassing entirely the need for an igniter), but they tend to be extremely volatile, toxic, corrosive, and carcinogenic, which are severe drawbacks, although research towards use of less toxic compounds to the same end is an active topic of investigation [158, 159].

3.4.6 Acoustic ignition

An acoustic resonator can be used to obtain ignition without electrical initiation [160]. Removing the electrical system needed for glow plugs or spark plugs not only makes the igniter lighter and more compact, but it also makes it more robust to failure scenarios.

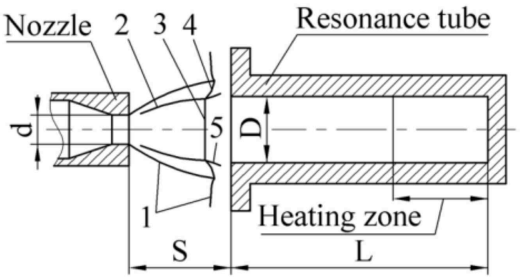

Fig. 33 Hartmann Sprenger (HS) tube principle sketch, from [161]. 1- gas jet boundary, 2- oblique shock, 3- Mach disc, 4- reflected shock, 5- boundary of internal subsonic zone

The acoustic generator for ignition, first reported in 1927 [162], was further extended to heat flows in so-called Hartmann-Sprenger (HS) tubes, following the principle described in Fig. 33. Early studies [163, 164] indicate that a Mach 2 jet can heat helium to 900 K in about 0.2 ms using a rather short (1cm) tube. A distinct advantage of this technique is that it requires only a moderate over-pressure (a few bars) to establish the small under-expanded jet that is needed.

Theoretical descriptions of the ignition mechanism exist, but they are scarce [165], with only moderate agreement between theory and experiments. Experimental [161, 166] and numerical [167, 168] studies also exist, but there is a clear gap to fill theoretically. In particular, the relationships between the maximum temperature reached, the Mach-disk position, and the generating pressure seem unclear.

4 How not to ignite: Application to safety issues

In the process of transition to widespread use of H_2 as a primary fuel, a central topic is H_2 storage and safety. H_2 being among the most fugacious gases, the question is not "whether a given system will leak", but "how much it will leak". In that context, the question of potential hazardous ignition is central. Combustion devices contain regions of hot-gas environments or hot solid parts, and risk assessment in these regions is particularly tricky.

For instance, most cryogenic H_2-O_2 rocket engines use He extensively as diluent wherever the fuel and oxidizer may come together. The choice of He is dictated by the extreme (cryogenic) temperatures – as low as 22 K in the vicinity of liquid H_2–

under which most other classical diluents (e.g. N_2) are in solid form. He, however, is a very expensive fluid, thereby motivating minimal usage of it.

4.1 A simple rule-of-thumb example.

The feed systems of a hydrogen thermal engine must raise the pressure of hydrogen in the lines up to a value close to the chamber pressure p_c. The pressurizing system therefore is likely to develop H_2 leaks, sometimes in an oxidizer environment. A first approach to addressing this problem consists in assessing characteristic times of the system, e.g. making estimates based on mean-flow velocities or hot-wall temperature distributions, and comparing these times with the branching time that appears in (28). If the branching time is too close to one of the characteristic times of the system, there is a safety risk, leading to an explosion potential. This can be avoided in several ways:

- lower the temperature of the hot environment (e.g. by cooling the walls),
- increase the departure from stoichiometric conditions $\|\varphi - 1\|$, to lower the reactivity,
- use an inert-gas supply to dilute the environment, thereby increasing characteristic branching times.

If the configuration is complex and far from canonical cases available in the literature, it is possible to resort to numerical simulation, making use of the numerical tools identified below. Reliance on numerical methods of computational fluid dynamics (CFD) can be quite helpful if they are not too expensive or time-consuming.

4.2 A computational example: The Cabra H_2 jet flame

The illustrations to be given in this section are obtained by post-processing a numerical simulation of the turbulent lifted H_2 jet flame studied experimentally by Cabra et al, [169], as sketched in Fig. 34. This test case is selected because of its close correspondence to safety scenarios; the experimental arrangement is clearly reminiscent of a hydrogen leak in a hot environment. It consists of a 300K H_2 jet ejected at Mach 0.3 into a coflow with a temperature slightly higher than the crossover temperature. Because of the proximity of the coflow temperature to the crossover temperature, ignition occurs far downstream from the injector, with a characteristic time therefore comparable with the convective time, as in Sec. 2.4. Cheng's flame [170] could be another valid example; with an exit velocity of Mach 2, it would approximate a leak from a high-pressure H_2 tank.

The simulation employed here was performed with ProLB software [171] following the approach presented in [172–174]. The conditions addressed are listed in Tab. 7, and Fig. 35 presents the simulation results along with a comparison of experi-

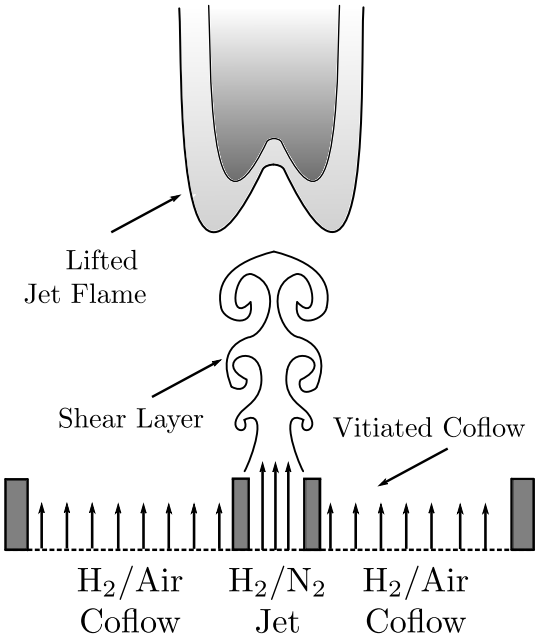

Fig. 34 Jet configuration experimental setup and flame structure from Cabra et al. [169]

mental and numerical temperature profiles along the central axis, the latter showing excellent agreement in the induction region (up to 15 diameters), the region of interest for this section, while the temperature over-estimation further downstream, not of interest here, is due to the *implicit* modeling, that is, the absence of a turbulent-combustion model. For a more complete test of the simulation the reader is referred to [175]. For presenting the simulation results in the upper figure, the so-called Q-criterion explained in Appendix 2 is adopted. Along the surface of the selected value of Q, identifying vortices in the turbulent flow, temperature is color-coded from blue for the cold inlet gases to red for hot in the region where ignition is occurring, and, in addition, the H-atom concentration is coded with increasing shades of gray indicating increasing concentrations that mark reaction-zone locations.

	Central jet	Coflowing jet
D (mm)	4.57	210
T (K)	305	1045
U (m/s)	107	3.5
Re	23 600	18 600
X_{H_2}	0.2537	0.0
X_{O_2}	0.0	0.0989
X_{N_2}	0.7427	0.7534
X_{H_2O}	0.0	0.1474

Table 7 Initial conditions for the jet flame [169]

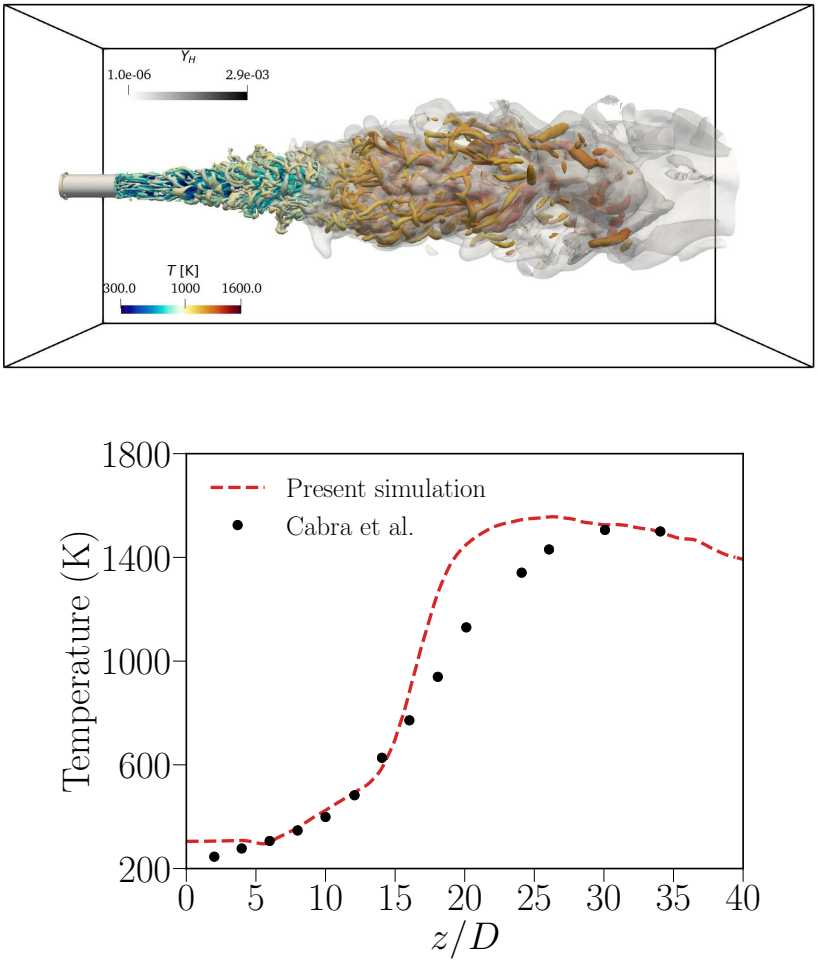

Fig. 35 Top: Instantaneous Q-criterion [176] iso-surfaces colored by temperature and iso-contours of the H-radical mass fraction, maximum values denoting the presence of auto-ignition (light gray). Bottom. Center-line temperature profiles as obtained numerically (dashed line) and experimentally (symbols).

4.3 Post-processing

Post-processing the numerical simulation is performed to identify regions where autoignition occurs by successively identifying:

1. where the mixture may ignite, e.g. where it is most reactive.
2. where the mixture does ignite (within the reactive zones).

4.3.1 HO_2 as an autoignition indicator

The hydroperoxyl radical HO_2 typically achieves its peak concentration in regions where ignition is occurring and therefore has been used extensively for detection and visualization of autoignition in lifted flames [177–179]. However, HO_2 also peaks in ignited mixtures near the fuel-rich reaction zones of flames [180]. Moreover, its concentration during autoignition processes changes drastically with local conditions, which can hinder the detection of certain autoignition spots when several local maxima (in HO_2 level) are simultaneously present. Nonetheless, HO_2 may be used for an initial approximation in detecting autoignition, as illustrated in Fig. 36. Comparison with the simulation shown in the previous figure reveals that this offers an appreciably more revealing and robust representation of the ignition regions than is obtainable from temperature color-coding, for example.

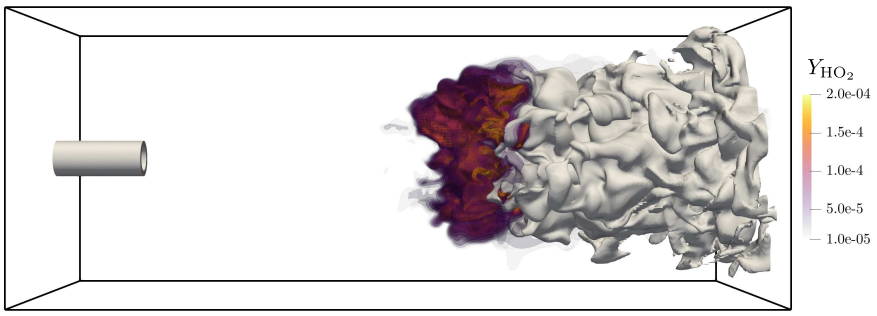

Fig. 36 Lifted flame HO_2volume rendering (colored with HO_2mass fraction) in the Cabra flame simulation. Downstream, temperature iso-contour at 1600K in gray, identifying the flame.

4.3.2 Reactivity

As outlined in the mixing-layer-ignition Section 2.4, ignition should occur at the most reactive position, e.g. where the branching time ($\sim \lambda^{-1}$) is shortest. Such regions can

be readily identified by computing λ (42) from the mixtures properties throughout the domain.

Figure 37 presents a center-plane snapshot of the instantaneous λ value obtained in the simulated Cabra flame. Given that λ depends only on the local temperature and concentrations C_{H_2} and C_{O_2}, and because these quantities barely change during induction, λ is approximately constant along the most-reacting mixture line, marking reactivity but not the actual occurrence of ignition. Autoignition occurs along this line after sufficient accumulation of HO_2 radicals, which can be identified by an appropriate variable, as presented in next section.

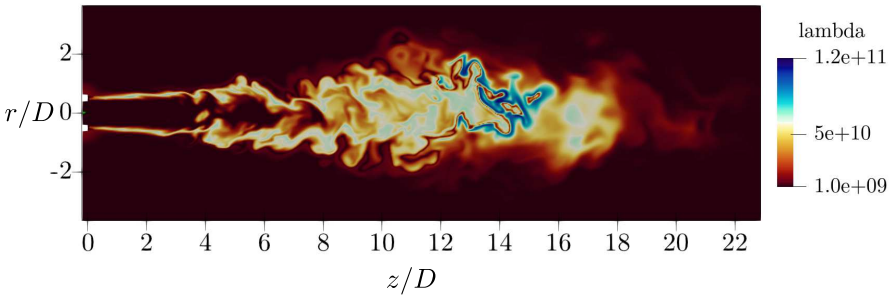

Fig. 37 Snapshot of λ, the reactivity of the mixture.

4.3.3 Autoignition progress / autoignition index

To identify regions where autoignition is actually occurring, it is convenient to introduce a HO_2 steady-state parameter [138, 177, 181], also referred to as autoignition index [179]

$$AI = \frac{\dot{\omega}^P_{HO_2} - \dot{\omega}^D_{HO_2}}{\dot{\omega}^P_{HO_2} + \dot{\omega}^D_{HO_2}}, \tag{86}$$

where $\dot{\omega}_{HO_2}$, the net HO_2 production rate, has been split into $\dot{\omega}^P_{HO_2}$ and $\dot{\omega}^D_{HO_2}$, respectively, its production and destruction rates. Figure 38 shows the evolution of λ, the temperature, and selected species mole fractions in an isobaric, adiabatic, homogeneous reactor with initial conditions p=1 atm, T=1200 K, φ=1, confirming that, as pointed out in Sec. 1, the concentration of H_2, O_2, and H_2O, as well as the temperature and therefore the reactivity λ remain constant during the induction process.

The chemical steady-state parameter AI defined in (86) was originally introduced in [177], and it was used later in [18] to detect autoignition and correct the behavior of a 3-step reduced mechanism for hydrogen combustion. The evolution of AI during autoignition in the homogeneous reactor is included in the lower plot of Fig. 38.

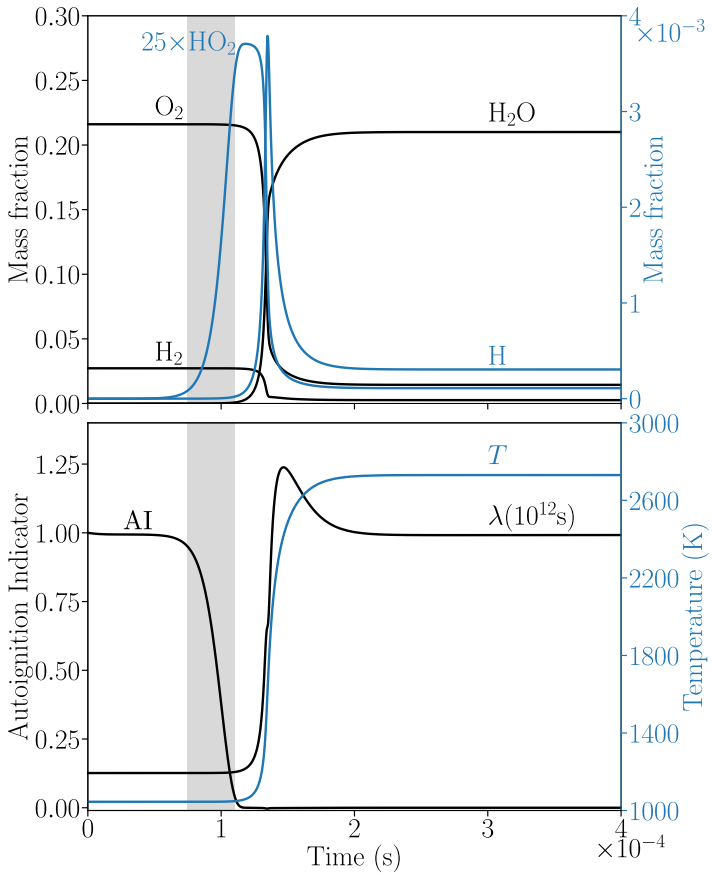

Fig. 38 Evolution of the mole fractions of the main species (top), of H and HO_2 radicals (middle), reactivity λ and autoignition index AI (bottom), and temperature (full-height), during isobaric homogeneous autoignition. Boundaries of the shaded regions at AI=0.95 and 0.05.

Initially, HO_2 cannot be consumed by any of the reactants ($\dot{\omega}^D_{HO_2} = 0$), and it remains unity by definition during this stage. As HO_2 radicals accumulate, it decreases, reaching 0 when the HO_2 concentration reaches its steady state, a condition already identified in Sec. 1 and used to derive the analytical branching time (45).

It is therefore reasonable to identify the autoignition period as the period during which HO_2 progresses towards steady state, that is, when AI decreases. In Fig. 38 a shaded region is included between $AI_{max} = 0.95$ and $AI_{min} = 0.05$ to show that these two values can be chosen as bounds of the autoignition region. Given the variations of AI (see Fig.38), the criterion depends very little on the choice AI_{min}, provided it is sufficiently small (see also [18]). However, the value of AI_{max} is critical in defining the criterion; it has to be small enough to be insensitive to numerical

instabilities, but large enough to capture the induction region. A figure in the next subsection suggest that $AI_{max} = 0.95$ is a good choice[6].

It may be remarked that this parameter may be defined for hydrocarbons as well, several definitions being available in the literature. For instance, Schultz et al. [179] define AI from the competition between rates 10 and 12 in the detailed mechanism of Tab. 1.

4.3.4 Identifying autoignition regions

While stabilization of a turbulent lifted flame by autoignition is more complex than the homogeneous case of Fig. 38, the underlying idea continues to apply in reactive preheated turbulent mixtures, and iso-surfaces with $AI = 0.05$ and 0.95 remain an efficient way to identify the autoignition region, both qualitatively and quantitatively. Figure 39 represents in the center an area corresponding to $0.05 < AI < 0.95$ in the plane of symmetry, its left and right sides being the isosurfaces of AI=0.05 and 0.95, respectively. This region is colored with the reactivity λ, computed from an

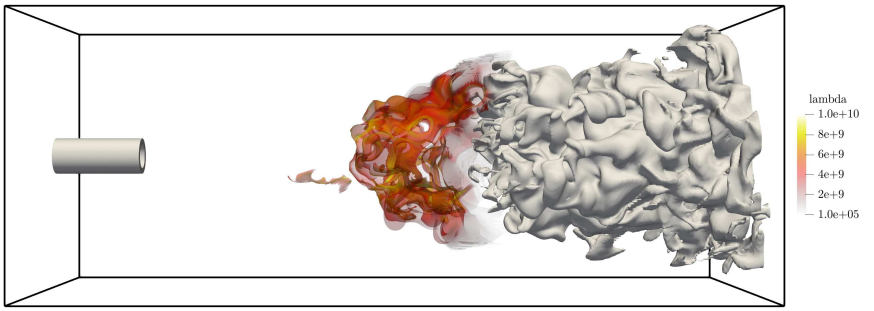

Fig. 39 Post-processed Cabra flame, volume rendering corresponding to $0.05 < AI < 0.95$ colored with λ. In gray downstream, temperature isosurface at T=1600 K.

instantaneous solution. As a reference, a gray temperature isosurface at T=1600K is also plotted, bounding the burnt-gas regions. For visualization purposes the AI iso-surfaces were restricted here to very reactive mixtures, arbitrarily eliminating points where λ is smaller than one third of its maximum value. The volume corresponding to $0.05 < \alpha < 0.95$, well separated from the burnt gases, can then be associated with autoignition kernels. Further study of this ignition region shows that it contains pockets of burnt gases, some visible in Fig. 39, but comparing the burnt-gas region and the autoignition region in Fig. 39 with the HO_2 region and the following flame in Fig. 36 shows the efficacy of the method as an identifier of autoignition.

[6] This same value was also used in post-processing the supersonic H_2-air flame in [181].

4.3.5 Alternative methods

Computational singular perturbation (CSP) [182, 183] provided the required tools that enable the identification of explosive timescales [184]. These tools were incorporated in chemical explosive mode analysis (CEMA) [180, 183], so that the explosive dynamics are currently analyzed by both CSP and CEMA. When the CSP basis vectors are approximated by the eigenvectors of the chemical Jacobian, the approach resembles the one presented herein. Being an algorithmic method, it has been applied to a range of different chemical-kinetic schemes but reduces to **A** (25) in the induction region for the chemistry addressed here, so the fastest explosive timescale identified by CSP/CEMA corresponds exactly to λ (42) [185]. Being fully explicit in the case of H_2 and H_2–CO blends [17], the method discussed above may therefore be easier to use. Formulations for methane and decane exist as well [185].

4.4 A priori prediction of hazardous ignition from cold-flow simulations

Information related to that presented above, extracted from reacting-flow simulations, also can be obtained from cold-flow simulations.

Computational savings of cold-flow simulations are substantial compared to reactive simulations in any given flow field for a number of reasons:

- conservation equations for only the injected species (H_2, O_2, N_2) need to be calculated.
- the chemical time-step constraint is lifted, leaving the CFL and Fourier numbers as the only constraints.
- there is no need to compute any Arrhenius reaction rates.

Such simplifications typically reduce computational costs by 50% to 90%, depending on the numerical method (see, e.g. [186, 187]) and on details of the chemistry-integration cost.

4.4.1 Formulation

Let us now define an ignition tracking variable η, as a passive scalar representative of the quantity of intermediate species during induction. In practice, it will represent the eigenvector associated with the most explosive timescale λ.

A transport-diffusion-reaction equation will be employed to describe the passive-scalar temporal evolution as

$$\frac{\partial \eta}{\partial t} + u_\alpha \frac{\partial \eta}{\partial x_\alpha} = \frac{\partial}{\partial x_\alpha}\left(D_\eta \frac{\partial \eta}{\partial x_\alpha}\right) + \dot{\omega}_\eta \tag{87}$$

to account for potential losses of radical pool η by convection/diffusion, with source and diffusion terms defined below.

It was shown in Sec. 1 that radical-pool growth is associated with a rate of the form $\lambda C + \epsilon$. In (87), η has the units of a mass fraction (dimensionless), so the appropriate source term for (87) reads

$$\dot{\omega}_\eta = \lambda\eta + \epsilon_\eta, \tag{88}$$

where $\epsilon_\eta = W_\eta \omega_5/\rho$ is introduced to maintain proper dimensions.

Lastly, the diffusion coefficient in (87), and molecular weight W_η may be set according to the radical-pool composition (Fig. 6). In the following, $W_\eta = W_\mathrm{H}$ and $D_\eta = D_\mathrm{H}$, since H is the most important intermediate species for the Cabra flame. The scalar is passive in the sense that it does not enter into the mass or energy balance and only plays the role of a tracer variable. Since it is entirely decoupled from the flow, it will not impact at all the computational numerical stability. Last but not least, its purely exponential form makes it easy to integrate exponentially [188], allowing for an accurate description of induction with only a few integration points. Since the production term exactly matches locally the production corresponding to the local ignition eigenmode (see Fig. 5), it is straightforward to see that η will describe exactly the evolution of the radical-pool growth. In particular, once a proper ignition threshold η_{ig} is defined, e.g. from the limiting reactant mass fraction as

$$\eta_{ig} = \min(Y^0_{\mathrm{H}_2}, Y^0_{\mathrm{O}_2}/8)/1000, \tag{89}$$

it is shown in [175] that:

- the time for η to reach η_{ig} in a homogeneous reactor very accurately matches the ignition delay time obtained with detailed chemistry (as in Fig. 2).
- the same holds for the ignition history in temporally or spatially evolving mixing layers (the configuration studied in Sec. 2.4).

Figure 40 shows the evolution of the passive scalar for the cold-flow simulation corresponding to the reactive simulation presented in Fig. 35. Iso-surfaces of the Q-criterion [176] show that the flow structure is similar to that of the reactive simulation in which the flow becomes turbulent at the inlet. Contours of the passive scalar are presented up to the auto-ignition criteria η_{ig} with a transparent grey color.

Note that, since all radical mass fractions grow with the same characteristic time λ^{-1} during branching, the same applies to η, which behaves in a manner very similar to that of H (see Fig. 35), the dominant radical at the local temperature/pressure conditions (see Fig. 6).

In order to further analyze whether the auto-ignition distance is predicted correctly by η, two-dimensional cross-sections of the instantaneous and mean flow field are exhibited in Fig. 41. In each plot, the top half corresponds to the cold-flow simulation (with the white line marking $\eta = \eta_{ig}$), and the bottom half, the reactive flows (with the white line corresponding to $Y_\mathrm{OH} = 6 \times 10^{-4}$, marking the flame). The white lines indicate a flame lift-off close to z/D =10, in excellent agreement with the experiment.

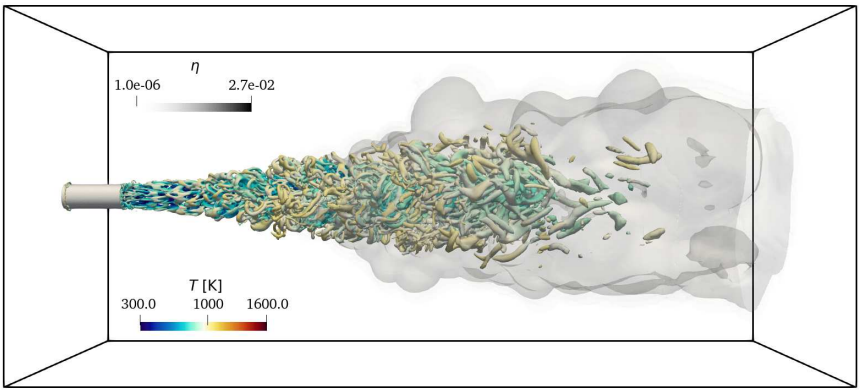

Fig. 40 Instantaneous iso-surfaces of the Q-criterion, colored by temperature. Iso-contours of the passive scalar in the figure denote the prediction of auto-ignition.

4.4.2 A predictive model for ignition

To test further how closely the cold-flow computations can reproduce reactive results, computations are made with the coflow temperature varied from 1025 to 1055 K. As expected, the flame behavior is extremely sensitive to the coflow temperature [189, 190]. At 1045 K (the experimental temperature), the lift-off height is about 10 D. Decreasing the coflow temperature by 15 K increases the lift-off height to 16 D, and, with a decrease as little as 20 K, the jet no longer ignites. Figure 42 shows results for both hot-flow and cold-flow simulations, demonstrating excellent agreement, even in predicting the absence of ignition, where η never reaches η_{ig}.

Other computational methods have also been used to track ignition kernels based on LES simulations [146–149], but they focus more on the ability of a hydrocarbon thermal engine to sustain successful ignition (e.g. without quenching) rather than on detecting the first ignition kernels. With H_2 being less prone to quenching once above the second explosion limit, the model presented here may be sufficient.

5 Conclusions and Perspectives

The road to tomorrow's broad use of H_2 thermal engines is paved with technological and scientific challenges. Luckily, even though hydrocarbons have been the most widely employed fuel for the past 80 years – with the notable exception of rocket propulsion – the scientific community certainly has not neglected the study of hydrogen combustion, thereby leaving us with an abundant literature on the topic.

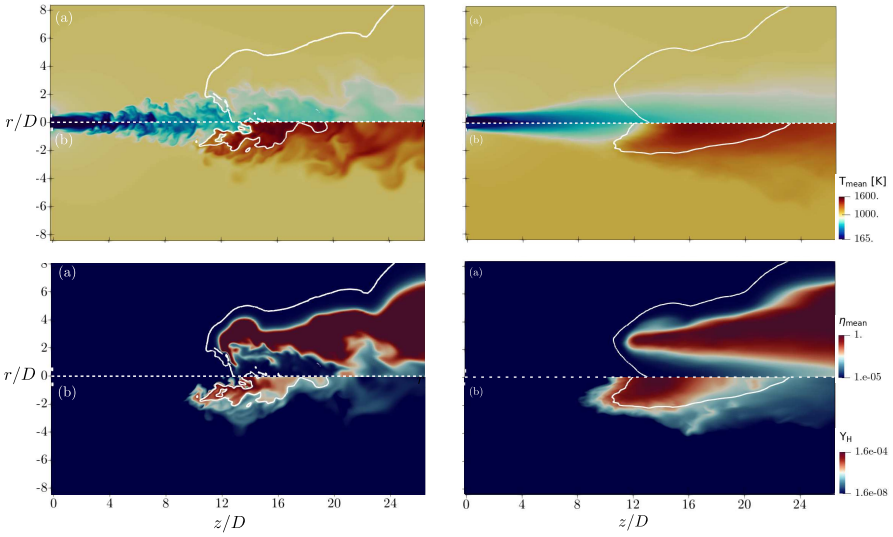

Fig. 41 Temperature (top) and η (bottom) contours for the cold flow simulation (a) compared to the reactive simulation (b). The auto-ignition condition ($\eta = Y^0_{H_2}/1000$) is indicated by white-line contours for non-reactive computations and for $Y_{OH} = 6 \times 10^{-4}$ as taken from the reactive simulation [175]. Instantaneous quantities are represented in the left column, while mean quantities are in the right column.

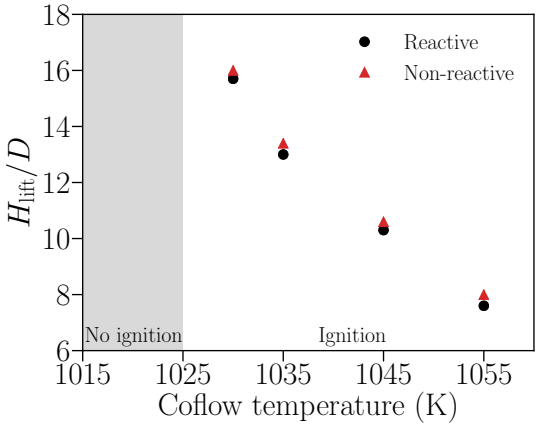

Fig. 42 The effect of coflow temperature T_{co} on the lift-off height normalized by the jet diameter. Comparison between results of the reactive simulations and predictions obtained from the passive-scalar cold-flow cost-saving formulation.

Important sources of difficulty in developing H_2 thermal engines are the H_2 flammability and explosion limits, which are much wider than those of conventional hydrocarbons. It has, however, been shown in this chapter that the various limit

behaviors of H_2 involve simpler chemistry than those of conventional fuels, resulting in low-order analytical approaches becoming available for hydrogen.

Most important for addressing hydrogen ignition and safety is the second explosion limit [1], which is a fundamental property of H_2 oxidation. Successful description of the underlying branched-chain reactions earned Semenov and Hinshelwood a Nobel prize in 1956. The behavior on either side of this limit is so markedly different that a step function at the crossover temperature T_c or the smooth function α, defined in Sec. 1.3, is enough to describe most limit phenomena. In particular, it was seen in this chapter that ignition delays (Sec. 1), explosion limits (Sec. 2.1), flammability limits (Sec. 2.2), and detonability limits (Sec. 2.3), were all intimately related to the crossover temperature. Even though H_2 oxidation is an important part of any hydrocarbon oxidation process, the transition between low-temperature and high-temperature hydrocarbon combustion regimes is not so clear (sometimes involving even negative temperature coefficients), which makes it more difficult to define those limits properly for hydrocarbons.

Thanks to the very stiff behavior of H_2 around the second explosion limit, ignition control may be easier to achieve with H_2 than with conventional hydrocarbons. Hydrocarbon flames quench easily, and ignition models for them typically must take into account ignition-kernel histories to ensure that sufficiently complete combustion occurs once the igniter is turned off. With such exceptional flammability limits, hydrogen thermal engines are unlikely to extinguish after the ignition energy is deposited, significantly simplifying the ignition models required during design and diagnostic investigations.

If igniting a thermal hydrogen engine is *a priori* easier than igniting its hydrocarbon counterpart, ensuring an ignition-free environment everywhere around the engine is much more complex. Leakage of H_2 into a potentially hot oxidant-rich environment (e.g. the exhaust gas of an engine designed for fuel-lean operation) can be disastrous. H_2 flames may also propagate through extremely narrow gaps, where hydrocarbons would quench and be extinguished.

Concerning the variety of possible ignition strategies, acoustic ignition is attractive to employ (see Sec. 3.4), but it remains a phenomenon that is not fully understood and that therefore deserves further analysis. More work is thus required to establish predictive models for investigations of ignition and flashback-protection measures in configurations relevant to future H_2 thermal engines. This is especially true under high-pressure conditions, at which fewer experiments have been conducted, and for which kinetic rates are not as well established. More work is also required for tackling safety concerns associated with the (many) potential accident scenarios, including collision or explosion of a H_2 container (whether cryogenic or high pressure), or tank flash-emptying in open or confined environment.

Mixture compositions affect induction or explosion times substantially, there being strong variations of these times with the equivalence ratio and the extent of dilution. Comparison of these time scales with convection, diffusion and heat-conduction times become important in ignition, design, and safety considerations and, while not reflected in the crossover temperature, they are taken into account in the reactivity measure λ defined in Sec. 1.4. An explicit formulation for this inverse characteristic

branching time is available (Sec. 1.6). This formulation is used throughout the present chapter, showing its relevance to ignition considerations and safety-related issues. In particular, through its derivation based on the chemical-source-term Jacobian, the formulation takes into account not only the pressure and temperature dependence (as does T_c and α), but also the effect of the local composition (including potential dilution), which is essential for establishing ignition-probability maps, as shown in Sec. 4.

There is increasing interest in the use of H_2 along with other fuels. This complicates investigations of ignition and safety by bringing in additional chemical-kinetic steps that have to be considered. In some cases, the notable extensive reductions achievable with H_2, leading ultimately to explicit analytical descriptions (unlike what is available for hydrocarbons), may well be developed, while in other cases that is not likely to be possible. For example, extensive studies of syngas fuels have revealed quite significant possible reductions for CO addition to H_2. Considering replacement of methane by mixtures of H_2 and NH_3 for environment-friendly gas-turbine applications raises interest in the chemistry of mixtures of hydrogen with ammonia; possible reductions for that chemistry have not yet been addressed but should be because it may well be possible to obtain explicit descriptions for flammability characteristics (ignition properties, reactivity, and flammability limits) of such mixtures that are nearly as simple as those for H_2. There also may be interest in other additives, such as ozone O_3 and hydrogen peroxide H_2O_2, which may not be amenable to so extensive degrees of reduction. Much more research is needed on these topics.

Acknowledgements The lead author is indebted to Antonio Sánchez, Carmen Jiménez and Forman Williams for introducing him to H_2 combustion and safety research. He also acknowledges his former colleagues from Snecma (now ArianeGroup) and CNES for providing him with the best insider view into rocket ignition that anyone could ever hope for. Finally, he acknowledges his current industrial partners for their support, and also for sharing such interest in H_2 combustion.

Appendix 1 – QSSA

The quasi-steady-state approximation (QSSA), commonly used in reducing the hydrogen oxidation chemistry, is a simplification that applies to the description of reaction intermediaries when their effective production and consumption times are much smaller than the corresponding accumulation and transport times (by convection or diffusion). Under those conditions, the accumulation, convection and diffusion terms in the corresponding conservation equation are much smaller than the chemical terms, and can be neglected in the first approximation, thereby reducing the governing equation of the steady-state radical to a balance between chemical production and consumption. This algebraic equation replaces the corresponding differential equation in the flow-field description, thereby reducing by one the order of the system of differential equations to be integrated. In many instances, the

chemical balance can be solved explicitly for the concentration of the steady-state species.

The term "quasi-steady-state" was coined in the original developments, dealing with transportless homogeneous systems, for which the approximation amounts to neglecting the time variation of the given intermediate species. To illustrate the approximation, it is of interest to consider a simple chemical system consisting of two elementary unimolecular reactions

$$\mathrm{A} \xrightarrow{1} \mathrm{B} \xrightarrow{2} \mathrm{C}, \tag{90}$$

where A is the reactant, B the intermediary species, and C the product. With C_i denoting the concentration of species i and k_j being the reaction-rate constant of reaction j, so that for instance $k_1 C_\mathrm{A}$ is the rate of reaction 1, the corresponding system of homogeneous balance equations can be written as

$$\frac{\mathrm{d}C_\mathrm{A}}{\mathrm{d}t} = -k_1 C_\mathrm{A}, \qquad \frac{\mathrm{d}C_\mathrm{B}}{\mathrm{d}t} = k_1 C_\mathrm{A} - k_2 C_\mathrm{B}, \quad \text{and} \quad \frac{\mathrm{d}C_\mathrm{C}}{\mathrm{d}t} = k_2 C_\mathrm{B}, \tag{91}$$

to be integrated with initial conditions $C_\mathrm{A} - C_0 = C_\mathrm{B} = C_\mathrm{C} = 0$ at $t = 0$.

For the unimolecular reactions considered, the reciprocal of the reaction-rate constants have dimensions of time. As can be seen in the first equation of (91), k_1^{-1} represents the characteristic time for reactant consumption, that is, the characteristic time required for the reactant concentration to decrease by an amount of the order of its initial value. The steady-state approximation for the intermediate B arises when the reaction-rate constant k_2 is much larger than k_1. To see this, note that at times of order k_1^{-1}, a simple order of magnitude analysis in the second equation of (91) yields $C_\mathrm{B}^*/(k_1^{-1})$, $C_0/(k_1^{-1})$, and $C_\mathrm{B}^*/(k_2^{-1})$ for the accumulation, production and consumption rates of the intermediate B, with C_B^* representing its unknown characteristic concentration. Clearly, if $k_2 \gg k_1$ the accumulation rate becomes negligibly small compared with the consumption rate, and can be neglected in the first approximation, so that the corresponding equation for the evolution of C_B reduces to $k_1 C_\mathrm{A} - k_2 C_\mathrm{B} = 0$. The physical interpretation is that in the limit $k_2 \gg k_1$, the consumption rate of B is so rapid that this intermediate is consumed as soon as it is created, without significant accumulation, thereby resulting in a small quasi-steady-state concentration

$$C_\mathrm{B} = \frac{k_1}{k_2} C_\mathrm{A} \tag{92}$$

changing slowly with time as the reactant is consumed. Note that $C_\mathrm{B} \ll C_\mathrm{A}$ because $k_1 \ll k_2$, indicating that intermediates in steady state appear in concentrations that are much smaller than those of the reactants. This characteristic is often used in realistic computations to identify radicals in steady state.

The solution for $k_2 \gg k_1$ therefore reduces to the integration of

$$\frac{dC_\mathrm{A}}{dt} = -k_1 C_\mathrm{A} \qquad \text{and} \qquad \frac{dC_\mathrm{C}}{dt} = k_1 C_\mathrm{A}, \tag{93}$$

where the second equation is obtained by substituting the steady-state expression (92) into the third equation of (91). The reduced problem (93) can be interpreted as the result of the equivalent chemical-kinetic scheme

$$\mathrm{A} \overset{k_1}{\rightarrow} \mathrm{B} \overset{k_2}{\rightarrow} \mathrm{C} \qquad \Longleftrightarrow \qquad \mathrm{A} \overset{k_1}{\rightarrow} \mathrm{C}, \tag{94}$$

indicating that in the limit $k_2 \gg k_1$ the system of two elementary reactions is replaced by a single overall "apparent" reaction $\mathrm{A} \rightarrow \mathrm{C}$ with a rate equal to $k_1 C_\mathrm{A}$.

Integration of (93) with initial conditions $C_\mathrm{A} - C_0 = C_\mathrm{C} = 0$ at $t = 0$ yields

$$C_\mathrm{A} = C_0 e^{-k_1 t}, \qquad C_\mathrm{C} = C_0 (1 - e^{-k_1 t}). \tag{95}$$

The reader can check that (92) and (95) represent the limiting form of the exact solution of the complete problem

$$\begin{aligned} C_\mathrm{A} &= C_0 e^{-k_1 t} \\ C_\mathrm{B} &= C_0 \frac{k_1}{k_2 - k_1} (e^{-k_1 t} - e^{-k_2 t}) \\ C_\mathrm{C} &= C_0 \left(1 + \frac{k_1 e^{-k_2 t} - k_2 e^{-k_1 t}}{k_2 - k_1} \right) \end{aligned} \tag{96}$$

in the limit $k_2 \gg k_1$ for $t \gg k_2^{-1}$, whereas for small times $t \sim k_2^{-1}$ the steady-state solution for C_B does not represent accurately that given in (96). These types of departures are also typically found in analyses of realistic chemical systems, for which the steady-state approximation for chain carriers is often inaccurate in the initial or final stages of a chain reaction [28], during which chain carriers are being produced or destroyed relatively rapidly through the predominance of initiation or termination steps. However, the rates of propagation steps often exceed those of initiation and termination so greatly during the major part of straight-chain reactions that the steady-state approximation is quite accurate for most of the reaction history (i.e., for $t \sim k_1^{-1}$ in the simple example analyzed above).

The analysis of realistic chemical-kinetic schemes is in general significantly more complicated than that presented in this illustrative example because there are many possible reaction paths, depending on the local conditions of composition and temperature. The expressions for the concentrations of the steady-state species become more complex than (92), and oftentimes they cannot be expressed in closed explicit form, so that truncation, that is, neglecting certain terms without formal justification, is needed to provide additional simplification prior to implementation of the reduced kinetics.

Appendix 2 – Q-criterion

The Q-criterion [176], widely defined and employed in computational fluid dynamics (CFD) for illustrating turbulent vorticity distributions in three dimensions, employs the quantity Q, defined as

$$Q = \frac{1}{2}(\|\Omega\|^2 - \|S\|^2), \tag{97}$$

where S and Ω are the strain-rate and vorticity tensor, respectively,

$$\Omega = \frac{1}{2}(\nabla \mathbf{u} + \nabla \mathbf{u}^T), \tag{98}$$

$$S = \frac{1}{2}(\nabla \mathbf{u} - \nabla \mathbf{u}^T), \tag{99}$$

The Q-criterion considers that areas where the vorticity magnitude is larger than the magnitude of the strain rate, such that $Q > 0$, correspond to the existence of a vortex. In illustrations, the surface of a fixed small positive value of Q is selected, and the value of a quantity of interest is color-coated along that surface to afford a qualitative visualization of its variation in the turbulent flow.

References

1. B. Lewis, G. Von Elbe, *Combustion, flames and explosions of gases* (Academic Press, 1987)
2. T. Poinsot, D. Veynante, *Theoretical and numerical combustion* (RT Edwards, Inc., 2005)
3. F. Williams, et al., http://web.eng.ucsd.edu/mae/groups/combustion/mechanism.html (2018)
4. R. Mével, S. Javoy, F. Lafosse, N. Chaumeix, G. Dupré, C.E. Paillard, Proceedings of The Combustion Institute **32**(1), 359 (2009)
5. G. Blanquart, P. Pepiot-Desjardins, H. Pitsch, Combustion and Flame **156**(3), 588 (2009)
6. G.P. Smith, D.M. Golden, M. Frenklach, N.W. Moriarty, B. Eiteneer, M. Goldenberg, C.T. Bowman, R.K. Hanson, S. Song, W.C. Gardiner Jr, et al., Gas Research Institute (http://www.me. berkeley. edu/gri_mech) (1999)
7. A.A. Konnov, Combustion and flame **152**(4), 507 (2008)
8. Y. Wu, S. Panigrahy, A.B. Sahu, C. Bariki, J. Beeckmann, J. Liang, A.A. Mohamed, S. Dong, C. Tang, H. Pitsch, et al., Combustion and Flame **226**, 229 (2021)
9. D.G. Goodwin, H.K. Moffat, R.L. Speth. Cantera: An object-oriented software toolkit for chemical kinetics, thermodynamics, and transport processes. `http://www.cantera.org` (2017). Version 2.3.0
10. T. Asaba, W. Gardiner Jr, R. Stubbeman, in *Symposium (International) on Combustion*, vol. 10 (Elsevier, 1965), vol. 10, pp. 295–302
11. R.S. Brokaw, in *Symposium (International) on Combustion*, vol. 10 (Elsevier, 1965), vol. 10, pp. 269–278
12. C. Treviño, Dynamics of deflagrations and reactive systems–flames **131**, 19 (1991)
13. C. Treviño, F. Mendez, Proceedings of the Combustion Institute **24**(1), 121 (1992)
14. C. Treviño, A. Liñán, in *Combustion in High-Speed Flows* (Springer, 1994), pp. 477–490
15. G. Del Alamo, F. Williams, A. Sanchez, Combustion science and technology **176**(10), 1599 (2004)

16. P. Boivin, A.L. Sánchez, F.A. Williams, Combustion and Flame **159**(2), 748 (2012)
17. P. Boivin, A. Sánchez, F. Williams, Combustion and Flame **176**, 489 (2017)
18. P. Boivin, C. Jiménez, A.L. Sánchez, F.A. Williams, Proceedings of the Combustion Institute **33**(1), 517 (2011)
19. L.S. Kassel, H. Storch, Journal of the American Chemical Society **57**(4), 672 (1935)
20. A.L. Sánchez, F.A. Williams, Progress in Energy and Combustion Science **41**, 1 (2014)
21. W.G. Vincenti, C.H. Kruger, *Introduction to physical gas dynamics*, vol. 246 (Wiley New York, 1965)
22. X. Wang, C.K. Law, The Journal of chemical physics **138**(13), 134305 (2013)
23. W. Liang, C.K. Law, Physical Chemistry Chemical Physics **20**(2), 742 (2018)
24. E.A. Tingas, D.C. Kyritsis, D.A. Goussis, Journal of Energy Engineering **145**(1), 04018074 (2019)
25. A. Azatyan, Z. Andrianova, A. Ivanova, Kinetics and catalysis **51**(3), 337 (2010)
26. A.L. Sánchez, E. Fernández-Tarrazo, F.A. Williams, Combustion and Flame **161**(1), 111 (2014)
27. P. Boivin, A.L. Sánchez, F.A. Williams, Combustion and Flame **160**(1), 76 (2013)
28. F.A. Williams, *Combustion Theory, second edition.* (Cummings Publ. Co, 1985)
29. D.R. Dowdy, D.B. Smith, S.C. Taylor, A. Williams, in *Symposium (International) on Combustion*, vol. 23 (Elsevier, 1991), vol. 23, pp. 325–332
30. F. Egolfopoulos, C.K. Law, in *Symposium (international) on combustion*, vol. 23 (Elsevier, 1991), vol. 23, pp. 333–340
31. C.M. Vagelopoulos, F.N. Egolfopoulos, C.K. Law, in *Symposium (international) on combustion*, vol. 25 (Elsevier, 1994), vol. 25, pp. 1341–1347
32. V.P. Karpov, A.N. Lipatnikov, P. Wolanski, Combustion and Flame **109**(3), 436 (1997)
33. S.D. Tse, D. Zhu, C.K. Law, Proceedings of the combustion institute **28**(2), 1793 (2000)
34. O. Kwon, G. Faeth, Combustion and Flame **124**(4), 590 (2001)
35. A. Lamorlette, F. Candelier, International Journal of Heat and Mass Transfer **82**, 117 (2015)
36. S. Verhelst, R. Woolley, M. Lawes, R. Sierens, Proceedings of the Combustion Institute **30**(1), 209 (2005)
37. M.P. Burke, Z. Chen, Y. Ju, F.L. Dryer, Combustion and Flame **156**(4), 771 (2009)
38. M. Kuznetsov, S. Kobelt, J. Grune, T. Jordan, International journal of hydrogen energy **37**(22), 17580 (2012)
39. M.C. Krejci, O. Mathieu, A.J. Vissotski, S. Ravi, T.G. Sikes, E.L. Petersen, A. Kérmonès, W. Metcalfe, H.J. Curran, Journal of Engineering for Gas Turbines and Power **135**(2) (2013)
40. A. Dahoe, Journal of loss prevention in the process industries **18**(3), 152 (2005)
41. C. Olm, I.G. Zsély, R. Pálvölgyi, T. Varga, T. Nagy, H.J. Curran, T. Turányi, Combustion and Flame (2014)
42. V.A. Alekseev, A.A. Konnov, Combustion and Flame **194**, 28 (2018)
43. D. Fernández-Galisteo, A. Weiss, A.L. Sánchez, F.A. Williams, Combustion and Flame **208**, 1 (2019)
44. K. Shkadinskii, B. Khaikin, A. Merzhanov, Combustion, Explosion and Shock Waves **7**(1), 15 (1971)
45. G. Sivashinsky, Combustion Science and Technology **15**(3-4), 137 (1977)
46. G. Goyal, U. Maas, J. Warnatz, Combustion science and technology **105**(4-6), 183 (1995)
47. E. Christiansen, C. Sung, C. Law, in *Symposium (International) on Combustion*, vol. 27 (Elsevier, 1998), vol. 27, pp. 555–562
48. E. Christiansen, C. Law, C. Sung, Combustion and flame **124**(1), 35 (2001)
49. V.V. Gubernov, A.V. Kolobov, A.A. Polezhaev, H.S. Sidhu, Combustion and flame **160**(6), 1060 (2013)
50. A. Korsakova, V. Gubernov, A. Kolobov, V. Bykov, U. Maas, Combustion and Flame **163**, 478 (2016)
51. B. Denet, P. Haldenwang, Combustion science and technology **104**(1-3), 143 (1995)
52. E. Al Sarraf, C. Almarcha, J. Quinard, B. Radisson, B. Denet, P. Garcia-Ybarra, Proceedings of the Combustion Institute **37**(2), 1783 (2019)

53. M. Tayyab, B. Radisson, C. Almarcha, B. Denet, P. Boivin, Combustion and Flame **221**, 103 (2020)
54. B. Denet, P. Haldenwang, Combustion science and technology **86**(1-6), 199 (1992)
55. M. Matalon, Proceedings of the Combustion Institute **32**(1), 57 (2009)
56. C. Altantzis, C.E. Frouzakis, A.G. Tomboulides, S.G. Kerkemeier, K. Boulouchos, Proceedings of the combustion institute **33**(1), 1261 (2011)
57. C. Altantzis, C.E. Frouzakis, A.G. Tomboulides, M. Matalon, K. Boulouchos, Journal of Fluid Mechanics **700**, 329 (2012)
58. L. Berger, K. Kleinheinz, A. Attili, H. Pitsch, Proceedings of the Combustion Institute **37**(2), 1879 (2019)
59. F. Veiga-López, M. Kuznetsov, D. Martínez-Ruiz, E. Fernández-Tarrazo, J. Grune, M. S´anchez Sanz, Physical Review Letters **124**(17), 174501 (2020)
60. Y.B. Zeldovich, (1950)
61. P.D. Ronney, Combustion and Flame **82**(1), 1 (1990)
62. P. Ronney, K. Whaling, A. Abbud-Madrid, J. Gatto, V. Pisowicz, AIAA journal **32**(3), 569 (1994)
63. P.D. Ronney, M.S. Wu, H.G. Pearlman, K.J. Weiland, AIAA journal **36**(8), 1361 (1998)
64. P.D. Ronney, in *Symposium (International) on Combustion*, vol. 27 (Elsevier, 1998), vol. 27, pp. 2485–2506
65. E. Fernández-Tarrazo, A.L. Sánchez, A. Liñán, F.A. Williams, International Journal of Hydrogen Energy **37**(2), 1813 (2012)
66. H.F. Coward, G.W. Jones, *Limits of flammability of gases and vapors*. 503-508 (US Government Printing Office, 1952)
67. N. Cohen, (1992)
68. W. Rakotoarison, A. Pekalski, M.I. Radulescu, Journal of Loss Prevention in the Process Industries **64**, 103963 (2020)
69. Y. Ballossier, F. Virot, J. Melguizo-Gavilanes, Journal of Loss Prevention in the Process Industries **72**, 104535 (2021)
70. Y. Ballossier, Topologies de l'accélération de flammes d'h2-o2-n2 dans des canaux étroits: de l'allumage jusqu'à la détonation. Ph.D. thesis, Chasseneuil-du-Poitou, Ecole nationale supérieure de mécanique et d . . . (2021)
71. A. Oppenheim, R. Soloukhin, Annual Review of Fluid Mechanics **5**(1), 31 (1973)
72. L. Kagan, G. Sivashinsky, Combustion and Flame **134**(4), 389 (2003)
73. E.S. Oran, V.N. Gamezo, Combustion and Flame **148**(1-2), 4 (2007)
74. A.Y. Poludnenko, J. Chambers, K. Ahmed, V.N. Gamezo, B.D. Taylor, Science **366**(6465), eaau7365 (2019)
75. G. Cheng, P. Bauer, R. Zitoun, The European Physical Journal-Applied Physics **65**(3) (2014)
76. J.M. Austin, The role of instability in gaseous detonation. Ph.D. thesis, California Institute of Technology, Pasadena, CA (2003)
77. F. Pintgen, C.A. Eckett, J.M. Austin, J.E. Shepherd, Combust. Flame **133**, 211 (2003)
78. M. Kaneshige, J. Shepherd, Detonation database. GALCIT Report FM97-8, California Institute of Technology: Aeronautics and Mechanical Engineering (1997)
79. W. Rudy, M. Kuznetsov, R. Porowski, A. Teodorczyk, J. Grune, K. Sempert, Proc. Combust. Inst. **34**, 1965 (2013)
80. A. Borisov, S. Khomic, V. Mikhalkin, Prog. Astronaut. Aeronaut **133**, 118 (1991)
81. S. Taileb, J. Melguizo-Gavilanes, A. Chinnayya, Combustion and Flame **218**, 247 (2020)
82. M.I. Radulescu, Combustion and Flame **195**, 151 (2018)
83. E.S. Oran, Proceedings of the Combustion Institute **35**(1), 1 (2015)
84. K. Kailasanath, AIAA journal **38**(9), 1698 (2000)
85. K. Kailasanath, in *Innovations in Sustainable Energy and Cleaner Environment* (Springer, 2020), pp. 3–21
86. Y.B. Zel'dovich, B. Gel'Fand, Y.M. Kazhdan, S. Frolov, Combust. Explo. Shock+ **23**, 342 (1987)
87. R. Klein, J. Krok, J. Shepherd, Curved quasi-steady detonations. asymptotic analysis and detailed chemical kinetics. Tech. Rep. FM95-04, GALCIT (1995)

88. B. F, Symposium (International) on Combustion pp. 745–751 (1959)
89. F. Belles, J.G. EHLERS, ARS Journal **32**(2), 215 (1962)
90. F. Belles, in *Symposium (International) on Combustion*, vol. 7 (Elsevier, 1958), vol. 7, pp. 745–751
91. S. Browne, J. Ziegler, J. Shepherd, GALCIT report FM2006 **6**, 90 (2008)
92. D. Pawel, H. Vasatko, H. WAGNER, Astronautica Acta **14**, 509 (1967)
93. J.H. Lee, *The detonation phenomenon*, vol. 2 (Cambridge University Press Cambridge, 2008)
94. E.K. Dabora, J. Nicholls, R. Morrison, in *Symposium (International) on Combustion*, vol. 10 (Elsevier, 1965), vol. 10, pp. 817–830
95. M. Reynaud, S. Taileb, A. Chinnayya, Shock Waves **30**(6), 645 (2020)
96. G. Kistiakowsky, W.G. Zinman, The Journal of Chemical Physics **23**(10), 1889 (1955)
97. G. Kistiakowsky, H.T. Knight, M.E. Malin, The Journal of Chemical Physics **20**(5), 876 (1952)
98. G. Agafonov, S. Frolov, Combustion, Explosion and Shock Waves **30**(1), 91 (1994)
99. J.A. Fay, The Physics of Fluids **2**(3), 283 (1959)
100. Y. Gao, B. Zhang, H.D. Ng, J.H. Lee, international journal of hydrogen energy **41**(14), 6076 (2016)
101. W.W. Wood, J.G. Kirkwood, The Journal of Chemical Physics **22**(11), 1920 (1954)
102. M. Reynaud, F. Virot, A. Chinnayya, Physics of Fluids **29**(5), 056101 (2017)
103. S. Taileb, Vers des simulations numériques prédictives des détonations gazeuses: influence de la cinétique chimique, de l'equation d'etat et des effets tridimensionnels. Ph.D. thesis, Chasseneuil-du-Poitou, Ecole nationale supérieure de mécanique et d . . . (2020)
104. M.A. Nettleton, *Gaseous detonations: their nature, effects and control* (Springer Science & Business Media, 1987)
105. S.S. Grossel, *Deflagration and detonation flame arresters* (John Wiley & Sons, 2010)
106. A.L. Sánchez, E. Fernández-Tarrazo, P. Boivin, A. Liñán, F.A. Williams, Comptes Rendus Mecanique **340**(11-12), 882 (2012)
107. A.L. Sánchez, M. Vera, A. Liñán, Physics of Fluids **18**(7), 078102 (2006)
108. A.L. Sánchez, A. Liñán, F.A. Williams, in *Symposium (International) on Combustion*, vol. 25 (Elsevier, 1994), vol. 25, pp. 1529–1537
109. J.D. Colwell, A. Reza, Fire Technology **41**(2), 105 (2005)
110. J.M. Kuchta, A. Bartkowiak, M.G. Zabetakis, J. Chem. Eng. Data **10**, 282 (1965)
111. C.R. Council, *Handbook of aviation fuel properties*. 530 (The Council, 1983)
112. S.K. Menon, P.A. Boettcher, B. Ventura, G. Blanquart, Combustion and Flame **163**, 42 (2016)
113. R. Mével, J. Melguizo-Gavilanes, L. Boeck, J. Shepherd, International Journal of Heat and Fluid Flow **76**, 154 (2019)
114. M. Beyer, D. Markus, Sci. Technol. Energ. Ma. **73**(1) (2012)
115. D. Roth, P. Sharma, T. Haeber, R. Schiessl, H. Bockhorn, U. Maas, Combust. Sci. Technol. **186**(10-11), 1606 (2014)
116. P.A. Boettcher, R. Mével, V. Thomas, J.E. Shepherd, Fuel **96**, 392 (2012)
117. J. Melguizo-Gavilanes, P. Boettcher, R. Mével, J. Shepherd, Combustion and Flame **204**, 116 (2019)
118. J. Melguizo-Gavilanes, L. Boeck, R. Mével, J. Shepherd, international journal of hydrogen energy **42**(11), 7393 (2017)
119. R.S. Silver, Philos. Mag. **23**(156), 633 (1937)
120. J. Melguizo-Gavilanes, R. Mével, S. Coronel, J. Shepherd, Proceedings of the Combustion Institute **36**(1), 1155 (2017)
121. S. Jones, J. Melguizo-Gavilanes, J. Shepherd, Proceedings of the Combustion Institute **37**(2), 1597 (2019)
122. N.N. Semenov, Progress of Physical Science **24**(NACA-TM-1026) (1942)
123. D.A. Frank-Kamenetskii, in *Diffusion and Heat Exchange in Chemical Kinetics* (Princeton University Press, 2015)
124. N.M. Laurendeau, Combustion and Flame **46**, 29 (1982)
125. Y.A. Cengel, A. Ghajar, McGraw-670 Hill Education **671**, 52 (2011)

126. P.A. Boettcher, Thermal ignition. Ph.D. thesis, California Institute of Technology (2012)
127. H.W. Liepmann, A. Roshko, *Elements of gasdynamics* (Courier Corporation, 2001)
128. E.F. Toro, *Riemann solvers and numerical methods for fluid dynamics: a practical introduction* (Springer Science & Business Media, 2009)
129. W. Tsang, A. Lifshitz, Annual review of physical chemistry **41**(1), 559 (1990)
130. V. Voevodsky, R. Soloukhin, in *Proc. Combust. Inst*, vol. 10 (1965), vol. 10, pp. 279–283
131. J. Meyer, A. Oppenheim, in *Symposium (International) on Combustion*, vol. 13 (Elsevier, 1971), vol. 13, pp. 1153–1164
132. K.P. Grogan, M. Ihme, Proceedings of the Combustion Institute **35**(2), 2181 (2015)
133. D. Nativel, S.P. Cooper, T. Lipkowicz, M. Fikri, E.L. Petersen, C. Schulz, Combustion and Flame **217**, 200 (2020)
134. J. Melguizo-Gavilanes, L. Bauwens, Shock Waves **23**(3), 221 (2013)
135. C.A. Eckett, *Numerical and analytical studies of the dynamics of gaseous detonations* (California Institute of Technology, 2001)
136. A. Linan, Acta Astronautica **1**(7), 1007 (1974)
137. K. Seshadri, F. Williams, International Journal of Heat and Mass Transfer **21**(2), 251 (1978)
138. P. Boivin, Reduced-kinetic mechanisms for hydrogen and syngas combustion including autoignition. Phd, Universidad Carlos III de Madrid (2011)
139. U. Niemann, K. Seshadri, F. Williams, Proceedings of the Combustion Institute **34**(1), 881 (2013)
140. H. Park, (2015)
141. W.M. Marshall, R.J. Osborne, S.E. Greene, in *53rd AIAA/SAE/ASEE Joint Propulsion Conference* (2017), p. 4665
142. G. Frenken, E. Vermeulen, F. Bouquet, B. Sanders, in *38th AIAA/ASME/SAE/ASEE Joint Propulsion Conference & Exhibit* (2002), p. 4330
143. M. Boileau, G. Staffelbach, B. Cuenot, T. Poinsot, C. Bérat, Combustion and Flame **154**(1-2), 2 (2008)
144. J. Carpio, I. Iglesias, M. Vera, A.L. Sánchez, A. Liñán, International Journal of Hydrogen Energy **38**(7), 3105 (2013)
145. D. Zhao, Y. Xia, H. Ge, Q. Lin, G. Wang, Fuel **263**, 116402 (2020)
146. A. Eyssartier, B. Cuenot, L.Y. Gicquel, T. Poinsot, Combustion and Flame **160**(7), 1191 (2013)
147. L. Esclapez, E. Riber, B. Cuenot, Proceedings of the Combustion Institute **35**(3), 3133 (2015)
148. J. Marrero-Santiago, F. Collin-Bastiani, E. Riber, G. Cabot, B. Cuenot, B. Renou, Combustion and Flame **222**, 70 (2020)
149. L. Esclapez, F. Collin-Bastiani, E. Riber, B. Cuenot, Combustion and Flame **225**, 180 (2021)
150. O.J. Haidn, Advances on propulsion technology for high-speed aircraft **1**, 6 (2008)
151. K. Breisacher, K. Ajmani, in *Third Spacecraft Propulsion Subcommittee Meeting* (2009), NASA/TM-2009-215522
152. O. Colin, K. Truffin, Proceedings of the Combustion Institute **33**(2), 3097 (2011)
153. H. Ge, P. Zhao, in *Internal Combustion Engine Division Fall Technical Conference*, vol. 51999 (American Society of Mechanical Engineers, 2018), vol. 51999, p. V002T06A007
154. M. Weinrotter, H. Kopecek, E. Wintner, M. Lackner, F. Winter, International journal of hydrogen energy **30**(3), 319 (2005)
155. H. Kopecek, S. Charareh, M. Lackner, C. Forsich, F. Winter, J. Klausner, G.n. Herdin, M. Weinrotter, E. Wintner, J. Eng. Gas Turbines Power **127**(1), 213 (2005)
156. B. Mewes, N. Rackemann, G. Kroupa, in *SPC2016-3124995, Space Propulsion Conference* (2016)
157. V.D. AGOSTA, T.F. SEAMANS, M. VANPEE, Aiaa Journal **5**(9), 1616 (1967)
158. E. Dambach, K. Cho, T. Pourpoint, S. Heister, in *46th AIAA/ASME/SAE/ASEE Joint Propulsion Conference & Exhibit* (2010), p. 6984
159. V.K. Bhosale, J. Jeong, J. Choi, D.G. Churchill, Y. Lee, S. Kwon, Combustion and Flame **214**, 426 (2020)
160. V. Bogdanov, Procedia engineering **129**, 702 (2015)

161. R. Marchan, A. Oleshchenko, S. Vekilov, M. Arsenuk, O. Bobrov, in *8^{th} European Conference for Aeronautics and Space Sciences (EUCASS)* (2019)
162. J. Hartmann, B. Trolle, Journal of Scientific Instruments **4**(4), 101 (1927)
163. E. Brocher, AIAA Journal **13**(10), 1265 (1975)
164. E. Brocher, J.P. Ardissone, International Journal of Heat and Fluid Flow **4**(2), 97 (1983)
165. K. Mørch, Journal of Fluid Mechanics **20**(1), 141 (1964)
166. S. Murugappan, E. Gutmark, Experiments in fluids **38**(6), 813 (2005)
167. C. Bauer, P. Lungu, O.J. Haidn, in *8th European Conference for Aeronautics and Space Sciences* (2019)
168. A. Conte, A. Ferrero, D. Pastrone, Advances in aircraft and spacecraft science **7**(5), 425 (2020)
169. R. Cabra, T. Myhrvold, J. Chen, R. Dibble, A. Karpetis, R. Barlow, Proceedings of the Combustion Institute **29**(2), 1881 (2002)
170. T. Cheng, J. Wehrmeyer, R. Pitz, Combustion and Flame **91**(3), 323 (1992)
171. P. Sagaut, Labs documentation scientifique. Tech. rep. (2016)
172. Y. Feng, M. Tayyab, P. Boivin, Combustion and Flame **196**, 249 (2018)
173. M. Tayyab, S. Zhao, Y. Feng, P. Boivin, Combustion and Flame **211**, 173 (2020)
174. M. Tayyab, S. Zhao, P. Boivin, Physics of Fluids **33**(3), 031701 (2021)
175. S. Taileb, A. Millan-Merino, S. Zhao, P. Boivin, Combustion and Flame **under review** (2022)
176. H. JCR, A. Wray, P. Moin, Studying Turbulence Using Numerical Simulation Databases-I1 p. 193 (1988)
177. T. Echekki, J. Chen, Combustion and Flame **134**(3), 169 (2003)
178. E. Mastorakos, Progress in Energy and Combustion Science **35**(1), 57 (2009)
179. O. Schulz, T. Jaravel, T. Poinsot, B. Cuenot, N. Noiray, Proceedings of the Combustion Institute **36**(2), 1637 (2017)
180. T. Lu, C. Yoo, J. Chen, C. Law, Journal of Fluid Mechanics **652**(1), 45 (2010)
181. P. Boivin, A. Dauptain, C. Jiménez, B. Cuenot, Combustion and Flame **159**(4), 1779 (2012)
182. S. Lam, D. Goussis, International Journal of Chemical Kinetics **26**(4), 461 (1994)
183. D.A. Goussis, H.G. Im, H.N. Najm, S. Paolucci, M. Valorani, Combustion and Flame **227**, 396 (2021)
184. C. Fotache, T. Kreutz, C.K. Law, Combustion and Flame **108**(4), 442 (1997)
185. L. Veggi, P. Boivin, Combustion and Flame **162**(3), 580 (2015)
186. A. Abdelsamie, G. Lartigue, C.E. Frouzakis, D. Thévenin, Computers & Fluids **223**, 104935 (2021)
187. P. Boivin, M. Tayyab, S. Zhao, Physics of Fluids **33**, 017703 (2021)
188. S. Blanchard, Q. Cazères, B. Cuenot, Acta Astronautica **190**, 98 (2022)
189. P.R. Medwell, B.B. Dally, Energy & fuels **26**(9), 5519 (2012)
190. Y. Hu, R. Kurose, International Journal of Hydrogen Energy **44**(12), 6313 (2019)